

Donor-acceptor effects on the optical limiting properties of BODIPY dyes



RHODES UNIVERSITY
Where leaders learn

**A thesis submitted in fulfilment of the requirements for the
degree of**

MASTER OF SCIENCE

of

RHODES UNIVERSITY

by

Zweli Thabiso Hlatshwayo

ABSTRACT

The main objectives of the research described in this thesis were firstly to synthesize and characterize a series of structurally related BODIPY dyes that are potentially suitable for use in applications, secondly to conjugate a carboxylic acid substituted BODIPY dye to amine-functionalized upconversion nanoparticles (UCNPs) through an amide bond to enable singlet oxygen production upon irradiation at 978 nm in the biological window for tissue penetration for biomedical applications, and thirdly to compare the nonlinear optical (NLO) properties of various BODIPY dyes to determine whether push-pull effects enhance their utility for optical limiting (OL) applications.

Halogenated BODIPY cores with high singlet oxygen quantum yields were prepared, which absorb in the green portion of the visible region and making it difficult to treat deeper skin tumors in the context of photodynamic therapy (PDT) applications. UCNPs generally absorb in the near-infrared (NIR) region (978 nm), and this is advantageous because, this is where absorption by water, cells and tissues is minimized. NaYF₄: Yb/Er/Gd UCNPs were synthesized, amine functionalized and successfully conjugated to a halogenated carboxylic acid functionalized BODIPY. This allowed for favorable Förster resonance energy transfer (FRET) since one of the emission wavelengths of the NaYF₄: Yb/Er/Gd UCNPs overlaps with the main absorption band of the BODIPY at 540 nm. The conjugate was irradiated at 978 nm, but instability of the BODIPY dye was observed, which made singlet oxygen quantum yield determination impossible. An enhanced singlet oxygen quantum yield value was observed upon irradiation of the conjugate at 540 nm, suggesting that further studies of this system are warranted.

The OL properties of BODIPY cores and dyes, which are π -extended at the 3,5-positions with styryl groups, were studied in a series of different organic solvents at 532 nm by using the z-

scan technique on a nanosecond timescale. Many of the dyes were used to compare the effects of introducing electron donor and acceptor groups on the OL properties of the dyes. The dipole moments of these dyes were found to correlate with the OL response. The OL results indicate that BODIPY dyes with push-pull properties, which are π -extended at the 3,5-positions with styryl groups, can be considered as viable candidates for use in OL applications. The studies sought to establish the effect of ESA in the triplet manifold as compared to the singlet manifold in as far as the OL response is concerned. The most promising dyes were embedded in polystyrene thin films, and this was found to significantly enhance their OL properties.

ACKNOWLEDGMENTS

First of all, I would like to thank my supervisor, Dr. Mack, for being awesome. He has been more than just a supervisor in the lab; he has assisted me in a number of things. Dr Mack has inspired me to be an independent researcher. I cannot find the words to describe what this has done to my life and my research career. His work ethic inspires me every single day. Even at times when I was having family problems, he was able to listen and that is priceless. I would like also thank Prof Nyokong as my co-supervisor. She has made sure everything we need is available in the laboratory when we needed it. In as much as she is very strict, this has a huge positive impact in developing us as young researchers and future leaders. Thank you very much, Prof. I thank Prof. Zhen Shen of Nanjing University for hosting me in her laboratory as part of a National Research Foundation (NRF) funded China-South Africa collaboration, and Dr Bokolombe Ngoy for all the help in the laboratory, such as the compounds that he helped to synthesize. I really appreciate the skills that he has shared with me. I will surely share these skills with my peers and with anyone in the Chemistry department. I would also like give thanks NRF for financial support.

Lokumcoka kakhulu, Ngitsandza kubonga Umdali wezulu nemhla, Jehova. Ngibonge batali bami, bangani, kanye nabantfwana bakitsi. Ikakhulu ngibonge make wami lengimutsandza kakhulu. Ngiyabonga imithandzo yakho Sobethu Mgazi, ngiphinze ngibonge ne support yakho onkhe emalanga. Ngibonge kakhulu Nongcebo, Manqoba, Simphiwe, naMlondi Hlatshwayo. Ngibonge kakhulu kubabe Hlatshwayo, ungisekele ebunzimeni nasebunanzini. Ngiyanitsanza kakhulu BoHlatshwayo. Ngiyabonga babe isupport yakho, yabonga Mhayise ngwanya.

Finally, but perhaps most importantly, I would like to thank the S22 group for all the support in the times when things were not working out. You people are the real MVPs.

TABLE OF CONTENTS

Chapter	Page
ABSTRACT.....	i
ACKNOWLEDGMENTS	iii
TABLE OF CONTENTS.....	iv
LIST OF FIGURES	vii
LIST OF SCHEMES.....	ix
LIST OF TABLES	x
LIST OF ABBREVIATIONS.....	xii
1 Introduction.....	1
1.1 Structure and modification	2
1.1.1 Halogenation	7
1.1.2 Substitution of the active methyl groups	9
1.2 PDT	10
1.2.1 Research to date on PDT.....	11
1.2.2 BODIPY dyes in PDT.....	12
1.3 Nanoparticles.....	13
1.3.1 UCNPs	13
1.3.2 Upconversion in the lanthanides	14
1.3.3 Activators, sensitizers and host matrix	15
1.3.4 Mechanisms of upconversion	16
1.3.5 Synthesis and surface modification	19
1.3.6 Applications	20
1.4 BODIPY dyes for NLO applications	21
1.4.1 Mechanisms in OL.....	24
1.4.2 The Z-scan as analysis technique.....	27
1.4.3 BODIPY dyes used in this work for NLO studies.....	35
1.5 Summary of aims	37
2 Experimental.....	39
2.1 Materials.....	39
2.2 Instrumentation.....	39
2.3 Photophysical and photochemical methods	43
2.3.1 Fluorescence quantum yield (Φ_F)	43
2.3.2 Fluorescence lifetime (τ_F).....	44
2.3.3 Singlet oxygen quantum yield (Φ_Δ).....	45
2.4 Synthesis and characterization of BODIPYs	46
2.4.1 4,4'-Difluoro-8-(4-methyl ester phenyl)-1,3,5,7-tetramethyl-4-bora-3a,4a-diaza- <i>s</i> -indacene (1).....	46
2.4.2 4,4'-Difluoro-8-(4-methyl ester phenyl)-1,3,5,7-tetramethyl-2,6-diiodo-4-bora-3a,4a-diaza- <i>s</i> -indacene (2)	47
2.4.3 4,4'-Difluoro-8-(4-methyl ester phenyl)-1,3,5,7-tetramethyl-2,6-dibromo-4-bora-3a,4a-diaza- <i>s</i> -indacene (3).....	48
2.4.4 4,4'-Difluoro-8-(4-dimethylamino phenyl)-1,3,5,7-tetramethyl-4-bora-3a,4a-diaza- <i>s</i> -indacene (4).....	49
2.4.5 4,4'-Difluoro-8-(4-carboxyphenyl)-1,3,5,7-tetramethyl-2,6-diiodo-4-bora-3a,4a-diaza- <i>s</i> -indacene (5)	50

2.4.6	4,4'-Difluoro-8-(4-phenoxyphthalonitrile)-1,3,5,7-tetramethyl-2,6,4-bora-3a,4a-diaza- <i>s</i> -indacene (6)	51
2.4.7	4,4'-Difluoro-8-(4-hydroxyphenyl)-1,3,5,7-tetramethyl-4-bora-3a,4a-diaza- <i>s</i> -indacene (7).....	53
2.4.8	4,4'-Difluoro-8-(4-hydroxyphenyl)-1,3,5,7-tetramethyl-2,6-dibromo-4-bora-3a,4a-diaza- <i>s</i> -indacene (8)	54
2.4.9	4'-difluoro-8-(4-methyl ester phenyl)-1,3,5,7-tetramethyl-2,6-diethyl-4-bora-3a,4a-diaza- <i>s</i> -indacene (9)	55
2.4.10	4,4'-Difluoro-8-(4-methyl ester phenyl)-1,7-dimethyl-2,6-diethyl-3,5,-di-styryl-(4' benzyloxy)-4-bora-3a,4a-diaza- <i>s</i> -indacene (10).....	56
2.4.11	4,4'-Difluoro-8-(4-methyl ester phenyl)-1,7-dimethyl-3,5,-di-styryl-(4'-benzyloxy)-4-bora-3a,4a-diaza- <i>s</i> -indacene (11)	57
2.4.12	4,4'-Difluoro-8-(4-methyl ester phenyl)-1,7-dimethyl-2,6-dibromo-3,5,-di-styryl-(4'-benzyloxy)-4-bora-3a,4a-diaza- <i>s</i> -indacene (12)	58
2.4.13	4,4'-Difluoro-8-(4-hydroxyphenyl)-1,7-dimethyl-3,5,-di-styryl-(4'-benzyloxy)-4-bora-3a,4a-diaza- <i>s</i> -indacene (13)	59
2.4.14	4,4'-Difluoro-8-(4-hydroxyphenyl)-1,7-dimethyl-2,6-dibromo-3,5,-di-styryl-(4' benzyloxy)-4-bora-3a,4a-diaza- <i>s</i> -indacene (14)	60
2.4.15	4,4'-Difluoro-8-(4-methyl ester phenyl)-1,7-dimethyl-3,5,-di-styryl-(4'-dimethylamino)-4-bora-3a,4a-diaza- <i>s</i> -indacene (15)	61
2.4.16	4,4'-Difluoro-8-(4-methyl ester phenyl)-1,7-dimethyl-3,5,-di-styryl-(4'-dimethylamino)-4-bora-3a,4a-diaza- <i>s</i> -indacene (16)	62
2.4.17	4,4'-Difluoro-8-(4-methyl ester phenyl)-1,7-dimethyl-2,6-diethyl-3,5, -di-styryl-(4'-dimethylamino)-4-bora-3a,4a-diaza- <i>s</i> -indacene (17)	63
2.4.18	4,4'-Difluoro-8-(4-carboxyphenyl)-1,7-dimethyl-2,6-diethyl-3,5,-di-styryl-(4'-dimethylamino)-4-bora-3a,4a-diaza- <i>s</i> -indacene (18)	63
2.5	Synthesis and characterization of UCNPs.....	65
2.5.1	Uncapped NaYF ₄ :Yb/Er/Gd	65
2.5.2	Silica capped NaYF ₄ :Yb/Er/Gd@Si	66
2.5.3	Amino capped NaYF ₄ :Yb/Er/Gd@Si@NH ₂	66
2.5.4	Conjugation of amine-functionalized UCNPs and iodinated carboxylic acid BODIPY.....	66
2.6	Preparation of thin films.....	67
3	Synthesis and characterization of BODIPY dyes	69
3.1	Synthesis, spectroscopic properties and characterization of the BODIPY dyes	70
3.1.1	4,4'-Difluoro-8-(4-methyl ester phenyl)-1,3,5,7-tetramethyl-4-bora-3a,4a-diaza- <i>s</i> -indacene (1).....	70
3.1.2	4,4'-Difluoro-8-(4-methyl ester phenyl)-1,3,5,7-tetramethyl-2,6-diiodo-4-bora-3a,4a-diaza- <i>s</i> -indacene (2)	72
3.1.3	4,4'-Difluoro-8-(4-methyl ester phenyl)-1,3,5,7-tetramethyl-2,6-dibromo-4-bora-3a,4a-diaza- <i>s</i> -indacene (3).....	74
3.1.4	4,4'-Difluoro-8-(4-dimethylamino phenyl)-1,3,5,7-tetramethyl-4-bora-3a,4a-diaza- <i>s</i> -indacene (4)	75
3.1.5	4,4'-Difluoro-8-(4-carboxyphenyl)-1,3,5,7-tetramethyl-2,6-diiodo-4-bora-3a,4a-diaza- <i>s</i> -indacene (5)	76
3.1.6	4,4'-Difluoro-8-(4-phenoxyphthalonitrile)-1,3,5,7-tetramethyl-2,6,4-bora-3a,4a-diaza- <i>s</i> -indacene (6)	77
3.1.7	4,4'-Difluoro-8-(4-hydroxyphenyl)-1,3,5,7-tetramethyl-4-bora-3a,4a-diaza- <i>s</i> -indacene (7).....	78

3.1.8	4,4'-Difluoro-8-(4-methyl ester phenyl)-1,7-dimethyl-2,6-diethyl-3,5,-di-styryl-(4' benzyloxy)-4-bora-3a,4a-diaza- <i>s</i> -indacene (10)	79
3.1.9	4,4'-Difluoro-8-(4-methyl ester phenyl)-1,7-dimethyl-3,5,-di-styryl-(4'-benzyloxy)-4-bora-3a,4a-diaza- <i>s</i> -indacene (11)	81
3.1.10	4,4'-Difluoro-8-(4-methyl ester phenyl)-1,7-dimethyl-2,6dibromo-3,5,-di-styryl-(4'-benzyloxy)-4-bora-3a,4a-diaza- <i>s</i> -indacene (12)	83
3.1.11	4,4'-Difluoro-8-(4-hydroxyphenyl)-1,7-dimethyl-3,5,-di-styryl-(4'-benzyloxy)-4-bora-3a,4a-diaza- <i>s</i> -indacene (13)	85
3.1.12	4,4'-Difluoro-8-(4-hydroxyphenyl)-1,7-dimethyl-2,6-dibromo-3,5,-di-styryl-(4' benzyloxy)-4-bora-3a,4a-diaza- <i>s</i> -indacene (14)	86
3.1.13	4,4'-Difluoro-8-(4-methyl ester phenyl)-1,7-dimethyl-3,5,-di-styryl-(4'-dimethylamino)-4-bora-3a,4a-diaza- <i>s</i> -indacene (16)	87
3.1.14	4,4'-Difluoro-8-(4-carboxyphenyl)-1,7-dimethyl-2,6-diethyl-3,5,-di-styryl-(4'-dimethylamino)-4-bora-3a,4a-diaza- <i>s</i> -indacene (18)	89
3.2	Concluding remarks	90
4	NLO parameters of BODIPY dyes in solution and in polymer thin films.....	93
4.1	BODIPYs for NLO studies	93
4.2	NLO parameters	93
4.2.1	Heavy atom effects	97
4.2.2	Donor-acceptor effects.....	98
4.2.3	Solvent effects.....	100
4.2.4	Energy variations	101
4.2.5	Concentration variations	102
4.2.6	OL threshold (I_{lim})	103
4.3	BODIPY– polystyrene thin films.....	106
4.4	Concluding remarks	108
5	UCNPs	111
5.1	Characterization of UCNPs.....	112
5.1.1	Transmission electron microscopy (TEM)	112
5.1.2	Atomic force microscopy (AFM)	113
5.1.3	Energy-dispersive X-ray spectroscopy (EDS).....	115
5.1.4	Powder x-ray diffraction (XRD).....	116
5.1.5	Infrared spectroscopy (IR)	117
5.1.6	Steady-state and time-resolved fluorescence spectroscopy (TCSPC).....	118
5.1.7	Photophysical properties.....	120
5.2	Concluding remarks	121
6	Molecular modelling.....	123
6.1	Geometry optimizations and TD-DFT calculations	123
6.2	BODIPYs for NLO applications	124
6.3	Molecular modelling for BODIPY dyes: (1), (3), (10), (11), (12), and (18)	125
6.4	Concluding remarks	132
7	Conclusion	134
7.1	Limitations and future work.....	136
8	References.....	138

LIST OF FIGURES

Figure 1.01	Generic structures of common fluorophores including BODIPY.....	2
Figure 1.02	Naming and numbering conventions for BODIPY based on <i>s</i> -indacene.....	3
Figure 1.03	The crystal structure of unsubstituted BODIPY elucidated by X-ray analysis with atoms labelled and 50% probability displacement ellipsoids.	5
Figure 1.04	A typical BODIPY absorption spectrum (RIGHT) and the transitions involved (LEFT).....	5
Figure 1.05	The effect of substituents on the absorption wavelengths of simple BODIPYs. .	7
Figure 1.06	Nodal patterns of the HOMO and LUMO of an unsubstituted BODIPY model compound at an isosurface value of 0.07 a.u..	8
Figure 1.07	Jablonski diagram showing the mechanism of formation of singlet oxygen (¹ O ₂). When a photosensitizer decays from the T ₁ excited state to the S ₀ ground state, a quantum-forbidden spin flip is required; spin is conserved by an energy transfer to molecular oxygen present in the tissue, resulting in the production of highly reactive singlet oxygen.	11
Figure 1.08	The differences between the three upconversion processes: ESA, ETU, and PA	17
Figure 1.09	Upconversion processes..	19
Figure 1.10	Schematic illustration of silica coated multicolor UCNPs based on the FRET mechanism.....	20
Figure 1.11	The behavior and definition of an optical limiter.....	25
Figure 1.12	The behavior of an ideal optical limiter, I _{trans} = transmitted fluence, I _{lim} =incident fluence.	25
Figure 1.13	Jablonski diagrams showing potential OL process mechanisms for (A) BODIPYs with halogens at the 2,6-positions that are likely to have a populated triplet excited state and (B) non-halogenated BODIPYs that do not undergo ISC to the triplet excited.....	26
Figure 1.14	Free-carrier absorption (FCA) in a semiconductor material.	27
Figure 1.15	Schematic diagram of a basic Z-scan set-up. Beam splitter (BS), convex lens (CL), zero position (ZP), sample holder (S), aperture (A), reference (D1) and probe detector (D2). The -z to +z describes the movement of a sample along the z-axis through the focus (ZP) of the lens.	28
Figure 1.16	A typical open aperture Z-scan profile depicting a positive nonlinear.	29
Figure 2.01	Schematic diagram of the laser setup for the z-scan measurements.	43
Figure 3.01	Normalized absorption (gray), excitation (blue) and emission (orange) spectra of BODIPY (1) in benzene.....	72
Figure 3.02	Normalized absorption (gray), excitation (blue) and emission (orange) spectra of BODIPY (2) in benzene.....	73
Figure 3.03	Normalized absorption (gray), excitation (blue) and emission (orange) spectra of BODIPY (3) in benzene.....	74
Figure 3.04	Normalized absorption (gray), excitation (blue) and emission (orange) spectra of BODIPY (4) in benzene.....	76
Figure 3.05	Normalized absorption (gray), excitation (blue) and emission (orange) spectra of BODIPY (5) in benzene.....	77
Figure 3.06	Normalized absorption (gray), excitation (blue) and emission (orange) spectra of BODIPY (6) in benzene.....	78
Figure 3.07	Normalized absorption (gray), excitation (blue) and emission (orange) spectra of BODIPY (7) in benzene.....	79

Figure 3.08	^1H NMR spectrum of BODIPY (10) in CDCl_3 .	80
Figure 3.09	Normalized absorption (gray), excitation (blue) and emission (orange) spectra of BODIPY (10) in benzene.	81
Figure 3.10	Normalized absorption (gray), excitation (blue) and emission (orange) spectra of BODIPY (11) in DMF.	83
Figure 3.11	Normalized absorption (gray), excitation (blue) and emission (orange) spectra of BODIPY (12) in DMSO.	84
Figure 3.12	Normalized absorption (gray), excitation (blue) and emission (orange) spectra of BODIPY (13) in DMSO.	86
Figure 3.13	Normalized absorption (gray), excitation (blue) and emission (orange) spectra of BODIPY (14) in DMSO.	87
Figure 3.14	Normalized absorption (gray), excitation (blue) and emission (orange) spectra of BODIPY (16) in benzene.	89
Figure 3.15	Normalized absorption (gray), excitation (blue) and emission (orange) spectra of BODIPY (18) in benzene.	90
Figure 4.01	Open-aperture z-scans for all of the BODIPYs in DMSO for BODIPY (11-14) and in benzene for BODIPYs (4), (10), (16) and (18) at a fixed concentration of $21.6 \mu\text{M}$ and a laser pulse input energy of ca. $26 \mu\text{J}$. Detailed NLO parameters are provided in Table 4.01 .	97
Figure 4.02	Output fluence (I_{out}) versus input fluence (I_0) curves for the BODIPYs at a fixed concentration of $21.6 \mu\text{M}$ and a laser pulse input energy of $26 \mu\text{J}$...	106
Figure 4.03	The UV-visible absorption spectrum of BODIPY (13) in the polystyrene thin film used for z-scan measurements.	107
Figure 5.01	TEM images of Oleate@UCNPs (A_1 , A_2), Si@UCNPs (B_1 , B_2) and NH_2 @UCNPs (C_1).	113
Figure 5.02	AFM images and average size distribution of NH_2 @UCNPs (A_1 , A_2) and of BODIPY@UCNPs (B_1 , B_2), respectively.	114
Figure 5.03	EDS images of Oleate@UCNPs (A), Si@UCNPs (B), NH_2 @UCNPs (C) and BODIPY@UCNPs (D).	115
Figure 5.04	(A) The XRD pattern for $\beta\text{-NaYF}_4$ nanocrystals, (B) the XRD pattern for $\beta\text{-NaYF}_4$ nanocrystals with reference peaks highlighted.	116
Figure 5.05	The FT-IR spectra of Oleate@UCNPs, Si@UCNPs, NH_2 @UCNPs, BODIPY (5) and the UCNP-BODIPY conjugate.	117
Figure 5.06	The fluorescence of the UCNPs (A), the spectral overlap of the UCNP fluorescence and the absorption bands of BODIPY (5) (B) and the effect of FRET on the fluorescence of the UCNP-BODIPY conjugate upon irradiation at 978 nm (C).	119
Figure 5.07	Degradation of DPBF by singlet oxygen generated through photoirradiation of BODIPY (5) measured at one minute intervals.	120
Figure 5.08	Degradation of DPBF by singlet oxygen generated through photoirradiation of the UCNP-BODIPY conjugate measured at one minute intervals.	120
Figure 6.01	Nodal patterns at an isosurface value of 0.02 a.u. and frontier MO energies for BODIPYs (1), (3), (10), (11), (12), and (18) in TD-DFT calculations carried out using the CAM-B3LYP functional with SDD basis sets.	129
Figure 6.02	The frontier MO energies and HOMO–LUMO gaps for BODIPYs (1), (3), (10), (11), (12), and (18), using the CAM-B3LYP functional with the SDD basis set.	130
Figure 6.03	The TD-DFT calculations of BOIPYs (1), (3), (10), (11), (12), and (18) at the CAMB3LYP/6-31G (d) level of theory	131

LIST OF SCHEMES

Scheme 2.01 The acid catalyzed synthesis of 4,4'-difluoro-8-(4-methyl ester phenyl)-1,3,5,7-tetramethyl-4-bora-3a,4a-diaza- <i>s</i> -indacene (1) via the classic “1-pot 3-step” method, highlighting the structural changes that occur at each step.....	47
Scheme 2.02 Synthesis of 4,4'-difluoro-8-(4-methyl ester phenyl)-1,3,5,7-tetramethyl-2,6-diiodo-4-bora-3a,4a-diaza- <i>s</i> -indacene (2) via nucleophilic addition of iodine to BODIPY.....	48
Scheme 2.03 Synthesis of 4,4'-difluoro-8-(4-methyl ester phenyl)-1,3,5,7-tetramethyl-2,6-dibromo-4-bora-3a,4a-diaza- <i>s</i> -indacene (2) via nucleophilic addition of bromine to BODIPY (1).....	49
Scheme 2.04 The acid catalyzed synthesis of 4,4'-difluoro-8-(4-dimethylaminophenyl)-1,3,5,7-tetramethyl-4-bora-3a,4a-diaza- <i>s</i> -indacene (4) via the classic “1-pot 3-step” method.....	50
Scheme 2.05 Synthesis of 4,4'-difluoro-8-(4-carboxyphenyl)-1,3,5,7-tetramethyl-2,6-diiodo-4-bora-3a,4a-diaza- <i>s</i> -indacene (5) via hydrolysis of BODIPY (1).....	51
Scheme 2.06 The acid catalyzed synthesis of 4,4'-difluoro-8-(4-phenoxyphthalonitrile)-1,3,5,7-tetramethyl-2,6-4-bora-3a,4a-diaza- <i>s</i> -indacene (6) via the classic “1-pot 3-step” method, highlighting the structural changes that occur at each step.	52
Scheme 2.07 The acid catalyzed synthesis of 4,4'-difluoro-8-(4-hydroxyphenyl)-1,3,5,7-tetramethyl-4-bora-3a,4a-diaza- <i>s</i> -indacene (7) via the classic “1-pot 3-step” method, highlighting the structural changes that occur at each step.....	54
Scheme 2.08 Synthesis of 4,4'-difluoro-8-(4-hydroxy phenyl)-1,3,5,7-tetramethyl-2,6-dibromo-4-bora-3a,4a-diaza- <i>s</i> -indacene (8) via nucleophilic addition of bromine to BODIPY (7).....	54
Scheme 2.09 The acid catalyzed synthesis of 4,4'-difluoro-8-(4-dimethylamino phenyl)-1,3,5,7-tetramethyl-4-bora-3a,4a-diaza- <i>s</i> -indacene (9) via the classic “1-pot 3-step” method.....	55
Scheme 2.10 Knoevenagel condensation of 4-(benzyloxy) benzaldehyde and (9) resulting in the synthesis of di-(4-benzyloxy)styryl BODIPY (10).....	56
Scheme 2.11 Knoevenagel condensation of 4-(benzyloxy)benzaldehyde and (1) resulting in the synthesis of di-(4-benzyloxy)styryl BODIPY (11).....	57
Scheme 2.12 Knoevenagel condensation of 4-(benzyloxy)benzaldehyde and (3) resulting in the synthesis of di-(4-phenoxy)styryl BODIPY (12).....	58
Scheme 2.13 Knoevenagel condensation of 4-(benzyloxy)benzaldehyde and (7) resulting in the synthesis of di-(4-phenoxy)styryl BODIPY (13).....	59
Scheme 2.14 Knoevenagel condensation of 4-(benzyloxy)benzaldehyde and (8) resulting in the synthesis of di-(4-benzyloxy)styryl BODIPY (14).....	60
Scheme 2.15 Knoevenagel condensation of 4-(dimethylamino)benzaldehyde and (1) resulting in the synthesis of di-(4-dimethylamino)styryl BODIPY (15).....	61
Scheme 2.16 Synthesis of 4,4'-difluoro-8-(4-carboxyphenyl)-1,3,5,7-tetramethyl-2,6-diiodo-4-bora-3a,4a-diaza- <i>s</i> -indacene (16) via hydrolysis of BODIPY (15).....	62
Scheme 2.17 Knoevenagel condensation of 4-(dimethylamino)benzaldehyde and (9) resulting in the synthesis of di-(4-dimethylamino)styryl BODIPY (17).....	63
Scheme 2.18 Knoevenagel condensation of 4-(dimethylamino) benzaldehyde and (9) resulting in the synthesis of di-(4-dimethylamino)styryl BODIPY (17). Hydrolysis of BODIPY (17) to obtain BODIPY (18).....	64
Scheme 2.20 Schematic of UCNPs capping and functionalization.....	65
Scheme 3.01 The structures of all the eighteen BODIPY dyes synthesized in this thesis.	69

LIST OF TABLES

Table 1.01	BODIPY dyes whose nonlinear properties have been reported in the literature.	22
Table 3.01	Photophysical data BODIPY (1)	71
Table 3.02	Photophysical data BODIPY (2)	73
Table 3.03	Photophysical data BODIPY (3)	74
Table 3.04	Photophysical data BODIPY (4)	76
Table 3.05	Photophysical data BODIPY (5)	76
Table 3.06	Photophysical data BODIPY (6)	77
Table 3.07	Photophysical data BODIPY (7)	78
Table 3.08	Photophysical data BODIPY (10)	81
Table 3.09	Photophysical data BODIPY (11)	82
Table 3.10	Photophysical data BODIPY (12)	84
Table 3.11	Photophysical data BODIPY (13)	85
Table 3.12	Photophysical data BODIPY (14)	87
Table 3.13	Photophysical data BODIPY (16)	88
Table 3.14	Photophysical data BODIPY (18)	90
Table 4.01	The NLO parameters of the synthesized BODIPYs (11-14) in solution (DMSO) and thin films.	98
Table 4.02	The NLO parameters of the synthesized BODIPYs (4), (6), (10), (16), and (18) in benzene.	100
Table 4.03	The NLO parameters of the synthesized BODIPYs (4), (16) and (18) in different solvents.	101
Table 4.04	The NLO parameters of the synthesized BODIPY (16) at different laser pulse input energies.	102
Table 5.01	Photophysical data for BODIPY (5) and the UCNP-BODIPY conjugate.	121
Table 6.01	The NLO parameters of the synthesized BODIPYs in solution with their calculated dipole moments.	125
Table 6.02	The TD-DFT calculations at the CAM-B3LYP/6-31G(d) basis sets for the B3LYP optimized structures of (1), (3), (11), (12), (10) and (18).	132

LIST OF SYMBOLS

α	Linear absorption coefficient
\AA	Angstrom
β	Nonlinear absorption coefficient
β_{eff}	Effective nonlinear absorption coefficient
ε	Molar extinction coefficient
F	Integrated fluorescence emission
γ	Second order hyperpolarizability
I_{00}	Irradiance at $z = 0$.
I_{lim}	Optical limiting threshold
$[\chi^{(3)}]$	Third-order nonlinear susceptibility
λ	Wavelength
μ	Dipole moment
η	Refractive index
Φ_{Δ}	Singlet oxygen quantum yield
Φ_{F}	Fluorescence quantum yield
S_0	Singlet ground state
S_1	First singlet excited state
t	Time
T_1	First triplet excited state
τ_{F}	Fluorescence lifetime

LIST OF ABBREVIATIONS

A	Absorbance
Abs	Absorption
AFM	Atomic force microscope
APTES	3-aminopropyltriethoxysilane
B3LYP	Becke 3-Parameter, Lee, Yang and Parr
BODIPY	4,4'-difluoro-4-bora-3a,4a-diaza-s-indacene
CAM-B3LYP	Coulomb-attenuating method-Becke 3-Parameter, Lee, Yang and Parr
CR	Cross relaxation
DCM	Dichloromethane
DDQ	2,3-Dichloro-5,6-dicyano-1,4-benzoquinone
DFT	Density functional theory
DMF	Dimethylformamide
DMSO	Dimethyl sulfoxide
DPBF	1,3-Diphenylisobenzofuran
EDG	Electron donating group
EDS	Energy-dispersive X-ray spectroscopy
Em	Emission

ESA	Excited state absorption
ETU	Energy transfer up-conversion
EWG	Electron withdrawing group
Exc	Excitation
F	Fluorescence
FRET	Förster resonance energy transfer
FT-IR	Fourier transformation Infra-red spectroscopy
HF	Hartree–Fock
HOMO	Highest occupied molecular orbital
ISC	Intersystem-crossing
LUMO	Lowest unoccupied molecular orbital
MALDI-TOF	Matrix-assisted laser desorption/ionization-time of flight
MO	Molecular orbital
MS	Mass spectrometry
NBS	N-bromosuccinimide
Nd:YAG	Neodymium-doped yttrium aluminium garnet
NLO	Nonlinear optics
NIS	N-iodosuccinimide

NIR	Near-infrared
NMR	Nuclear magnetic resonance spectroscopy
OA	Oleic acid
OL	Optical limiting
P	Phosphorescence
PA	Photon avalanche
Pc	Phthalocyanine
PDT	Photodynamic therapy
PEG	Polyethylene glycol
RE	Rare earth
RSA	Reverse saturable absorption
r.t.	Room temperature
SA	Saturable absorption
SEM	Scanning electron microscopy
SDD	Gaussian 09 default basis set
TCSPC	Time-correlated single photon counting
TD-DFT	Time-dependent density functional theory
TEA	Triethylamine

TEM	Transmission electron microscope
TEOS	Tetraethoxysilane
THF	Tetrahydrofuran
TFA	Trifluoroacetic acid
TLC	Thin layer chromatography
2PA	Two-photon absorption
UCNPs	Upconversion nanoparticles

Chapter 1: Introduction

1 Introduction

Research on the difluoro-boraindacene family (4,4-difluoro-4-bora-3a,4a-diaza-*s*-indacene, BODIPY) only started gaining interest relatively recently and has not been carried out to the same depth as that on other classes of fluorescent dyes, which continue to attract attention from scientists for various applications [1]. However, over the past two decades, many research groups around the world have explored the synthesis and properties of BODIPY dyes. Their versatility and potential utility for a wide range of applications have enhanced their popularity. Treibs and Kreuzer reported the first member of this class of compound in 1968 [1]. Despite this, relatively little attention was given to these compounds until the end of the 1980s. Their subsequent application in biological labeling resulted in a huge increase in interest in the development of new BODIPY dyes [2, 3]. Due to their favorable properties, such as their small Stokes shift, high environmental independence, high fluorescence quantum yields, and high solubility in numerous organic solvents, BODIPY dyes have been studied for use in imaging, sensing, photodynamic therapy (PDT), optical limiting (OL), and electrochemistry [3-11].

BODIPY dyes have recently been studied for applications in OL because of their structural versatility which allows different electron donating groups (EDGs) and electron withdrawing groups (EWGs) to be attached at different positions of the parent BODIPY core [4, 5], and part of the work described in this thesis can be viewed as an extension of this. The main objectives of the research described in this thesis are, firstly to synthesize and characterize a series of structurally related BODIPY dyes that are potentially suitable for use in applications, secondly to conjugate a carboxylic acid substituted BODIPY dye to amine-functionalized upconversion nanoparticles (UCNPs) through an amide bond to enable singlet oxygen production upon irradiation at 978 nm in the biological window for tissue penetration

for biomedical applications, and thirdly to compare the nonlinear optical (NLO) properties of various BODIPY dyes to determine whether push-pull effects enhance their utility for OL applications.

1.1 Structure and modification

Modern medicine continues to advance, especially with the development of new technologies and novel techniques for bioimaging and disease therapies, and with such progression comes the need for new fluorophores capable of being excited and emitting in the red to near-infrared (IR) region of the visible spectrum [6]. The optimal “biological window” of 650–1350 nm allows for minimal interference from endogenous chromophores, such as heme, and optimal light penetration through tissues with reduced light scattering and diminished damage to the tissues being imaged [7-10]. Ideally, these fluorophores should no longer possess a single use, and the demand for dual-purpose theranostic agents is on the rise. Although numerous nonradioactive fluorophores, including rhodamines, cyanines and fluorescein (**Fig 1.01**), are on the market for facile modification and use, the difluoro-boraindacene family of dyes has garnered considerable attention due to their versatility [7-10].

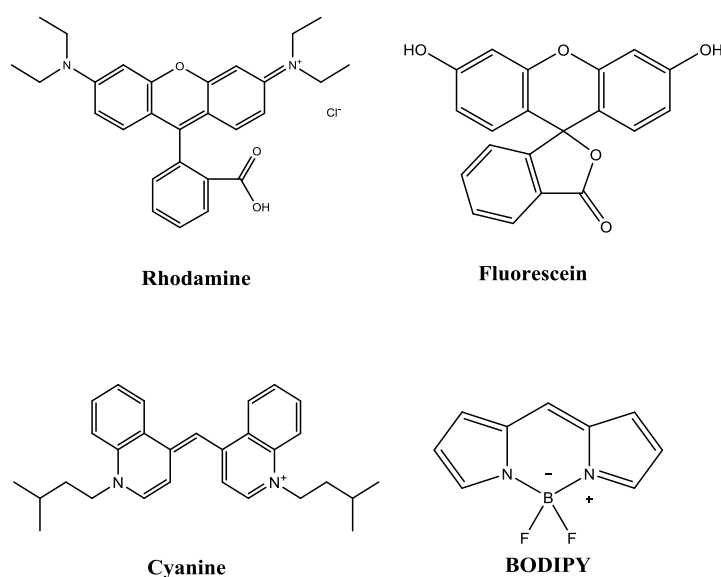
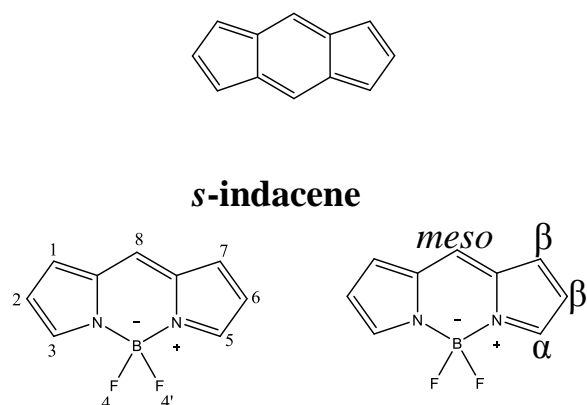


Figure 1.01 Generic structures of common fluorophores including BODIPY.

BODIPY dyes are formed from the complexation of a dipyrromethene ligand with a disubstituted boron moiety, typically in the form of BF_2 , achieved using boron trifluoride diethyl etherate [5, 11, 12]. The dipyrromethene ligand is formed from the linking of the α -position of two pyrroles via a methine bridge. Complexation of the dipyrromethene ligand with the BF_2 unit forms a rigid tricyclic system and prevents *cis/trans* isomerization of the dipyrromethene, allowing for the conjugation of π -electrons along the carbon-nitrogen backbone, which leads to unusually high fluorescence quantum yields [13]. The BODIPY fluorophore, once complexed with BF_2 can be compared to a “constrained” cross-conjugated cyanine dye possessing fixed planarity in the conjugated π -system of the fluorophore [14]. The resultant zwitterionic species possesses an overall neutral charge.

Several approaches have been accepted in the systematic naming the BODIPY core. The first utilizes the similarity in BODIPYs structure to that of *s*-indacene (**Fig 1.02**) [11, 12]. Following this identification system, the 3- and 5-positions are referred to as the α -carbons and the 1, 2, 6 and 7-positions are described as the β -carbons, in a similar manner to conventions related to the pyrroles [15]. The C-8 position is also referred to as the *meso*-position, following the labeling conventions of porphyrin ring systems [12].



4,4-difluoro-4-bora-3a,4a-diaza-*s*-indacene (BODIPY)

Figure 1.02 Naming and numbering conventions for BODIPY based on *s*-indacene.

Analysis of single crystalline BODIPY chromophores units identifies a three-ring fused framework, as shown in **Fig 1.03**, exhibiting strong π -electron delocalization across the nine carbons and two nitrogen atoms making up the central six-membered ring and the two pyrrolic rings [16]. The B-N bonds disrupt this π -conjugation since the BF_2 moiety plays very little to no role in the π -delocalization. The central boron atom displays a distorted tetrahedral geometry with a BF_2N_2 configuration as defined by the $\text{N}_1\text{-B}_1\text{-N}_2$ and $\text{F}_1\text{-B}_1\text{-F}_2$ bond angles [17]. It is noteworthy that the BODIPY fluorophore is isoelectronic with heptamine cyanine possessing twelve π -electrons delocalized over eleven atoms, rather than the monomethine cyanine dye with six π -electrons equally distributed over five atoms [18].

The monoclinic unit cell of the BODIPY fluorophore consists of four molecules stacked head-to-tail, an arrangement that aids in optimizing π - π interactions between adjacent hydrophobic BODIPY molecules and countering the variability of the fluorine atoms dipole moments [19]. The slight polarization of the heteroatoms generates electronically diverse reaction sites of the BODIPY carbon core, favouring both nucleophilic and electrophilic reactions. Such electronic diversity across a single molecular structure opens the door for a very wide range of structural modifications [20].

Known affectionately as “porphyrin’s little sister,” these fluorescent molecules have highly favorable photophysical properties [10]. As is the case with porphyrins, BODIPY and its derivatives absorb strongly in the visible region. They have relatively sharp emission peaks, possess high fluorescence quantum yields, and high molar absorption coefficients (in the range of 40,000 to 80,000 $\text{M}^{-1}\text{cm}^{-1}$), and have favorable properties for imaging agents such as the negligible triplet-state formation and small Stokes shifts (ca. 10 nm) of non-halogenated BODIPY cores [10, 16], resistance toward self-aggregation, and relatively long fluorescence lifetimes in the nanosecond range [5]. Additionally, most BODIPY dyes exhibit high thermal

and photostability both in the solid state and in solution, are highly soluble in most organic solvents, and are insensitive to solvent polarity and pH [11, 21, 22].

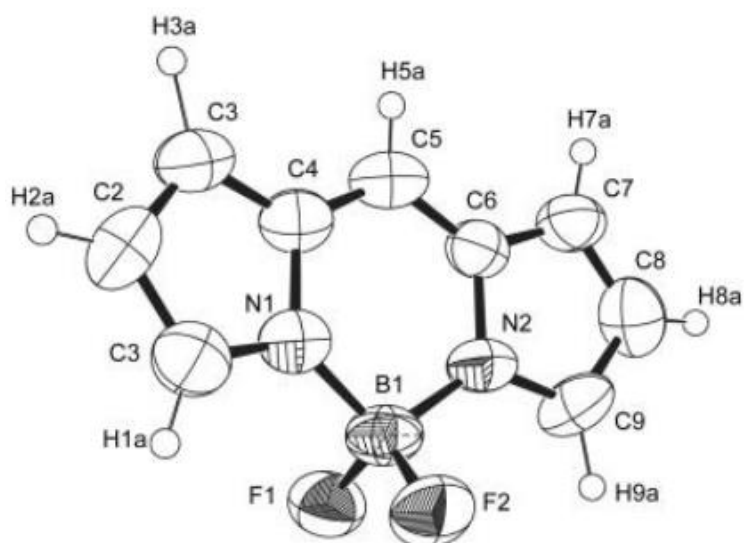


Figure 1.03 The crystal structure of unsubstituted BODIPY elucidated by X-ray analysis with atoms labelled and 50% probability displacement ellipsoids. Reprinted with permission from reference 23; *Dyes and Pigments*, 2009.

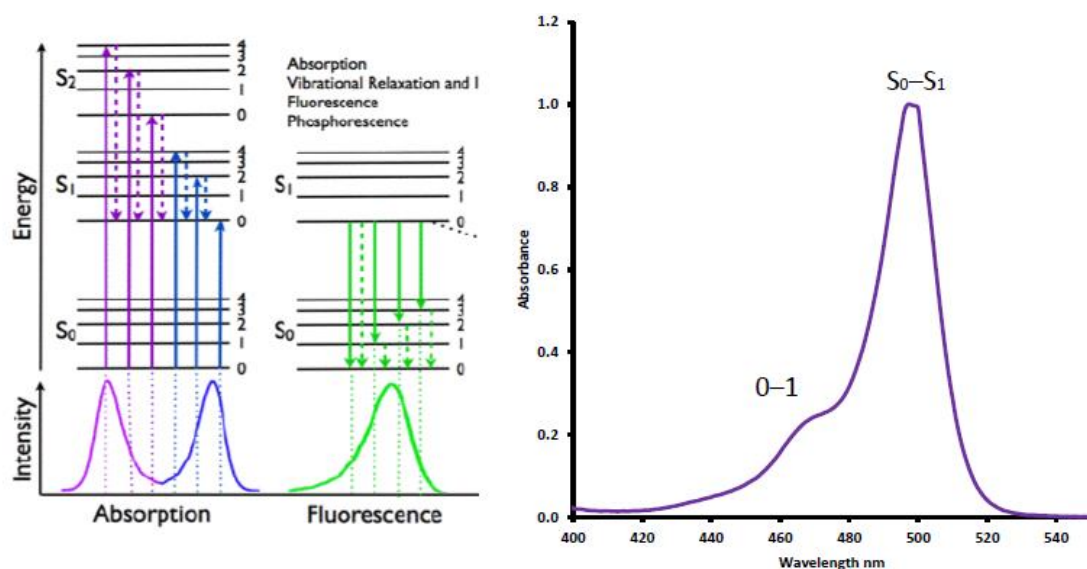


Figure 1.04 A typical BODIPY absorption spectrum (RIGHT) and the transitions involved (LEFT).

The BODIPY absorption spectrum typically contains a strong, narrow absorption band in the visible region signifying the S_0 - S_1 (π - π^*) (**Fig 1.04**) transition with a shoulder of high energy around 480 nm assigned to the 0-1 vibrational overtone (**Fig 1.04**). A broad, much weaker band around 350 nm arises from the S_0 - S_2 (π - π^*) transition [24]. Upon excitation to either the S_1 or S_2 states, an equally narrow emission band of mirror image to the absorption spectra is observed from the S_1 state (**Fig 1.04**). Most BODIPYs emit at wavelengths less than 600 nm, providing yellow to green emission bands (500–590 nm) [5, 25]. Unsubstituted BODIPY typically absorbs near 500 nm and emits at ca. 510 nm [24]. Small Stokes shifts are normally observed and this indicates that there is only a modest change in the BODIPY core structure following S_0 - S_1 transition and vibrational relaxation [24]. Addition of functionality at any position of the aromatic core alters the photochemical and photophysical properties to varying degrees, dependent upon the groups added. The BODIPY core can be easily modified to bear desired functionalities at the α -, β -, and *meso*-positions as well as through substitution of the fluorines. As seen in **Fig 1.05**, the addition of functional groups to the BODIPY core can have varying effects dependent upon the placement and symmetry of the substituent [26, 27]. Symmetrical BODIPYs 1 and 3 (underlined numbers are used here to denote the structures in **Fig 1.05**) appear to produce more red-shifted absorption bands than either equally substituted asymmetric counterpart. However, substitution at the *meso*-position does not necessarily result in a spectral change as can be seen by comparing the spectral properties of penta-substituted BODIPY 4 to those of the tetra-substituted BODIPY 3. In the context of 1,3,5,7-tetramethyl BODIPYs such as 4, the *meso* aryl ring lies orthogonal to the BODIPY core for steric reasons resulting in an inductive rather than a mesomeric interaction. Dyes of this type form the main focus of this thesis, since the use of 2,4-dimethylpyrrole as a precursor inhibits the formation of porphyrin rings [26, 27].

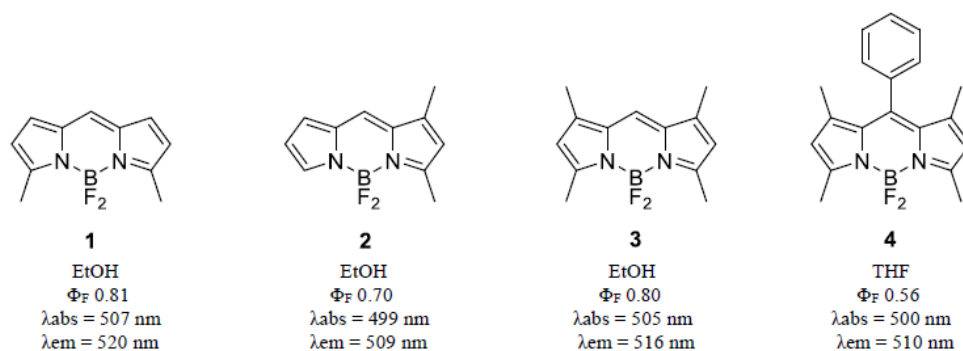


Figure 1.05 The effect of substituents on the absorption wavelengths of simple BODIPYs

(The optical data in the figure are from the previous publications [26, 27]).

Shifts of the main spectral band to the red end of the visible and near infrared (NIR) region are typically achieved through facile modifications to the BODIPY core [26], by extending the degree of π -delocalization with groups that lie co-planar with the π -system. In addition, the emissive behavior of BODIPY fluorophores is greatly influenced by steric and electronic interactions of the substituents. Rotation or rigidity of pendant components, as well as their electron-donating or withdrawing effects on the conjugated core greatly influences both the brightness and absorptive and emissive properties of BODIPY [28]. The development of facile synthetic modifications had led to an intense research focus dedicated to functionally diverse BODIPY dyes.

1.1.1 Halogenation

Non-halogenated BODIPYs tend to have high fluorescence quantum yields, and this is undesirable for the use of BODIPY dyes in singlet oxygen applications such as PDT, which forms one of the main goals of this thesis, as most of the energy absorbed on excitation does not undergo ISC to the triplet state. Consequently, BODIPYs must be structurally modified for use in PDT to enhance the rate of intersystem-crossing (ISC) [29]. It has been demonstrated that the spin-selection rule may be relaxed by attaching a halogen atom to the

BODIPY core, thus producing BODIPYs that undergo ISC and can generate singlet oxygen [29, 30].

The addition of halogen atoms at the 2,6-positions has also been shown to cause a red shift of the main spectral bands [31, 32]. Although halogen atoms are EWGs, they possess lone pairs of electrons and thus act as resonance donators. When added at the 2,6-positions of the BODIPY core, halogens cause destabilization of the highest occupied molecular orbital (HOMO) with respect to the lowest occupied molecular orbital (LUMO), resulting in narrowing of the HOMO–LUMO band gap. In contrast, the LUMO is not affected significantly by substitutions at these positions, since they lie along a nodal plane (**Fig. 1.06**).

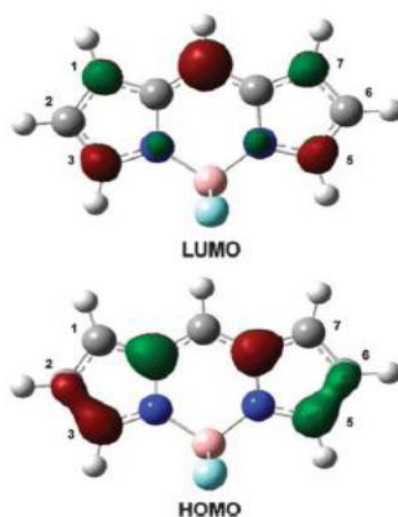


Figure 1.06 Nodal patterns of the HOMO and LUMO of an unsubstituted BODIPY model compound at an isosurface value of 0.07 a.u. Reprinted with permission from reference 33; Royal Society of Chemistry, 2014.

The heavy atom effect may be enhanced by using iodine rather than bromine [11, 34, 35], or by increasing the number of halogen atoms attached to the BODIPY core [36]. However, it has been noted the relationship between the number of halogen atoms and the corresponding spectral effects is nonlinear, with the addition of more than four halogens resulting in no

discernible change in the photophysical properties of the BODIPY [36]. In the absence of steric crowding, the 3,5-positions have been identified as the favored positions for halogenation, followed by the 2,6- and 1,7-positions respectively [36]. However, due to the blocking effects of 1,3,5,7-tetramethyl substituents, the 2,6-positions are favored for halogenation in the context of this study [36].

1.1.2 Substitution of the active methyl groups

BODIPYS generally absorb and emit strongly in the visible region in the 500–550 nm region. This is not desirable for biological and medical applications, it is necessary, therefore, to shift the main absorption band to the red/NIR region of the spectrum, so that it lies in the "biological window", where absorption by water, cells and tissues is at a minimum. Obtaining BODIPY dyes that fluoresce in this region of the spectrum requires the presence of an extended delocalization pathway [5, 37], which occurs in a highly conjugated π -system [24, 38, 39]. As a result of the unevenly distributed MO coefficients at the 3,5-positions (**Fig. 1.06**), substitution at these positions has a greater effect on the energy of the HOMO than that of the LUMO. Extending the π -conjugation at these positions causes a net destabilization of the HOMO with respect to the LUMO, resulting in narrowing of the HOMO–LUMO gap and hence a red-shift of the main absorption band. The most direct method to extend the delocalization pathway is to synthesize pyrrole derivatives bearing phenyl groups at the 3-position [5, 39, 40]. However, it is also possible to add one or more styryl groups to 1,3,5,7-tetramethyl-BODIPY due to the acidity of the methyl groups [5, 39, 41]. This is achieved by condensation of 3,5-dimethyl-BODIPYs with aromatic aldehydes [11, 39], using a modified Knoevenagel condensation reaction [37, 41, 42]. These reactions normally take place under basic conditions and require the removal of water from the mixture. This can be achieved through the azeotropic removal of the water by a Dean-Stark apparatus, or by using

molecular sieves [41, 43]. This condensation process provides direct access to BODIPY derivatives that have red-shifted fluorescence properties [11, 43].

Substitution at the 3,5-positions is of further interest in this work in terms of providing functionality [11]. The inclusion of functional groups at these positions allows for the possibility of conjugation to nanoparticles [44-47], which may be exploited for drug delivery. For example, BODIPYs with sulfur-containing substituents at the 3,5-positions have been used to form BODIPY-gold nanoparticle conjugates [44].

1.2 PDT

The term ‘photodynamic action’ (*‘photodynamische Wirkung’*) was introduced in 1904 by one of the pioneers of photobiology: Professor Hermann von Tappeiner, director of the Pharmacological Institute of the Ludwig-Maximilians University in Munich [48]. The initial application of PDT to the treatment of tumors and other skin diseases, such as lupus of the skin and chondylomata of the female genitalia, was performed by the group of von Tappeiner in 1903-1905 [48]. They attempted to use a number of dyes: eosin, fluorescein, sodium dichloroanthracene disulfonate and ‘Grubler’s Magdalene red’. The dyes were in most cases topically applied, but intratumoral injections were also attempted. Favorable results were reported, however there was no long-term follow-up, and PDT was soon forgotten, probably because of the advent of ionizing radiation in cancer therapy [48]. However, recently PDT has been gaining more attention as an effective treatment approach for some cancers and has been accepted as a clinical treatment in many countries [48].

PDT involves the administration of a tumor-localizing photosensitizing agent, followed by activation of the photosensitizer by light of a specific wavelength. This then results in a sequence of photochemical processes that cause irreversible photodamage to tumor cells (**Fig 1.07**) [46]. The wavelength to excite a photosensitizer dictates how far the light can travel

into the body [46]. Thus, doctors use specific photosensitizers and wavelengths of light to treat different areas of the body with PDT for example, for tumors deep in the body, a photosensitizer that absorb NIR is required.

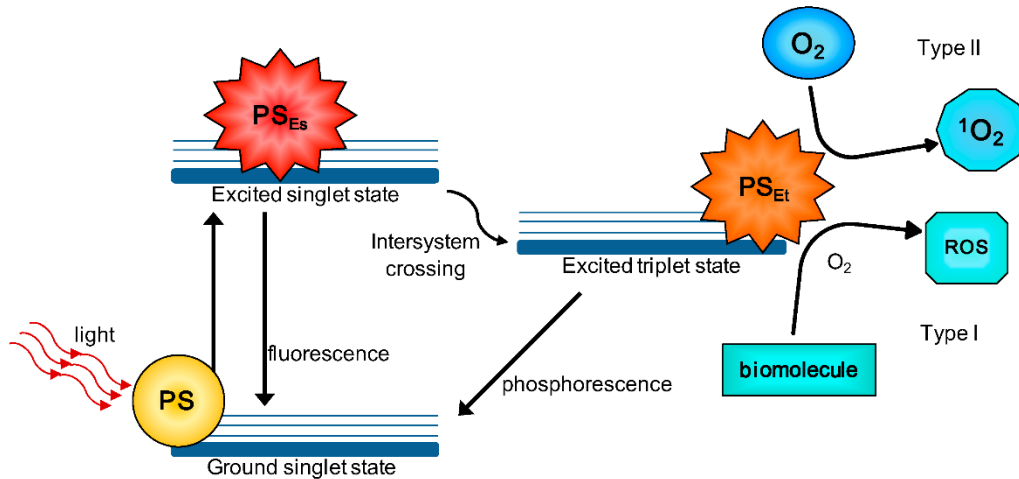


Figure 1.07 Jablonski diagram showing the mechanism of formation of singlet oxygen (¹O₂).

When a photosensitizer decays from the T₁ excited state to the S₀ ground state, a quantum-forbidden spin flip is required; spin is conserved by an energy transfer to molecular oxygen present in the tissue, resulting in the production of highly reactive singlet oxygen. (The figure was obtained from an open source publication reference number [47]).

1.2.1 Research to date on PDT

PDT has been a tremendous success as far as application to treat cancer is concerned [49]. It has been tested for use in oncology to treat different cancers. Many countries have accepted PDT as a form of treatment [49]. PDT research has focused on cancers of the head and neck, brain, lung, pancreas, intraperitoneal cavity, breast, prostate and skin [50]. Since PDT requires the accumulation of a photosensitizer in a tumor, it cannot be used for cancers of the blood or lymphatic system, or for cancers that have spread widely; its principal use is for the treatment of localized tumors [47]. Furthermore, it can only be used to treat tumors that can

be reached using laser light, externally or internally (via endoscope or bronchoscope) as a conventional argon laser can only penetrate about 1 cm into the skin [51].

Porfimer sodium (Photofrin®), a hematoporphyrin derivative (HpD), was the first photosensitizer to receive approval and is now licensed for use in the treatment of a number of cancers [50-52]. However, it is only moderately active in tissue, as its absorption band in the red region of the visible spectrum is very weak. Photofrin® and other HpDs are known as first generation sensitizers mainly because they exist as complex mixtures of monomeric, dimeric, and oligomeric structures, and the intensity of light absorption at the maximum wavelength is low [51]. The long-term skin phototoxicity lasts six to ten weeks, during which time sunlight and strong artificial light exposure should be avoided [51]. Second-generation synthetic photosensitizers were developed to address the issues of unfavorable skin phototoxicity, low absorption in the red region of the visible spectrum, as well as the complex mixtures arising from synthetic methods. Second-generation photosensitizers have shorter periods of photosensitivity, longer activation wavelengths that allow for deeper penetration of tissue, higher singlet oxygen quantum yields, and better selectivity. The groups that have been most actively investigated are the chlorins, texaphyrins, purpurins, and phthalocyanines (Pcs) [50-52]. It is worth noting that as of 2013, no non-porphyrin sensitizer had been approved for PDT applications [50-52]. Porphyrinoid compounds include chlorins, bacteriochlorins, Pcs, and other related structures [50-52].

1.2.2 BODIPY dyes in PDT

There is a need to develop more efficient photosensitizers for PDT. The photosensitizers that have been tried and tested have a number of drawbacks. For example, Pcs are very efficient but they are far from ideal because their main absorption band lies at the edge of the therapeutic window, hence most of the photosensitizers that have been used for PDT have

been on the surface of the skin. Developing photosensitizers that absorb strongly in the heart of the optical window, would result in PDT being applied to deeper lying tissues. To address this, the objective of this project is to develop a BODIPY dye [11, 33] that can be conjugated to UCNPs so that photons absorbed in the NIR region can be used to generate singlet oxygen. By matching the emission bands of the UCNPs with the absorption bands of the BODIPY, efficient Förster resonance energy transfer (FRET) results in the excitation of the BODIPY chromophore in a manner that leads to efficient ISC to the triplet state if heavy atoms such as bromine or iodine are incorporated onto the BODIPY chromophore. This should result in the efficient formation of singlet oxygen, so that the conjugates can be used as photosensitizers for PDT [46]. In this work, UCNPs are conjugated with a carboxylic acid substituted BODIPY dye with a high singlet oxygen quantum yield so that the potential utility for PDT can be explored.

1.3 Nanoparticles

Nanoparticles by definition range between 1 and 100 nm in size. They consist of an interfacial layer, which fundamentally affects the properties of the nanoparticles. In contrast to other types of nanoparticles, the size of UCNPs is directly proportional to the quantum efficiency [53-56]. The theory on how the upconverted energy is achieved is described below.

1.3.1 UCNPs

UCNPs are nanoparticles that absorb low energy wavelength and emit high energy wavelengths. This process is what is referred to as photon upconversion [53]. In other words, absorption can occur in the infrared, while emission occurs in the visible or ultraviolet regions of the electromagnetic spectrum. The phenomenon of upconversion was first described by François Auzel who demonstrated that incident photons of infrared light could

be upconverted into a photon of visible light in ytterbium–erbium and ytterbium–thulium systems [53], by expanding on Bloembergen's earlier work, which suggested that energy transfer could occur between ions in their excited state [53, 54]. Later developments of UCNPs have been made on lanthanides, actinides, and sometimes transition metals. What makes these metals suitable is their ability to have a longer-lived excited state, which encourages excited state absorption (ESA) and energy transfer between ions in the excited state [53, 54].

For this work, we focus on lanthanides as they have proven to have superior properties when compared to actinides and transition metals. The lanthanides employed here are erbium (Er^{3+}), ytterbium (Yb^{3+}), yttrium (Y^{3+}) and gadolinium (Gd^{3+}). UCNPs consist of a host matrix, and dopants, with Erbium (Er^{3+}) as the activator and ytterbium (Yb^{3+}) as the sensitizer [53, 54].

1.3.2 Upconversion in the lanthanides

Generally, upconversion phosphors are composed of rare earth elements or transition metals [53-56]. However, transition metals are not as common, because their orbitals are involved in both luminescence and bonding, making them extremely vulnerable to environmental influence [56]. On the other hand, trivalent rare earth metals are ideal candidates for use as upconversion phosphors [56], since their 4f orbitals that are shielded from environmental interactions, by the 5s and 5p orbitals, and as a result they do not participate in bonding [54, 56]. This is what characterizes the long lived excited states of trivalent rare earth metals [56]. This property is what is of utmost importance for the upconversion process to occur, and this will be discussed in detail in **Section 1.3.3**.

1.3.3 Activators, sensitizers and host matrix

In most cases, lanthanide upconverting materials consist of an inorganic crystal host lattice composed of lanthanide dopants, which act as luminescent centers [54]. The dopants in the host lattice of the most efficient upconverting materials are trivalent lanthanide ions [53, 54]. In most cases there are two lanthanide species that take part in the upconversion process, and these are referred to as the activator and the sensitizer [53, 54]. The sensitizer ion is responsible for absorbing energy from the light source and transferring that energy to the activator ion. The activator ion must possess a long-lived excited state to allow for re-excitation to a higher energy state, while it is still in its first excited state. In other words a good activator ion is one that has its 4f orbitals shielded from environmental interactions to allow for minimum vibrations [53-56]. Thus, desirable activators in the lanthanide series include Er^{3+} , Tm^{3+} , and Ho^{3+} ion [56]. Desirable, sensitizers must have one excited state and its energy must match that of the activators [56]. Yb^{3+} has been found to be the most effective sensitizer ion. The sensitizer ion transfers its energy to the activator ion through energy transfer upconversion (ETU) [56].

The concentration of the activator and the sensitizer ions is of fundamental importance, because it affects the proximity of the activator and the sensitizer [57]. Generally, activator concentrations are kept low (2 mol %) as compared to sensitizer ion concentrations which range between (18-22) mol % [50, 57, 58].

The host matrix also referred to as the host lattice brings the two luminescent centers into close proximity to allow for an effective energy transfer between the ions [56, 58]. The most suitable host matrix for efficient upconversion must have low phonon energy and high chemical stability [56, 58]. Fluorides have demonstrated to be the best host matrix [54, 56]. For the purposes of this thesis, NaYF_4 was used as a host matrix. NaYF_4 has two types of

crystalloid phases at ambient pressure: the cubic α -phase and the hexagonal β -phase [54, 56, 58]. The β -phase has been reported as the most thermodynamically stable [54, 56]. Generally, the β -NaYF₄ can be obtained via a heating treatment such as annealing, hydrothermal or solvothermal treatments, often requiring harsh conditions with high reaction temperatures and long reaction times [54-58]. In this work, the hexagonal β -NaYF₄ is favored, so the hydrothermal treatment was used.

1.3.4 Mechanisms of upconversion

The fluorescence that results from the upconversion process is counterintuitive to conventional fluorescence. In conventional fluorescence, in line with Stokes law, the energy of the emitted photons is less than the energy of the exciting photons [59]. The process employed in upconversion is known as an anti-Stokes process, because the emitted photons have higher energy than the exciting photons. The anti-Stokes process is achieved through a number of processes, which include energy transfer up-conversion (APTE or ETU), multi-step excitations from ESA, cooperative upconversion, and photon avalanche (PA) [53]. For the lanthanide doped UCNPs, the main process involved is ETU [53]. As a photon of appropriate energy is absorbed by the sensitizer ion, the next step is to transfer the energy of the incident photon from the sensitizer ion through a radiative or non-radiative energy transfer. The activator ion has a long-lived excited state, and this results in the activator ion absorbing an additional photon in its excited state as seen in **Fig 1.08**. Finally, because of the very strong vibration in the crystal at this stage as the ion is also in its second excited state, the electron is relaxed back to the ground state and in the process it releases a photon with double the energy of the initial photon. This anti-Stokes process arises because of ETU [53, 54].

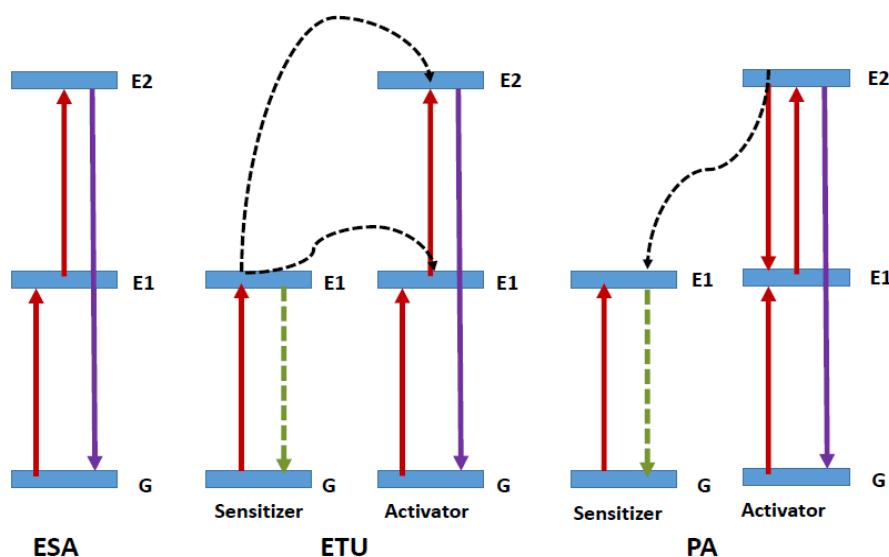


Figure 1.08 The differences between the three upconversion processes: ESA, ETU, and PA.

ETU involves a sensitizer, which is the first ion to be excited, and an activator, which is the ion to which energy is transferred. The proximity between these ions must be very small and the power of the light source must be high for effective energy transfer [53]. The power source is of critical importance because it greatly increases the probability of energy transfer to occur between the sensitizer and the activator. Laser light is typically used for this reason.

Within the ETU process studied in the context of UCNPs in this study, the energy transfer can either be radiative, non-radiative or phonon-assisted (**Fig 1.08**). However, phonon-assisted is less likely. For radiative energy, the transfer a phonon is involved. The process occurs when a phonon is emitted by the sensitizer and absorbed by the activator and hence is dependent on the sample shape. Longer dimensions allow for a greater possibility for absorption by the activator [54, 59]. Depending on the spectral overlap of the sensitizer and the activator, the shape of the sensitizer emission will change according to the activator concentration [54]. This means radiative and nonradiative energy transfer can be distinguished by analyzing reabsorption effects. **Equation 1** gives the probability for an energy transfer to occur as a function of distance R

$$P_{SA}(R) = \frac{\sigma}{4\pi R^2 \tau_s} \int g_s(V) g_a(V) dV \quad (1)$$

where τ_s is the sensitizer lifetime, σ is the absorption cross-section, and the integral is the spectral overlap between S and A. The R^2 distance dependence between the ions helps to determine their optimal concentration levels, as well as determining the suitability of various host lattices based on interatomic distances [53, 54].

Nonradiative energy transfer involves two ions interacting with each other, which is quite different from the radiative process, in which the sensitizer and the activator need not interact as can be seen in **Fig 1.08**. Given enough ion interaction, the excitation will jump from one ion to another [50]. The probability for energy transfer goes as:

$$P_{SA}(R) = \frac{\left(\frac{R_0}{R}\right)^n}{\tau_s} \quad (2)$$

where τ_s is the sensitizer lifetime and R_0 is the critical transfer distance for which excitation transfer and spontaneous deactivation of the sensitizer have equal probability [53, 54]. The exponent, n , is an integer that varies as $n = 6$ for dipole-dipole interactions, $n = 8$ for dipole-quadrupole interactions and $n = 10$ for quadrupole-quadrupole interactions.

A photon assisted energy transfer is quite different from the two energy transfer processes discussed above (**Fig 1.08**). The probability for energy transfer should go to zero as the energy integral overlap goes to zero (**Equation. 1**), however, it can still take place for small energies (0.01 eV) provided energy is conserved through production and annihilation of a few phonons. In rare-earth (RE) ions, however, energy differences an order of magnitude higher are possible and so multiphonon processes must be considered [53].

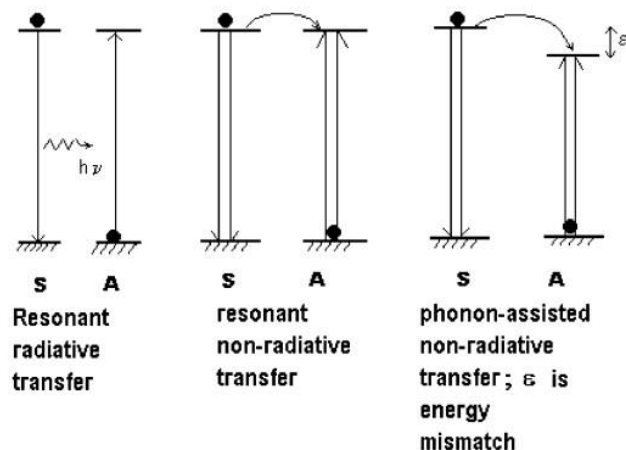


Figure 1.09 Upconversion processes. Reprinted with permission from reference 53; Chemical Reviews, 2014.

1.3.5 Synthesis and surface modification

Generally, RE-doped NaYF₄ UCNPs that are synthesized using the thermal method are not water soluble, because of the organic ligands that are used such as oleic acid (OA) [60]. To achieve water solubility these nanoparticles need to be functionalized with hydrophilic groups such as carboxyl or amino groups [60-65]. Additionally, functionalizing UCNPs with amine groups allows for conjugation between the UCNPs and biomolecules. The functionalization of the UCNPs can be achieved either through surface modification with an inorganic shell layer, or surface modification with organic capping ligands [60-65]. In most cases, an inorganic silica shell is used for surface modification and this is called silanization [66]. In this procedure, the surfaces of synthesized nanoparticles (NPs) are further coated with amorphous silica [62, 67]. The hydrolysis and condensation of siloxane precursors, such as tetraethoxysilane (TEOS) in the presence of ethanol and ammonia, has been extensively used for the surface silanization of UCNPs [66, 67]. Although coating the surface of NPs with silica allows them to be water dispersible, it may not provide the required functional groups for conjugation to the photosensitizer dye. To overcome this problem, the hydrolysis

of aminosiloxanes such as (3-aminopropyl) triethoxysilane (APS) is often performed to generate functional amino groups on the surface of the silica-coated NPs [63, 65].

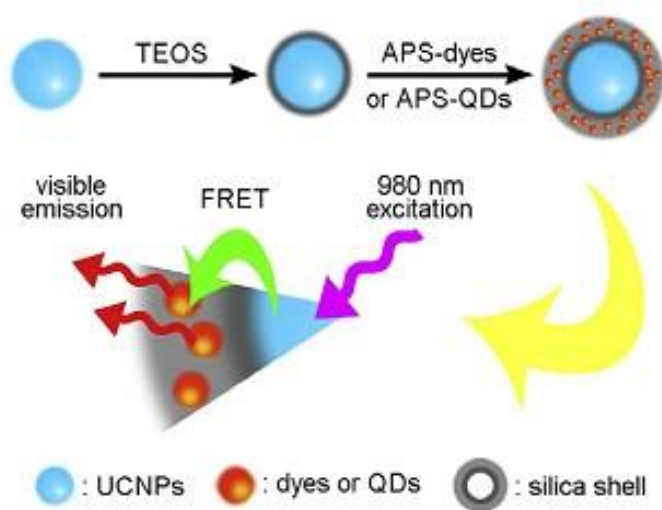


Figure 1.10 Schematic illustration of silica coated multicolor UCNPs based on the FRET mechanism. Reprinted with permission from reference 67; Nanotechnology, Biology and Medicine, 2011.

1.3.6 Applications

The ability of UCNPs with different dopants to generate various high energy emission bands from low energy excitation is sought after in many applications. They have seen successful applications in the fields of lasers [68, 69], photovoltaic solar cells as well as more unusual areas such as anti-counterfeiting [70]. Currently, UCNPs have been studied for security and molecular memory switches [71, 72]. Most importantly from the standpoint of this study, UCNPs have also found applications in various biomedical fields because their absorption in the NIR region gives them an extremely favorable signal to noise ratio [73-76]. Most biological samples display autofluorescence upon UV excitation. UCNPs not degradable under ambient light or temperatures, the nanoparticles exhibit excellent photostability and the luminescence capability of UCNPs can be applied to a variety of in vitro assays displaying a

lower detection limit by comparison to conventional methods [73, 74]. These desirable properties are a result of the three fundamental factors that have been incorporated in the UCNPs synthesized in this work, that is: the nature of the dopants (which bring about the upconversion process), the host matrix (which keep the luminescent centers in close proximity for efficient energy transfer between the sensitizer ion and the activator ion) and the size and phase of the UCNPs (which ensures high efficiency of the UCNPs). The combination of all these factors bring about the desirable properties that have been discussed.

In this work, we have functionalized UCNPs with amine groups to allow for conjugation. In addition, this amine layer provides water solubility for the nanoparticles, which is desirable as biological applications are concerned.

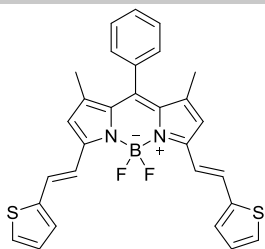
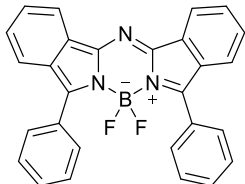
1.4 BODIPY dyes for NLO applications

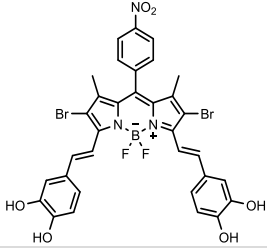
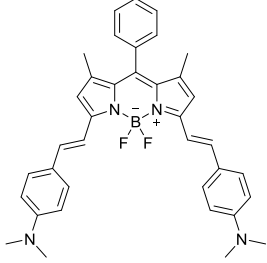
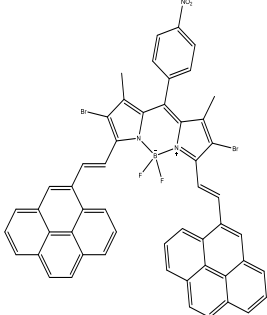
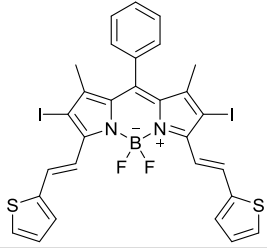
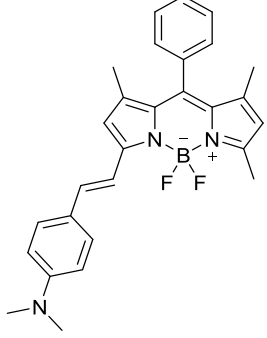
The success of laser research has been a great asset to society. However, with this positive success comes some negative unintended consequences due to the widespread availability of cheap and powerful lasers. Irresponsible members of the general public have been shining laser pointers at aircraft during their landing approach [77]. Since there is a need for protection against intense incident laser pulses, there has been a strong research focus on OL materials that limit the intensity of laser light so that it is not harmful to the vision of pilots and sensitive optical equipment [77]. The focus in this study is on developing OL materials that can limit the transmittance of nanosecond pulses of the second harmonic of Nd:YAG lasers at 532 nm, which is one of the most problematic wavelengths from a laser safety standpoint, while remaining largely transparent under ambient light conditions. Many materials including quantum dots, Pc, BODIPYs and other semiconductors and dyes have been studied for OL [77-86]. In this study, the OL properties of BODIPY dyes are explored along with a study of how the effect of structural modifications on the photophysical

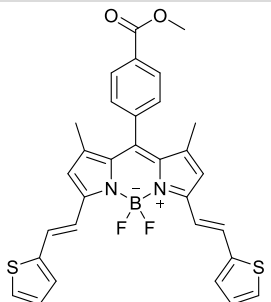
properties affect the OL properties. Dyes which possess intense two-photon absorption (2PA) properties under intense illumination have been shown to possess good OL behavior, thus there is a need to design and develop novel dyes with strong 2PA properties [78].

Comparatively little research has been carried out to date in exploring the effect of donor and acceptor groups on the OL properties of BODIPY dyes. Other researchers have reported on the effect of heavy atoms on the OL properties of BODIPY dyes [77]. Recently aza-BODIPY dyes have been explored at 532 nm [78]. However, not much has been done to explore the effect of push-pull effects on the OL properties of BODIPY dyes and this is what we seek to explore in this work.

Table 1.01 BODIPY dyes whose nonlinear properties have been reported in the literature.

Compound	Method	Solvent /Matrix	NLO Behavior	Wavelength λ / nm	Ref
	Z-SCAN	DMF	RSA	532	[77]
	Z-SCAN	PBC	RSA	532	[77]
	Z-SCAN	DMSO THF Benzene Toluene DCM EtOAc CNCH ₃	RSA	532	[78]
		PBC PMMA PS			

	Z-SCAN	DCM	RSA	532	[79]
	Z-SCAN	THF	RSA	532	
	Second harmonic generation response: Rotational Marker fringe technique Third harmonic response: comparative model	PMMA	RSA	1064	[80]
	Z-SCAN	DCM	RSA	532	[79]
	Z-SCAN	THF	RSA	532	[77]
	Z-SCAN	PBC	RSA	532	
	Z-SCAN	THF	RSA	532	[80]
	Second harmonic generation response: Rotational Marker fringe	PMMA	RSA	1064	

	technique Third harmonic response: comparativ e model				
	Z-SCAN	DMF	RSA	532	[77]
	Z-SCAN	PBC	RSA	532	

1.4.1 Mechanisms in OL

An important parameter in determining the suitability of materials for use as OL materials is the limiting threshold intensity (I_{lim}), which may be defined as the input fluence (or energy) at which the transmittance is 50% of the linear transmittance, **Fig. 1.11** [81]. The lower the I_{lim} value, the better the material as an optical limiter. Surprisingly, it has been observed that this important OL parameter is only sparsely reported in the literature [82]. Ideally, the output energy of a limiter rises linearly with the input energy until a threshold I_{lim} is reached as shown in **Fig. 1.12**. Ideally, after the I_{lim} threshold is achieved, the output energy is restricted to a given value, for all input intensity beyond the I_{lim} .

The main mechanisms used to achieve OL are nonlinear absorption (NLA), nonlinear refraction (NR) and nonlinear light scattering (NLS). However, the focus of this thesis is on the use of BODIPY dyes as OL materials due to NLA processes that occur on the nanosecond timescale.

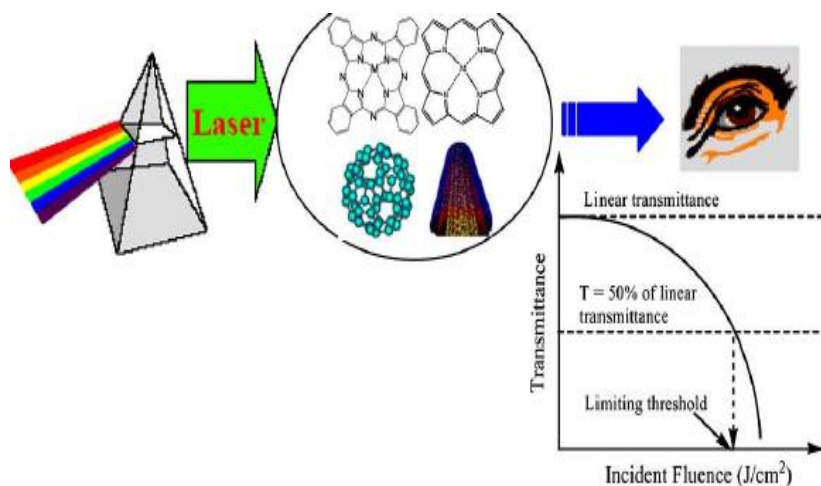


Figure 1.11 The behavior and definition of an optical limiter. Reprinted with permission from reference 83; Journal of Chemical Physics, 1968.

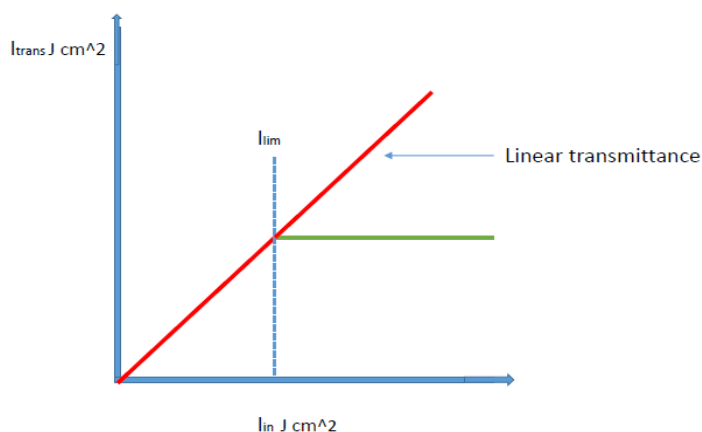


Figure 1.12 The behavior of an ideal optical limiter, I_{trans} = transmitted fluence, I_{lim} = incident fluence.

Materials with a positive nonlinear absorption coefficient exhibit a reverse saturable absorption (RSA) mechanism with a decrease in transmittance at high-intensity levels, and so operate as optical limiters [83]. 2PA described by the imaginary part of the third-order susceptibility ($\text{Im}[\chi^{(3)}]$) would account for the OL of the BODIPY dyes, if a femtosecond laser were being used. However, excited-state absorption (ESA), which results from the absorption of photons by an excited state, constitutes the fundamental mechanism for RSA

and OL in BODIPY dyes on the nanosecond timescale [83]. For BODIPYs that undergo ISC to the triplet-excited state, ESA may occur in the triplet manifold (**Fig. 1.13 A**). However, this is unlikely to be the OL mechanism for BODIPYs in the absence of halogen substituents at the 2,6-positions. For these non-halogenated BODIPYs, OL activity is likely due to ESA and 2PA in the singlet manifold (**Fig. 1.13 B**)

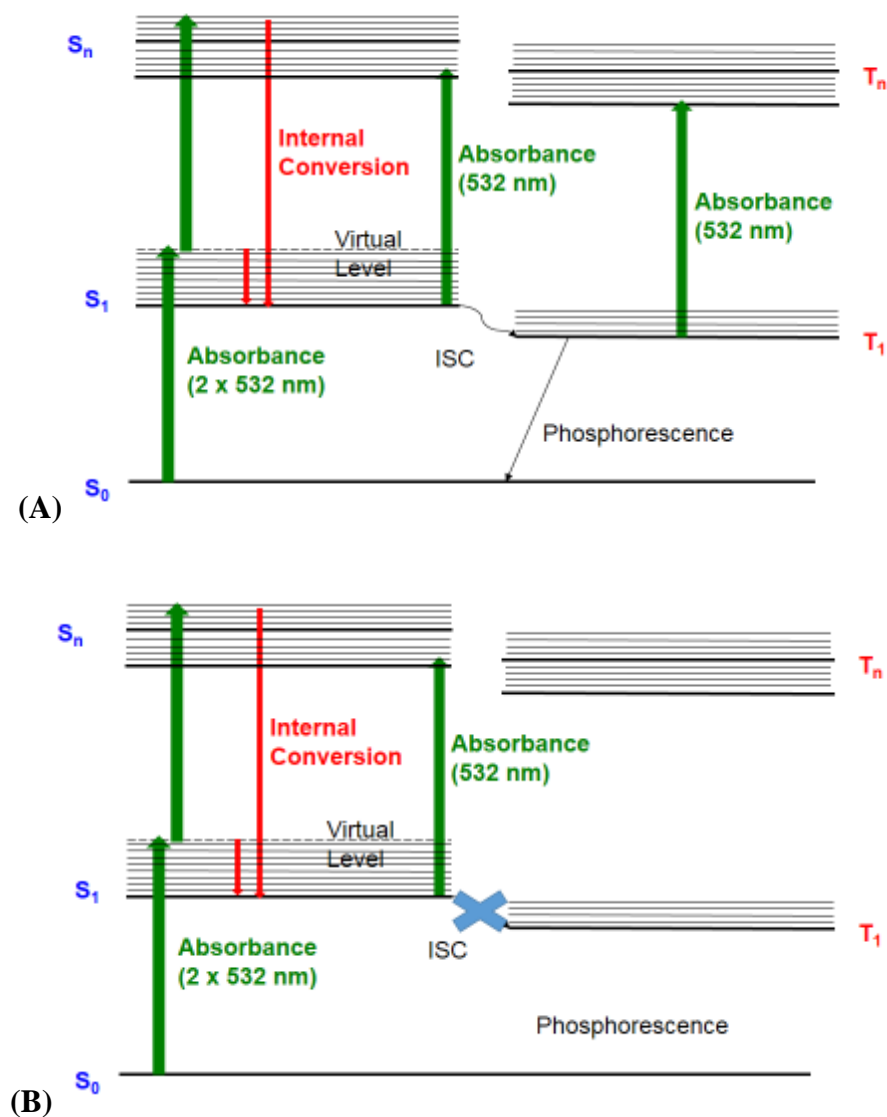


Figure 1.13 Jablonski diagrams showing potential OL process mechanisms for (A) BODIPYs with halogens at the 2,6-positions that are likely to have a populated triplet excited state and (B) non-halogenated BODIPYs that do not undergo ISC to the triplet excited.

Another OL process that is common with semiconductor materials is the free-carrier absorption (FCA), which does its limiting action via a similar mechanism as the ESA, but uses both the electrons and holes generated upon excitation. These electrons and holes may recombine to produce fluorescence or serve as absorbing ‘carriers’ in the conduction (electrons) and the valence (holes) bands for the incident light (**Fig. 1.14**). A good free-carrier absorber would have high free-carrier generation and a long recombination time.

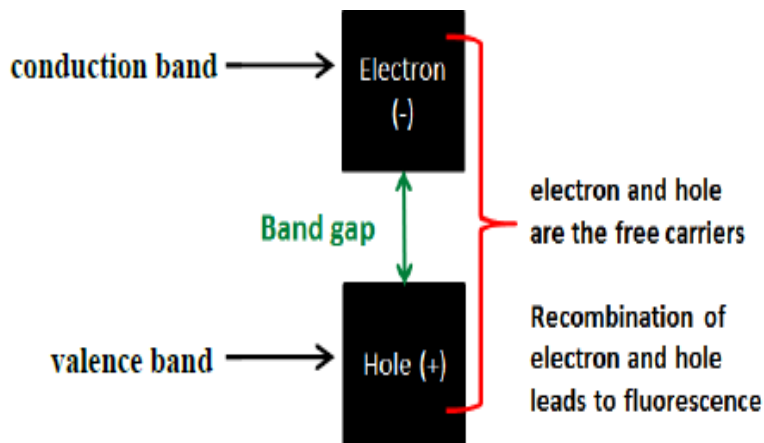


Figure 1.14 Free-carrier absorption (FCA) in a semiconductor material.

1.4.2 The Z-scan as analysis technique

The Z-scan technique (**Fig. 1.12**) developed by Sheik-Bahae et al. [85-87] is one of the simplest and the most sensitive techniques for the determination of the third-order nonlinearities of materials. The set-up, when used in conjunction with a suitable pulsed laser allows one to measure the nonlinear absorptive or refractive property of a material. It works on the principle of moving the sample under investigation through the focus of a tightly focused Gaussian beam with the following background assumptions:

- a) The experiment assumes only a $\text{Im}[\chi^{(3)}]$ nonlinearity.
- b) It assumes a Gaussian spatial and temporal pulse, and

c) It assumes that the sample length is smaller than the Rayleigh length (the “thin” sample concept). In order for the sample to be considered “thin,” the pathlength through the sample must be shorter than the Rayleigh length (z_0). In this particular setup, it means that the sample cannot exceed 0.2 cm.

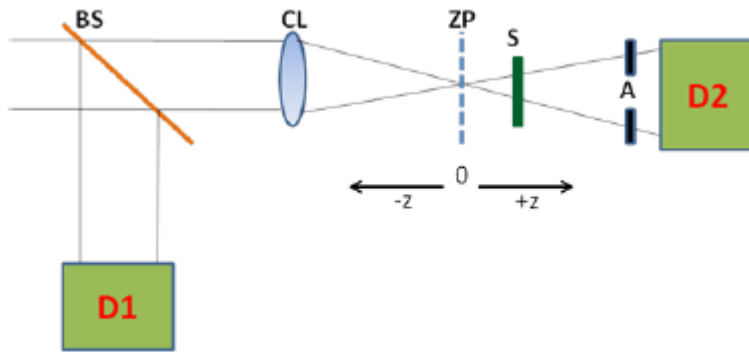


Figure 1.15 Schematic diagram of a basic Z-scan set-up. Beam splitter (BS), convex lens (CL), zero position (ZP), sample holder (S), aperture (A), reference (D1) and probe detector (D2). The $-z$ to $+z$ describes the movement of a sample along the z -axis through the focus (ZP) of the lens.

The Z-scan method has been used to determine the sign and magnitude of both the real and imaginary parts of third-order NLO susceptibility [85-90]. The real part can be assigned as the nonlinear refractive index of the material, whereas the imaginary part represents the nonlinear absorption coefficient.

In **Fig 1.15**, a single laser beam in tight focus geometry is used. The tight geometry is provided primarily by the relative position of the convex lens (CL) to the sample holder, the three directing mirrors (not shown in the figure), and the two detectors (D1 and D2). In this system, there is an optical gain because the fluence at the focal plane (ZP) is much greater than that at the input (D1). The relative transmission, which is the ratio of the transmitted

intensity to the incident intensity ($D2/D1$) of a nonlinear medium is recorded as a function of its position z and measured with respect to the focal plane (ZP) of the incident beam.

Depending on whether there is an aperture (A) or not, two different basic experiments can be performed with the experimental set-up (**Fig. 1.15**). The presence of an aperture (the closed aperture technique) makes the experiment sensitive to both nonlinear absorption and nonlinear refraction. Without the aperture (the open aperture technique), all the transmitted beams are collected onto the detector ($D2$), and the sensitivity to nonlinear refraction is completely removed. In the open aperture technique, changes in the relative transmission ($D2/D1$) are due only to nonlinear absorption. Hence, the open aperture technique was employed throughout in this work.

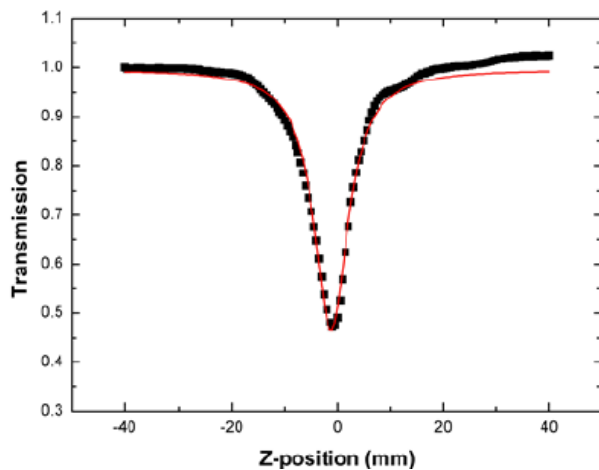


Figure 1.16 A typical open aperture Z-scan profile depicting a positive nonlinear.

Fig 1.16 shows a typical open aperture Z-scan curve for a material with a positive nonlinear absorption coefficient. The red solid line in the figure shows the theoretical fit to the experimental data. Details about the appropriate equations to fit the data will be provided later in this section. The strongest absorption is found when the sample is at position $z = 0$, ZP , and shows a minimum transmission at this position. This thus demonstrates an intensity dependent RSA process. The opposite effect, which is not the focus of this work, saturable

absorption (SA), is found for materials with a negative nonlinear absorption coefficient, wherein the relative transmission increases with increasing incident intensity and has a maximum at the focal plane (ZP). By moving the sample along the z-axis through the focus in an open aperture Z-scan experiment, the intensity-dependent absorption is measured as the change of the transmission through the sample using a detector in the far field (D2). On approaching the focus, the intensity increases by several orders of magnitude relative to the intensity away from the focus, thus inducing nonlinear absorption in the sample. An important limitation of the Z-scan technique is the inability to separate the various mechanisms (ESA, 2PA, FCA, NLR, and/or NLS) responsible for the RSA process. To address this limitation, general equations for analysis have been developed, and the explanation of results from such analyses are usually provided based on a careful consideration of the nature of the investigated material and the properties (pulse width and repetition rate) of the laser beam employed [85-90].

The Z-scan technique employed for the determination of the third-order nonlinearities of materials is the one developed by Sheik-Bahae et al. [85-87]. This is one of the simplest and the most sensitive techniques for studying OL materials. The dyes showed no sign of band broadening due to aggregation and there were no issues with solubility, so NLS due to aggregation is not anticipated, and NLA is anticipated to be the mechanism of interest for the BODIPY dyes that were studied.

The measured quantity in an open-aperture z-scan experiment is the normalized transmittance, given by **Equation 3** for a Gaussian pulse [85-90].

$$T(z) = \frac{1}{\sqrt{\pi}q_0(z)} \int_{-\infty}^{\infty} \ln[1 + q_0(z) e^{-\tau^2}] d\tau \quad (3)$$

where $q_0(z)$ is a parameter characterizing the strength of the nonlinearity and is given by **Equation 4** when using a circular Gaussian beam [85-87].

$$q_0(z) = \frac{2\beta P_0 L_{\text{eff}}}{\pi w^2(z)} \quad (4)$$

Where β is the nonlinear absorption coefficient of the material, P_0 is the peak power of the pulses and L_{eff} is the effective pathlength in the sample, given by **Equation 5**:

$$L_{\text{eff}} = \frac{1 - e^{-\alpha L}}{\alpha} \quad (5)$$

where α is the linear absorption coefficient. For applications of these materials, α should always be measured at the intended wavelength in this case, 532 nm. In **Equation 2**, $w(z)$ is the beam width as a function of the sample position, and is given by

$$w(z) = w_0 \cdot \sqrt{1 + \left(\frac{z}{z_0}\right)^2} \quad (6)$$

where w_0 is the beam waist at the focus ($z = 0$), defined as the distance from the beam centre to the point where the intensity reduces to $1/e^2$ of its axis value; while z and z_0 are the translation distance of the sample relative to the focus, and Rayleigh length, respectively. The Rayleigh length is defined as $\pi w_0^2 / \lambda$ where λ is the wavelength of the laser. **Equations 1–4** are used to determine the nonlinear absorption coefficient β_{eff} from experimentally measured normalized transmittance. β_{eff} takes into account all the processes that result in a NLO response on the nanosecond timescale such as ESA, which makes it more suitable than β . Since Equation 3 cannot easily be applied, an analytical formula is typically used to fit the z-scan data, which is given by **Equation 5**:

$$T(z) = \tag{7}$$

$$0.36e^{\left\{-\frac{q_0(z)}{5.60}\right\}} + 0.286e^{\left\{-\frac{q_0(z)}{1.21}\right\}} + 0.213e^{\left\{-\frac{q_0(z)}{24.62}\right\}} + \\ 0.096e^{\left\{-\frac{q_0(z)}{115.95}\right\}} + 0.038e^{\left\{-\frac{q_0(z)}{965.08}\right\}}$$

Equation 7 provides values of q_0 directly from the normalized transmittance $T(z)$.

Substituting **Equation 6** into **Equation 4** gives $q_0(z)$ as follows:

$$q_0(z) = \frac{Q_0}{1 + \left(\frac{z}{z_0}\right)^2} \tag{8}$$

where

$$Q_0 = \frac{2\beta P_0 L_{\text{eff}}}{\pi w^2(z)} = \frac{2\beta P_0 L_{\text{eff}}}{\lambda z_0} \tag{9}$$

Equation 9 gives a Gaussian plot with Q_0 as the maximum value at the beam waist ($z = 0$).

The peak value and the FWHM of the plot give values of Q_0 and z_0 respectively. The β value may then be calculated using **Equation 10** [87].

$$\beta = \frac{\lambda z_0 Q_0}{2P_0 L_{\text{eff}}} \tag{10}$$

The imaginary component of the third order susceptibility, $\text{Im}[\chi^{(3)}]$, is directly proportional to β , as seen in **Equation 11** [84]:

$$\text{Im}[\chi^{(3)}] = \frac{\eta^2 \epsilon_0 c \lambda \beta}{2\pi} \tag{11}$$

where η and c are the linear refractive index and speed of light, respectively, and ϵ_0 is the permittivity of free space. The third-order NLO susceptibility is used to describe ultrafast

responses, with nonlinear absorption being described by the imaginary component, while the real component is representative of the nonlinear refraction of the material [86, 87]. While $\text{Im}[\chi^{(3)}]$ describes the speed of the NLA response of the material, the behavior at a molecular level may be described using hyperpolarizability (γ), which describes the nonlinear absorption per mole of the OL compound, and is useful when comparing efficiencies of different optical limiters. The relationship between $\text{Im}[\chi^{(3)}]$ and γ is shown in **Equation 12** [87]:

$$\gamma = \frac{\text{Im}[\chi^{(3)}]}{f^4 C_{\text{mol}} N_A} \quad (12)$$

where N_A is Avogadro's constant, C_{mol} is the concentration of the active species in the excited state per mole, and f is the Lorentz local field factor, $f = (\eta^2 + 2)/3$.

It makes sense that a good optical limiter would be those compounds exhibiting lower I_{lim} values, as this means that the limiting would occur at a lower intensity, allowing for more cautious protection of sensors. The International Commission on Non-Ionizing Radiation Protection has published a guideline [89] giving insight into exposure limits for a variety of lasers. This work deals with 10 ns pulses of light at 532 nm derived from an Nd:YAG laser with a second harmonic generation crystal and, as such, its exposure limit can be determined from **Equation 13**, which gives the exposure limit as a function of time.

$$2.7 C_A t^{0.75} \text{ J/cm}^2 \quad (13)$$

C_A is a correction factor (= 1 for lasers with wavelengths of 400–700 nm). For this work, the exposure limit was determined to be 0.95 J cm^{-2} assuming a 0.25 s exposure time. This exposure time was defined as the average human response time (blink reflex) to a sudden flux

of light into the eye [88]. Irradiance has units of W cm^{-2} , with the maximum value occurring at the focus ($z = 0$), determined by **Equation 14** [87].

$$I_{00} = \frac{E}{\tau \cdot \pi \cdot w_0^2} \quad (14)$$

where E is maximum laser energy (J), τ is the length of the laser pulse (s) and w_0 is beam waist (cm). As $1 \text{ J/s} = 1 \text{ W}$, the maximum irradiance has units of W cm^{-2} . For any given z -scan experiment, the laser energy (J) remains constant and hence, the overall laser power ($\text{J/s} = \text{W}$) also remains constant. However, the irradiance varies with z , as the beam width depends on the distance from the focus. The cross-sectional area of the beam is circular and hence equal to $\pi \cdot w(z)^2$. Multiplying the irradiance by the corresponding beam area gives the laser power, P . At the focus ($z = 0$), P is given by **Equation 15** [87].

$$P = I_{00} \cdot \pi w_0^2 \quad (15)$$

At any other z position, P is given by **Equation 16** [87].

$$P = I_{\text{in}}(z) \cdot \pi w(z)^2 \quad (16)$$

As P remains constant throughout any given z -scan run, **Equation. 15** and **Equation. 16** may be combined and simplified as shown in **Equation 17** [87]:

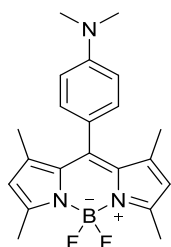
$$I_{\text{in}}(z) = I_{00} \cdot \left(\frac{w_0}{w(z)} \right)^2 \quad (17)$$

As the transmittance value gives the percentage of light that passes through a material, the output fluence ($I_{\text{out}}(z)$) may be calculated by finding the product of $I_{\text{in}}(z)$ and the transmittance corresponding to each z position ($T(z)$) (**Equation 18**) [87].

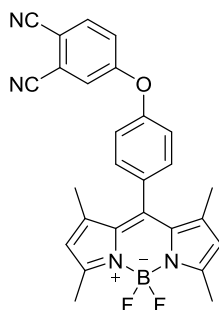
$$I_{\text{out}}(z) = I_{\text{in}}(z) \cdot T(z) \quad (18)$$

1.4.3 BODIPY dyes used in this work for NLO studies

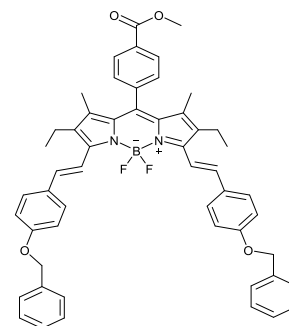
BODIPY (**4**) and (**6**) were studied to compare effect electron donating groups and electron withdrawing groups on as far as OL is concerned. The numbering system follows the sequence used in later chapters and parentheses denotes dyes that were synthesized as part of this study. BODIPY (**4**) and (**6**) can be referred to as D- π -A and A- π -A BODIPY cores respectively where D stand for donor group, π for the BODIPY parent core and A for acceptor group. BODIPY (**10**), (**16**), and (**18**) were studied to compare styryl-extended BODIPYs with push-pull effects of differing magnitudes, herein referred to as D- π -A styryl-extended BODIPYs with push-pull effects of differing magnitudes. BODIPY (**11-14**) were studied to investigate the effect of ESA in the singlet manifold and in the triplet, manifold and this work was recently published [91].



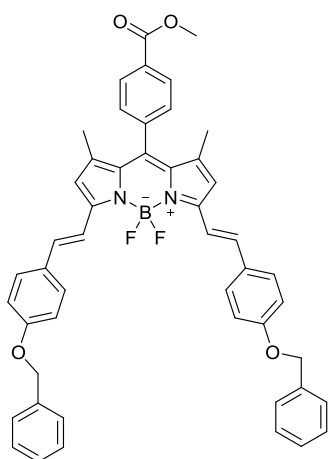
(4)



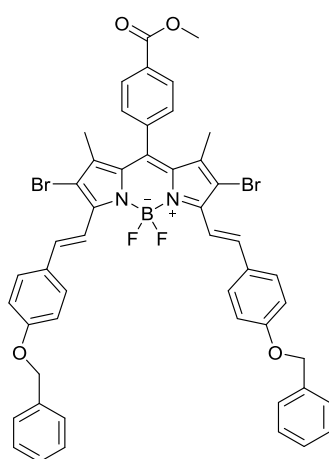
(6)



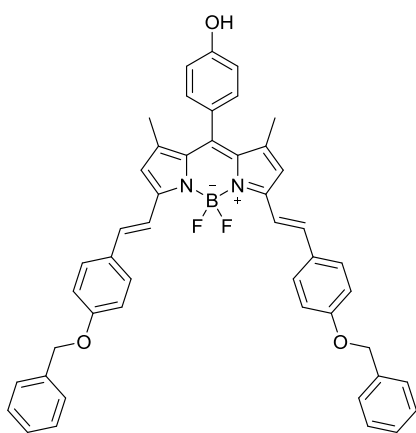
(10)



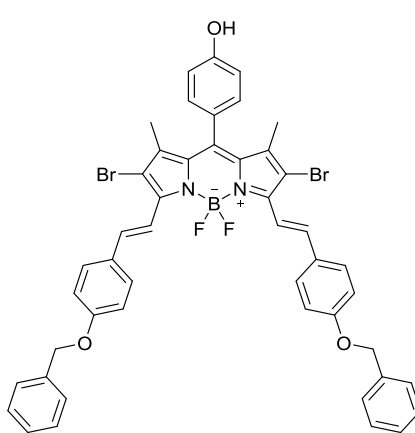
(11)



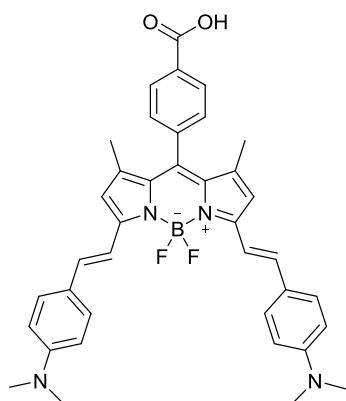
(12)



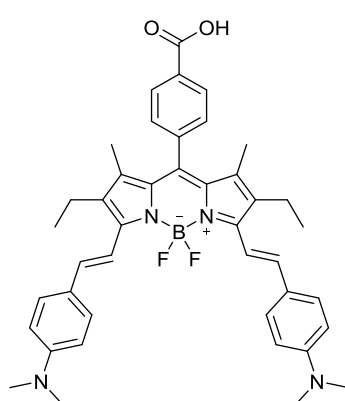
(13)



(14)



(16)



(18)

1.5 Summary of aims

The aims of this thesis are summarized below.

1. The synthesis and characterization of D- π -A and A- π -A BODIPY cores, and D- π -A styryl-extended BODIPYs with push-pull effects of differing magnitudes to determine how the push-pull effects modify the OL limiting properties.
2. A study of the NLO properties of 2,6-dibrominated BODIPY dyes and their non-brominated analogues to explore the effects of ESA in the triplet manifold to those in the singlet manifold. This work was recently published [91].
3. A study of the effect of the solvent on the NLO properties of selected BODIPYs.
4. The synthesis and characterization of amine-functionalized UCNPs and their conjugation to 2,6-diiodinated carboxylic acid functionalized BODIPY dyes to enable the use of NIR radiation in PDT related applications.
5. The determination of the photophysical and photochemical parameters of all synthesized compounds.
6. An analysis of trends in the properties of a selected series of synthesized BODIPYs by carrying out theoretical calculations in order to obtain a better understanding of the structure-property relationship of these compounds

Chapter 2: **Experimental**

Equipment, Materials, Synthesis and Methods

2 Experimental

2.1 Materials

Trifluoroacetic acid (TFA), triethylamine (TEA), boron trifluoride diethyl etherate ($\text{BF}_3 \cdot \text{Et}_2\text{O}$), N-iodosuccinimide (NIS), N-bromosuccinimide (NBS), benzene, Rhodamine 6G zinc phthalocyanine (Pc) and anhydrous potassium carbonate were purchased from Sigma Aldrich. 4-Methylesterbenzaldehyde, 4-(dimethylamino)benzaldehyde, hydroxybenzaldehyde, 4-formylbenzonitrile, 4-Nitrophthalonitrile, 2, 4-dimethylpyrrole and *p*-chloranil (tetrachloro-1,4-benzoquinone) were obtained from Aldrich. Piperidine was purchased from Riedel-de Haen AG. PE and Bengal Rose B were obtained from Fluka Chemika. Hydrochloric acid (HCl, 32 %), glacial acetic acid, sodium hydroxide (NaOH), acetonitrile (ACN), dichloromethane (DCM), ethyl acetate, petroleum ether (PE), dimethyl sulfoxide (DMSO), dimethylformamide (DMF), Tetrahydrofuran (THF) and hexane were obtained from local suppliers. The lanthanide salts, and various other salts that were used, were provided by Sigma Aldrich, who also provided tetraethylorthosilicate (TEOS), Igepal CO-520, 1-octadecene, oleic acid (OA), 3-aminopropyltriethoxysilane (APTES) and N,N'-dicyclohexylcarbodiimide (DCC), and 1-ethyl-3-(3-dimethylaminopropyl)carbodiimide (EDC).

2.2 Instrumentation

1. Ground state electronic absorption spectra were performed on a Shimadzu UV-2550 spectrophotometer.
2. Fluorescence excitation and emission spectra were recorded on a Varian Eclipse fluorescence spectrofluorimeter.

3. Elemental analyses for CHNS were carried out using a Vario-Elementar Microcube ELIII Series when the yields obtained provided sufficient compound for this procedure.
4. Mass spectral data were collected with a Bruker AutoFLEX III Smartbeam TOF/TOF Mass spectrometer. The instrument was operated in positive ion mode using an m/z range of 400–3000 amu. The voltage of the ion sources was set at 19 and 16.7 kV for ion sources 1 and 2 respectively, while the lens was set at 8.50 kV. The reflector 1 and 2 voltages were set at 21 and 9.7 kV respectively. The spectra were acquired using α -cyano-4-hydroxycinnamic acid as the MALDI matrix and a 354 nm nitrogen laser as the ionizing source.
5. Proton nuclear magnetic resonance spectra (^1H -NMR) were recorded in deuterated solvents (CDCl_3 or $\text{DMSO}-d_6$ or $\text{Acetone}-d_6$) using Bruker AMX600 MHz spectrometer.
6. FT-IR spectra were recorded on a Perkin Elmer Spectrum 100 FT-IR spectrometer.
7. Fluorescence lifetimes were measured using a FluoTime 300 EasyTau spectrometer (PicoQuant GmbH) using a time-correlated single photon counting (TCSPC) technique. BODIPYs **(1)**, **(2)**, **(3)**, **(4)**, **(5)**, **(6)** **(7)**, and **(9)** were excited at 485 nm using a LDH-*P*-C-485 laser head driven by PDL 800-B single channel driver (10 MHz repetition rate), while red-shifted BODIPYs **(10)**, **(11)**, **(12)**, **(13)**, **(14)**, **(16)**, and **(18)** were excited at 670 nm with a diode laser (LDH-*P*-670, 20 MHz repetition rate, 44 ps pulse width, PicoQuant GmbH). A monochromator with a spectral width of about 8 nm was used to select the required emission wavelength band. The response function of the system, which was measured with a scattering Ludox solution (DuPont), had a full width at half-maximum (FWHM) of about 300 ps. All

luminescence decay curves were measured at the maximum of the emission peak. The fluorescence lifetimes were obtained by deconvolution of the decay curves using the FluoFit Software program (PicoQuant GmbH, Germany).

8. Photo-irradiation for determination of singlet oxygen quantum yields (Φ_{Δ}) was carried out using a tunable laser system consisting of a Quanta-Ray Nd:YAG laser (532 nm, 400 mJ, 9 ns pulses at 10 Hz) pumping an Ekspla NT-342B-20-AW laser equipped with an optical parametric oscillator (OPO) system (0–7 mJ), with a wavelength range of 420–2300 nm. Solutions of sensitizer (absorbance of ca. 0.5 at the irradiation wavelength) containing DPBF were prepared in the dark and irradiated using the setup described above. Degradation of the DPBF peak was monitored. For red-shifted samples whose crossover with the standard occurred at wavelengths above 660 nm, the laser setup used for singlet oxygen determination was a Nd:YAG laser pumping a Lambda-Physik FL3002 dye laser (Pyridin 1 dye in methanol), with a pulse period of 7 ns and repetition rate of 10 Hz.
9. The thickness and morphologies of BODIPY-embedded thin films were determined by the knife edge attachment of a Bruker D8 Discover X-ray diffractometer.
10. All Z-scan experiments described in this study were performed using a frequency-doubled Nd:YAG laser (Quanta-Ray, 1.5 J /10 ns FWHM pulse duration) as the excitation source. The laser was operated in a near Gaussian transverse mode at 532 nm (second harmonic), with a pulse repetition rate of 10 Hz and energy range of 0.1 μ J – 0.1 mJ, limited by the energy detectors (Coherent J5-09). The low repetition rate of the laser prevents cumulative thermal nonlinearities. The beam was spatially filtered to remove the higher order modes and tightly focused with a 15 cm focal

length lens. No damage was detected between runs since the sample was moved or replaced (**Fig. 2.01**).

11. Transmission electron microscope (TEM) images were collected using a Zeiss Libra[®] transmission electron microscope.
12. Analyses of samples by XRD were carried out on a Bruker D8 Diffractometer fitted with a Lynx Eye detector under Cu K α ($\lambda=1.5405 \text{ \AA}$) with a scanning rate of 192 seconds per step. The samples were prepared on a zero background silicon wafer slide.
13. Energy dispersive spectroscopy (EDS) was carried out using an INCA PENTA FET coupled to a VAGA TESCAN using a 20 kV accelerating voltage.
14. The Gaussian 09 software package [92] running on an Intel/Linux cluster was used to perform all calculations. Geometry optimizations were carried out at the B3LYP level of theory with SDD basis sets. TD-DFT calculations employed the CAM-B3LYP level of theory with SDD basis sets. The Avogadro program [93] was used for all visualisations of molecular orbitals (MOs).
15. The calculations were performed at the Centre for High Performance Computing (CHPC).

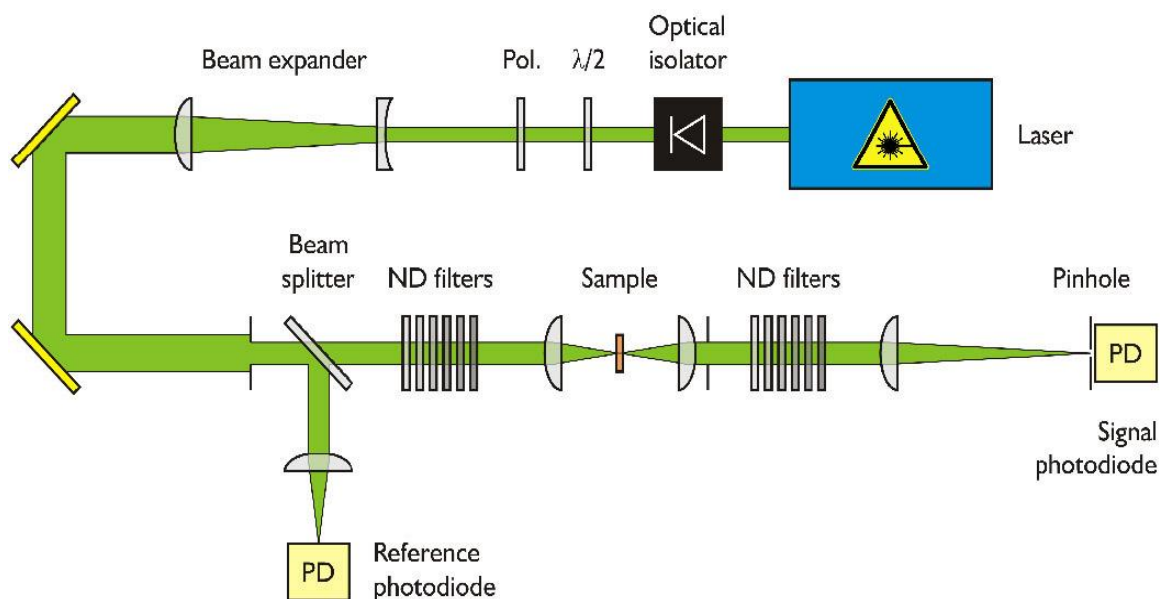


Figure 2.01 Schematic diagram of the laser setup for the z-scan measurements.

2.3 Photophysical and photochemical methods

2.3.1 Fluorescence quantum yield (Φ_F)

The fluorescence quantum yield is the ratio of photons absorbed to photons emitted by fluorescence. In other terms, the fluorescence quantum yield provides information about the probability of the excited state being deactivated by fluorescence as opposed to any other nonradiative process. The fluorescence quantum yield of the BODIPY dyes and their conjugates were obtained using the comparative method, using **Equation 17** [94]:

$$\Phi_F = \Phi_{Fstd} \frac{F \cdot A_{std} \cdot n^2}{F_{std} \cdot A \cdot n_{std}^2} \quad (19)$$

where F and F_{std} are the integrated fluorescence intensities of the BODIPY dye and the standard, respectively. The integrated fluorescence intensity is equal to the area beneath a fluorescence emission curve. A and A_{std} are the absorbance of the samples and standard respectively. ZnPc (Φ_F in DMSO = 0.20 [94, 95]; Φ_F in DMF = 0.28 [94]), and Rhodamine (Φ_F in EtOH = 0.95 [95, 96]) were used as standards. The standard and samples were both

excited at the same wavelength and the maximum absorbance of the solutions were kept below 0.05 to avoid any filter effects.

2.3.2 Fluorescence lifetime (τ_F)

When a molecule absorbs a photon of appropriate energy, a series of photophysical processes occur. These include but are not limited to; internal conversion or vibrational relaxation (loss of energy in the absence of light emission), fluorescence, ISC (from singlet state to a triplet state) and phosphorescence as shown in **Fig 1.09B**. Each process has a probability linked to it; this probability is characterized by constant (k). The constant (k) is inversely proportional to the rate of decay: $\tau = 1/k$. The mean length is called the lifetime. The lifetime of photophysical processes, vary significantly from tens of femtoseconds for internal conversion [97, 98] to nanoseconds for fluorescence and microseconds or seconds for phosphorescence [97].

Fluorescence lifetime is the average time a molecule spends in the S_1 singlet excited state before returning to the S_0 state via fluorescence. A time-correlated single photon counting (TCSPC) technique is used to calculate the fluorescence lifetime of a sample [99]. This is achieved by measuring the time-dependent fluorescence intensity profile of emitted light upon excitation by a pulsed laser [100, 101]. However, as the intensity of the light is very low, the probability of detecting one photon in a single period is consequently also very low [102]. Hence, periods in which more than one photon are observed are very rare. The time elapsed between excitation by the laser pulse and the detection of a fluorescence photon is measured and is referred to as the 'start-stop' time or the time delay. With many repetitions, a distribution of time differences may be acquired, with events being binned based on their respective time differences [98, 99]. Fitting an exponential curve to this distribution can be

used to calculate τ_F , the time it takes for the intensity to fall to 1/e of its initial value [100, 103].

2.3.3 Singlet oxygen quantum yield (Φ_Δ)

The singlet oxygen quantum yield (Φ_Δ) is typically described as the ratio of singlet oxygen molecules generated for every photon absorbed by a photosensitizer (**Equation. 20**). An indirect method with diphenylisobenzofuran (DPBF) as a chemical quencher was used by comparing the rates of degradations under the same conditions that are sensitized by the synthesized BODIPYs and by a standard [104, 105]. In an ideal situation, the absorption of a single photon has the capacity to generate only one molecule of singlet oxygen. Hence, the Φ_Δ of a photosensitizer, which can be determined using a relative method by comparison with a standard with a known Φ_Δ value [104-106].

$$\Phi_\Delta = \frac{\text{number of molecules of singlet oxygen formed}}{\text{number of photons absorbed}} \quad (20)$$

The singlet oxygen quantum yield (Φ_Δ) of BODIPY dyes was studied in a spectrophotometric cell of 1 cm path length [108, 109]. Solutions of the sample and reference sensitizers (absorbance below 0.5 at irradiation wavelength) containing DPBF were prepared in the dark and irradiated at the crossover wavelength used for laser excitation, the wavelength at which the absorbance of the sample and standard solutions are equal. The decay of the DPBF absorption peak was monitored spectroscopically with time of irradiation [110]. The values of Φ_Δ were calculated using **Equation 21** [110-114]:

$$\Phi_\Delta = \Phi_{\Delta\text{Std}} \cdot \frac{I_{\text{abs}}}{I_{\text{std}}} \quad (21)$$

where $\phi_{\Delta std}$ is the singlet oxygen quantum yield of the standard, and I_{abs} and I_{absstd} are the rates of light absorption by the sample and standard, respectively. The initial DPBF concentrations were kept the same for both the reference and the sample. Zinc Pc (ZnPc) (Φ_{Δ} in DMSO = 0.67 [112]; Φ_{Δ} in EtOH = 0.53 [115, 116]; Φ_{Δ} in DMF = 0.56 [117-119] and Rose Bengal (Φ_{Δ} in DMSO = 0.76 [117-120]; Φ_{Δ} in EtOH = 0.86 [113]) were used as standards for red-shifted BODIPY dyes and BODIPY core, respectively.

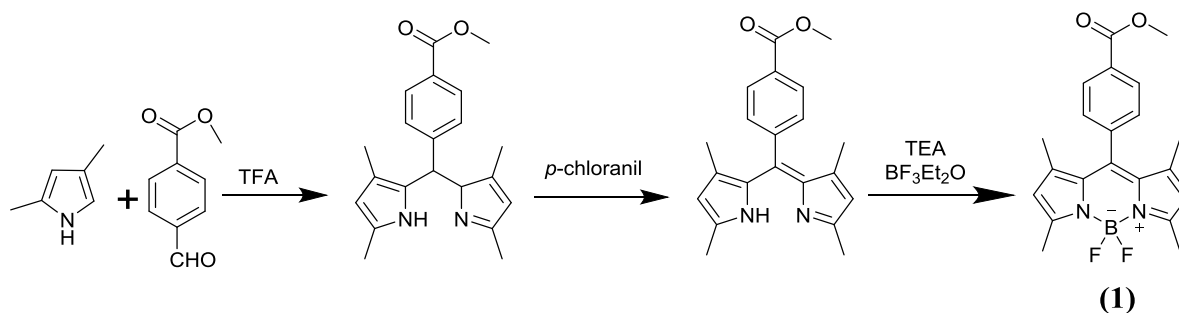
2.4 Synthesis and characterization of BODIPYs

Eighteen BODIPYs (**1-18**) were synthesized during the course of this study (**Schemes 1-18**). BODIPY core compounds (**1-9**) have been reported previously [11, 34-37, 121-123], while dyes (**10-18**) are novel. BODIPY core dyes have been used as precursors to prepare more complex 3,5-distyryl-substituted structures (**10**), (**11**), (**12**), (**13**), (**14**), (**16**), and (**18**) for use in the NLO studies described in Chapter 4. BODIPY cores (**1**), (**4**) and (**6**) were also used in the NLO studies, while (**5**) was conjugated to UCNPs in the work described in Chapter 5. BODIPYs (**15**) and (**17**) were only used as precursors to prepare final target compounds (**16**) and (**18**). Since the yields of the Knoevenagel condensation reactions involved were quite small, it was decided to only fully characterize BODIPYs (**16**) and (**18**).

2.4.1 4,4'-Difluoro-8-(4-methyl ester phenyl)-1,3,5,7-tetramethyl-4-bora-3a,4a-diaza-s-indacene (**1**)

The synthesis of the ester functionalized BODIPY was carried out in a single pot reaction. 2,4-Dimethylpyrrole (0.558 ml) and 4-methyl ester benzaldehyde (0.3 g) were added to dry DCM (30 ml). To this mixture, 3 drops of TFA were added, and the reaction was left to stir for 4 hours under Ar gas. Consumption of the 4-methyl ester benzaldehyde was monitored by thin layer chromatography (TLC) after which the temperature was lowered to 0°C, and *p*-

chloranil (0.539 g) was added. The solution was left to stir for 30 min. The temperature was lowered again to 0°C followed by the drop-wise addition of TEA (1.78 ml) and BF₃·Et₂O (2.52 ml). After overnight stirring, the resulting solution was washed with deionized water and extracted with DCM.

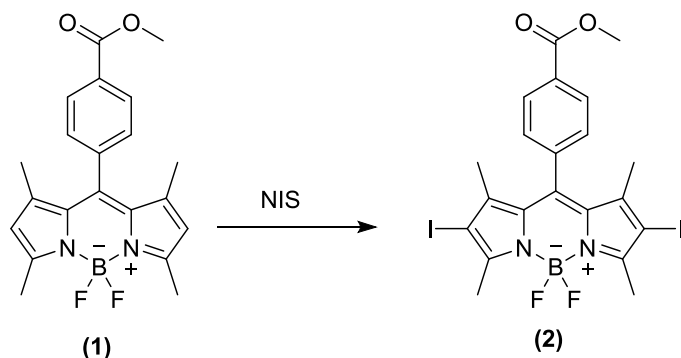


Scheme 2.01 The acid catalyzed synthesis of 4,4'-difluoro-8-(4-methyl ester phenyl)-1,3,5,7-tetramethyl-4-bora-3a,4a-diaza-*s*-indacene (**1**) via the classic “1-pot 3-step” method, highlighting the structural changes that occur at each step.

Product (**1**) separated by flash column chromatography with ethyl acetate/hexane (1:4) as the eluent to obtain 72% yield. UV-Vis (DCM): 503 nm, IR (cm⁻¹): 2957, 2945 (C-H), 1713 (C=O), 1278, 1186, 1066 (CN) ¹H NMR (600 MHz, CDCl₃) δ (ppm): 8.19 (d, 2H), 7.40 (d, 2H), 5.99 (s, 2H), 3.97 (s, 3H), 2.56 (s, 6H), 1.31 (s, 6H). Elemental Analysis for C₂₁H₂₁BF₂N₂O₂: Expected: C, 65.99; H, 5.54; N, 7.33; found: C 65.42, H 5.01, N 6.97

2.4.2 4,4'-Difluoro-8-(4-methyl ester phenyl)-1,3,5,7-tetramethyl-2,6-diiodo-4-bora-3a,4a-diaza-*s*-indacene (**2**)

200 mg of (**1**) and NIS (2.5 mole eq.) were dissolved in DCM (100 mL). The mixture was left to stir under Ar/N₂ at room temperature for 2 h. The reaction was quenched with water and the organic phase was dried and separated *via* column chromatography.

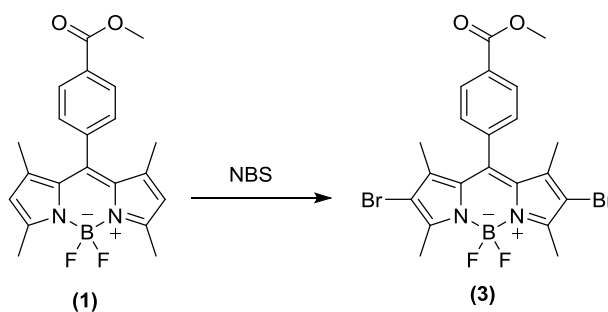


Scheme 2.02 Synthesis of 4,4'-difluoro-8-(4-methyl ester phenyl)-1,3,5,7-tetramethyl-2,6-diiodo-4-bora-3a,4a-diaza-s-indacene (**2**) via nucleophilic addition of iodine to BODIPY.

Product (**2**) was separated by flash chromatography using ethyl acetate/petroleum ether (1:4) as an eluent. Obtained: deep red crystalline powder at 86% yield. UV-Vis (DCM): 539 nm, IR (cm^{-1}): 2924, 2838 (C-H), 1715 (C=O), 1274, 1276, 1176, 991 (CN), 520 (C-I). ^1H NMR (600 MHz, CDCl_3) δ (ppm): 8.22 (d, 2H), 7.37 (d, 2H), 3.99 (s, 6H), 2.64 (s, 3H), 1.34 (s, 6H). MALDI-TOF (M+H): Calc. for $\text{C}_{21}\text{H}_{19}\text{BF}_2\text{I}_2\text{N}_2\text{O}_2$: Expected: 633.96 amu; found: 634.40 amu.

2.4.3 4,4'-Difluoro-8-(4-methyl ester phenyl)-1,3,5,7-tetramethyl-2,6-dibromo-4-bora-3a,4a-diaza-s-indacene (**3**)

260 mg of (**1**) and NBS (2.5 mole eq.) were dissolved in DCM (100 mL). The mixture was left to stir under Ar/N_2 at room temperature for 2 h. The reaction was quenched with water and the organic phase was dried and separated *via* column chromatography.



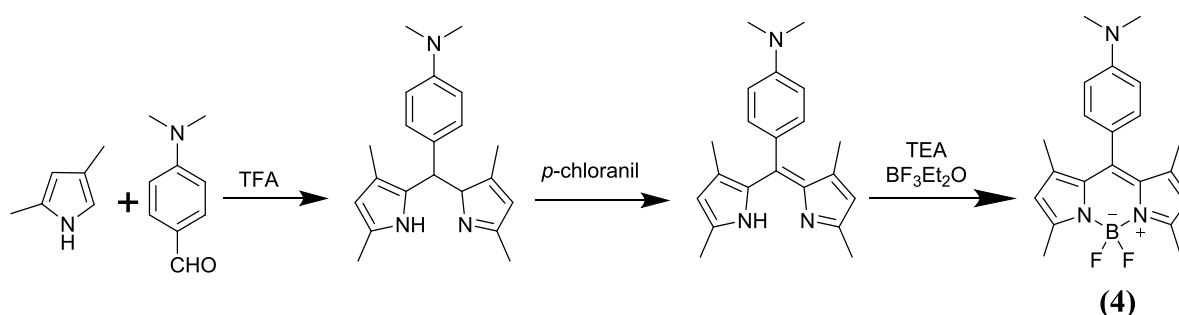
Scheme 2.03 Synthesis of 4,4'-difluoro-8-(4-methyl ester phenyl)-1,3,5,7-tetramethyl-2,6-dibromo-4-bora-3a,4a-diaza-*s*-indacene (**2**) via nucleophilic addition of bromine to BODIPY (**1**).

Product (**3**) was separated by flash chromatography using ethyl acetate/petroleum ether (1:4) as an eluent. Obtained: deep red crystalline powder at 70% yield. UV-Vis (DCM): 539 nm, IR (cm^{-1}): 2920, 2834 (C-H), 1716 (C=O), 1274, 1173, 1020 (CN), 550 (C-Br). ^1H NMR (600 MHz, CDCl_3) δ (ppm): 8.21 (s, 2H), 7.44 (s, 2H), 3.99 (s, 3H), 2.58 (s, 3H), 1.38 (s, 9H). MALDI-TOF (M+H): Calc. for $\text{C}_{21}\text{H}_{19}\text{BF}_2\text{Br}_2\text{N}_2\text{O}_2$: Expected: 539.99 amu; found: 539.31 amu.

2.4.4 4,4'-Difluoro-8-(4-dimethylamino phenyl)-1,3,5,7-tetramethyl-4-bora-3a,4a-diaza-*s*-indacene (**4**)

The synthesis of the dimethylamino-functionalized BODIPY was carried out in a single pot reaction. 2,4-Dimethylpyrrole (0.613 ml) and 4-dimethylaminobenzaldehyde (0.3 g) were added to dry DCM (30 ml). To this mixture, 3 drops of TFA were added, and the reaction was left to stir for 4 hours under Ar gas. Consumption of the 4-methyl ester benzaldehyde was monitored by TLC after which the temperature was lowered to 0°C , and *p*-chloranil (0.678 g) was added. The solution was left to stir for 30 min. The temperature was lowered again to 0°C followed by the drop-wise addition of TEA (1.96 ml) and $\text{BF}_3 \cdot \text{Et}_2\text{O}$ (2.278 ml).

After overnight stirring, the resulting solution was washed with deionized water and extracted with DCM.

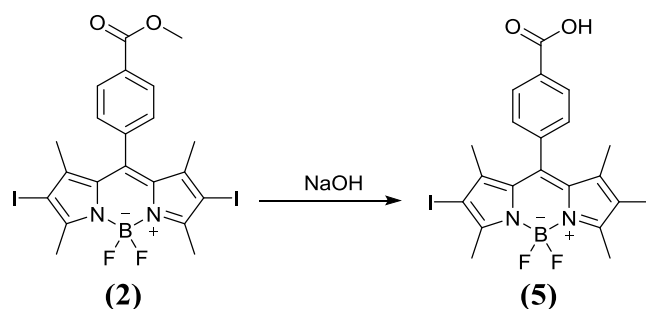


Scheme 2.04 The acid catalyzed synthesis of 4,4'-difluoro-8-(4-(dimethylaminophenyl))-1,3,5,7-tetramethyl-4-bora-3a,4a-diaza-s-indacene (**4**) via the classic “1-pot 3-step” method.

Product (**4**) was separated with flash chromatography using ethyl acetate/petroleum ether (1:4) as an eluent. Obtained: deep red crystalline powder at 48% yield. IR (cm^{-1}): 2920, 2849, 2808 (C-H), 1303, 1184, 1050 (C-N). ^1H NMR (600 MHz, CDCl_3) δ (ppm): 7.09 (d, 2H), 6.86 (d, 2H), 5.97 (s, 2H), 3.05 (s, 6H), 2.60 (s, 6H), 1.47 (s, 6H). Elemental Analysis for $\text{C}_{21}\text{H}_{24}\text{BF}_2\text{N}_3$: Expected: C, 68.68; H, 6.59; B, 11.44. Found C, 68.23, H, 6.37, N, 11.38.

2.4.5 4,4'-Difluoro-8-(4-carboxyphenyl)-1,3,5,7-tetramethyl-2,6-diiodo-4-bora-3a,4a-diaza-s-indacene (**5**)

To a solution of the BODIPY (**2**) (0.060 g, 0.068 mmol), in EtOH (2mL) and H_2O (1mL), was added NaOH (0.027 g, 0.68 mmol). The mixture was stirred at room temperature for 10 hours until complete consumption of the starting material was observed by TLC using ($\text{H}_2\text{O}/\text{EtOH}$, 1:4). The solution was then added HCl (10%) until neutral, then evaporated.



Scheme 2.05 Synthesis of 4,4'-difluoro-8-(4-carboxyphenyl)-1,3,5,7-tetramethyl-2,6-diiodo-4-bora-3a,4a-diaza-*s*-indacene (**5**) via hydrolysis of BODIPY (**1**).

Product (**5**) was separated by flash chromatography using ethyl acetate/petroleum ether (1:4) as an eluent. Obtained: dark red crystalline powder at 90% yield. IR (cm^{-1}): 3171 (OH), 2928, 2849, 2808 (C-H stretch), 1682 (C=O), 1300, 1170, (C-O), 1535 (O-H). ^1H NMR (600 MHz, DMSO) δ (ppm): 11.09 (s, 1H), 8.11 (d, 2H), 7.57 (d, 2H), 3.35 (s, 6H), 2.56 (s, 6H). MALDI-TOF (M+H): Calc. for $\text{C}_{20}\text{H}_{17}\text{BF}_2\text{I}_2\text{N}_2\text{O}_2$: Expected: 619.94 amu; found: 620.36 amu.

2.4.6 4,4'-Difluoro-8-(4-phenoxyphthalonitrile)-1,3,5,7-tetramethyl-2,6-4-bora-3a,4a-diaza-*s*-indacene (**6**)

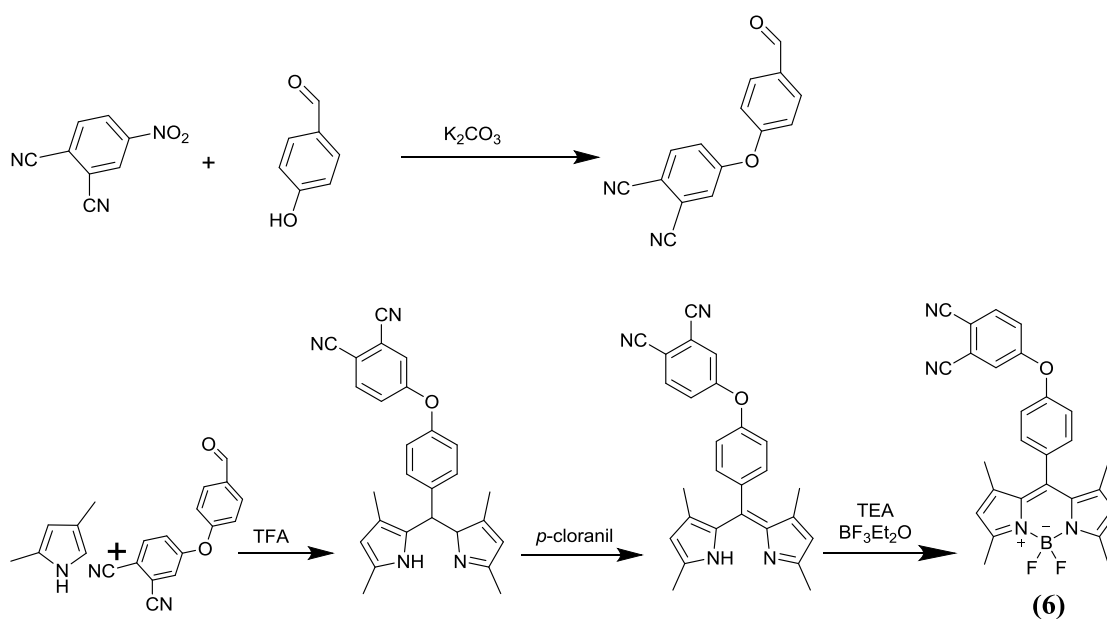
4-(4-Formylphenoxy)phthalonitrile and 4-(4-*meso*-BODIPY-phenoxy)phthalonitrile was synthesized as reported in [123] with minor modifications.

4-(4-Formylphenoxy)phthalonitrile

4-Nitrophthalonitrile (1.00 g, 5.78 mmol) and 4-hydroxybenzaldehyde (0.71 g, 5.78 mmol) were dissolved in DMF (15 mL) and degassed with argon in a dual-bank vacuum-gas manifold system. After stirring for 15 min, finely ground anhydrous potassium carbonate (2 g, 14.45 mmol) was added portion-wise within 2 h period with the efficient stirring. The progress of the reaction was monitored by TLC using DCM / hexane (3/1) solvent system.

The stirring of the suspension was maintained at room temperature for a further 24 h. The resulting mixture was poured into an iced-water/acetone mixture (5/1: v/v). The precipitate was collected by filtration, washed several times with ethanol, and dried in vacuum.

The synthesis of the phthalonitrile functionalized BODIPY was synthesized in a similar manner to that described in the literature [123] with minor modifications. 2,4-dimethylpyrrole (0.613 ml) and 4-(4-formylphenoxy)phthalonitrile (0.3 g) were added to dry DCM (30 ml). To this mixture, 3 drops of TFA were added, and the reaction was left to stir for 4 hours under Ar gas. Consumption of the 4-methyl ester benzaldehyde was monitored by TLC after which the temperature was lowered to 0°C, and *p*-chloranil (0.678 g) was added. The solution was left to stir for 30 min. The temperature was lowered again to 0°C followed by the drop-wise addition of TEA (1.96 ml) and BF₃·Et₂O (2.278 ml). After overnight stirring, the resulting solution was washed with deionized water and extracted with DCM.



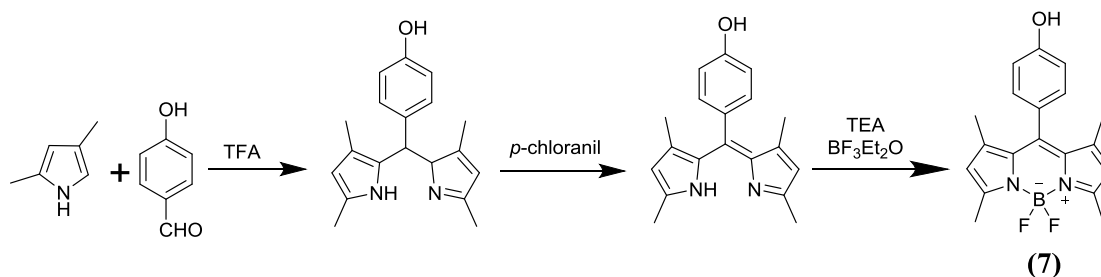
Scheme 2.06 The acid catalyzed synthesis of 4,4'-difluoro-8-(4-phenoxyphthalonitrile)-1,3,5,7-tetramethyl-2,6,4-bora-3a,4a-diaza-*s*-indacene (**6**) via the classic “1-pot 3-step” method, highlighting the structural changes that occur at each step.

The phthalonitrile product was separated by flash chromatography using ethyl acetate/petroleum ether (1:2) as an eluent. The desired pure compound was obtained as a yellowish powder in sufficient purity. Yield 90 %. IR (cm^{-1}): 3105-3041(C-H), 2805–2764 (O-C-H), 2237 ($\text{C}\equiv\text{N}$), 1691 (C=O), 1587–1506 (C=C), 1489–1309 (C-C), 1255 (Ar-O-Ar), 1209, 1155, 1111, 1087, 950, 858, 839, 821. $^1\text{H-NMR}$ (CDCl_3) δ (ppm): 10.03 (s, 1H, OCH), 8.01 (d, 2H, ArH), 7.81 (d, 1H, ArH), 7.41–7.34(m, 2H, ArH), 7.23 (d, 2H, ArH).

Product (6) was separated by flash chromatography using ethyl acetate/petroleum ether (1:4) as an eluent. Obtained: red crystalline powder at 74 % yield. IR (cm^{-1}): 3115–3038 (C-H), 2232 ($\text{C}\equiv\text{N}$), 1685 (C=N), 1590–1537 (C=C), 1250 (Ar-O-Ar). $^1\text{H-NMR}$ (CDCl_3) δ (ppm): 7.97 (s, 2H), 7.83 (d, 1H), 7.69 (d, 2H), 7.43–7.37 (m, 2H), 7.27–7.25 (m, 2H), 6.97 (d, 2H), 6.60 (d, 2H).

2.4.7 4,4'-Difluoro-8-(4-hydroxyphenyl)-1,3,5,7-tetramethyl-4-bora-3a,4a-diaza-s-indacene (7)

The synthesis of the hydroxyl functionalized BODIPY was carried out in a single pot reaction as reported [121] with minor modifications. 2,4-Dimethylpyrrole (0.750 ml) and 4-hydroxybenzaldehyde (0.3 g) were added to dry DCM (30 ml). To this mixture, 3 drops of TFA were added, and the reaction was left to stir for 4 hours under Ar gas. Consumption of the 4-hydroxybenzaldehyde was monitored by TLC after which the temperature was lowered to 0°C , and *p*-chloranil (0.720 g) was added. The solution was left to stir for 30 min. The temperature was lowered again to 0°C followed by the drop-wise addition of TEA (2.40 ml) and $\text{BF}_3\cdot\text{Et}_2\text{O}$ (3.40 ml). After overnight stirring, the resulting solution was washed with deionized water and extracted with DCM.

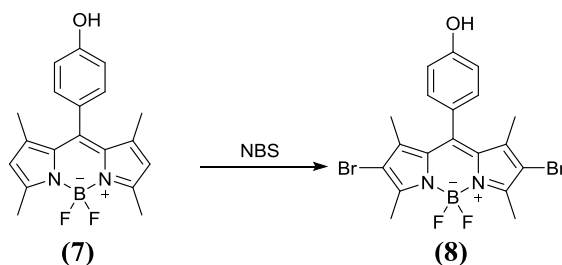


Scheme 2.07 The acid catalyzed synthesis of 4,4'-difluoro-8-(4-hydroxyphenyl)-1,3,5,7-tetramethyl-4-bora-3a,4a-diaza-*s*-indacene (**7**) via the classic “1-pot 3-step” method, highlighting the structural changes that occur at each step.

Product (**7**) was separated by flash chromatography using ethyl acetate/petroleum ether (1:4) as an eluent to obtain orange crystals at 65% yield. IR (cm^{-1}): 3106 (O-H stretch) 2918, 2849 (C-H stretch), 1521, 917 (O-H bend), 2863,3120,1135,1085 (C-O stretch). ^1H NMR (600 MHz, CDCl_3) δ (ppm): 7.15 (d, 2H), 6.98 (d, 2H), 6.00 (s, 2H), 5.37 (s, 1H), 2.57 (s, 6H), 1.46 (s, 6H).

2.4.8 4,4'-Difluoro-8-(4-hydroxyphenyl)-1,3,5,7-tetramethyl-2,6-dibromo-4-bora-3a,4a-diaza-*s*-indacene (**8**)

100 mg of (**7**) and NBS (2.5 mole eq.) were dissolved in DCM (100 mL). The mixture was left to stir under Ar/N_2 at room temperature for 2 h. The reaction was quenched with water, and the organic phase was dried and separated *via* column chromatography [122].

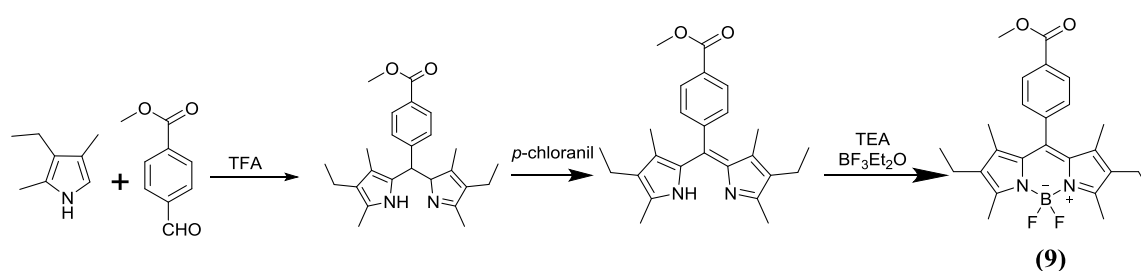


Scheme 2.08 Synthesis of 4,4'-difluoro-8-(4-hydroxy phenyl)-1,3,5,7-tetramethyl-2,6-dibromo-4-bora-3a,4a-diaza-*s*-indacene (**8**) via nucleophilic addition of bromine to BODIPY (**7**).

Product (**8**) was separated by flash chromatography using ethyl acetate/petroleum ether (1:4) as eluent, red crystals obtained at 83% yield. IR (cm^{-1}): 3106 (O-H) 2918, 2849 (C-H), 1521, 917 (O-H), 2863, 3120, 1135, 1085 (C-O), 520 (C-Br). ^1H NMR (600 MHz, CDCl_3) δ (ppm): 7.43 (d, 2H), 6.98 (d, 2H), 2.62 (s, 6H), 1.41 (s, 6H).

2.4.9 4'-difluoro-8-(4-methyl ester phenyl)-1,3,5,7-tetramethyl-2,6-diethyl-4-bora-3a,4a-diaza-s-indacene (**9**)

The synthesis of the ester-functionalized BODIPY was carried out in a single pot reaction. 2,3-Ethyl-2,4-dimethylpyrrole (0.750 ml) and 4-methyl ester benzaldehyde (0.3 g) were added to dry DCM (30 ml). To this mixture, 3 drops of TFA were added, and the reaction was left to stir for 4 hours under Ar gas. Consumption of the 4-methyl ester benzaldehyde was monitored by TLC after which the temperature was lowered to 0°C , and *p*-chloranil (0.720 g) was added. The solution was left to stir for 30 min. The temperature was lowered again to 0°C followed by the drop-wise addition of TEA (2.40 ml) and $\text{BF}_3 \cdot \text{Et}_2\text{O}$ (3.40 ml). After overnight stirring, the resulting solution was washed with deionized water and extracted with DCM.

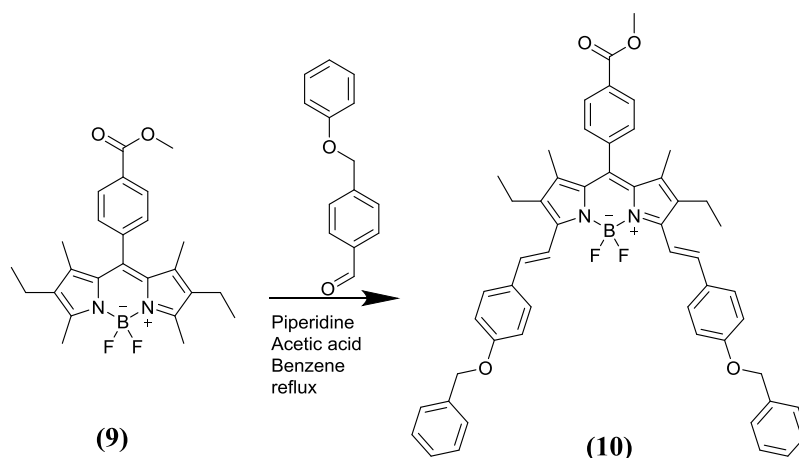


Scheme 2.09 The acid catalyzed synthesis of 4,4'-difluoro-8-(4-dimethylamino phenyl)-1,3,5,7-tetramethyl-4-bora-3a,4a-diaza-s-indacene (**9**) via the classic “1-pot 3-step” method.

Since compound **(9)** was used as a precursor for the preparation of target compounds **(10)** and **(18)** in this study, the final target compounds were the only ones to be fully characterized.

2.4.10 4,4'-Difluoro-8-(4-methyl ester phenyl)-1,7-dimethyl-2,6-diethyl-3,5,-di-styryl-(4'-benzyloxy)-4-bora-3a,4a-diaza-s-indacene (**10**)

(100 mg) of **(9)**, 4-(benzyloxy)benzaldehyde (0.535 mmol, 3 mole eq.) and glacial acetic acid (0.4 mL) were dissolved in dry benzene (20 mL) under Ar with stirring. Piperidine (0.4 mL) was added slowly, and the solution was heated to reflux for 2 h under Ar. A Dean-Stark trap was employed for the azeotropic removal of water formed during the condensation reaction. The reaction was quenched with water, and the organic phase was dried and separated using column chromatography with silica gel.



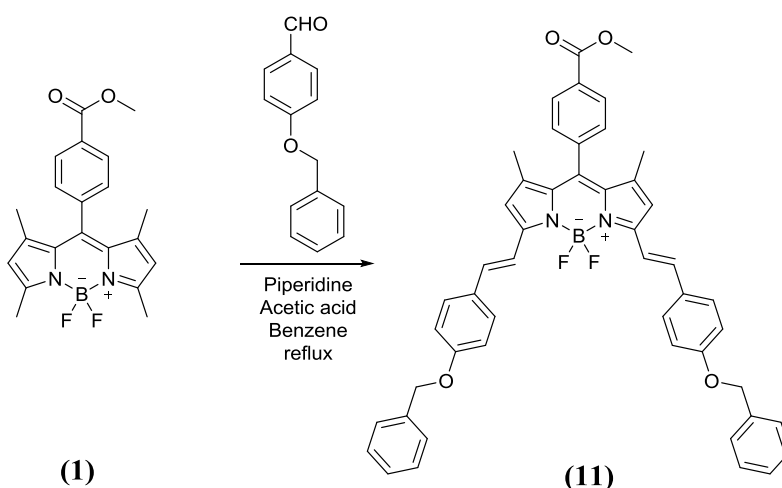
Scheme 2.10. Knoevenagel condensation of 4-(benzyloxy) benzaldehyde and **(9)** resulting in the synthesis of di-(4-benzyloxy)styryl BODIPY **(10)**.

(10) was separated by flash chromatography using ethyl acetate/petroleum ether (1:4) as an eluent. Obtained: dark blue crystalline powder at 30% yield. ^1H NMR (600 MHz, CDCl_3) δ (ppm): 8.12 (s, 2H), 7.60 (d, $J = 16.5$ Hz, 2H), 7.50 (s, 4H), 7.38 (s, 6H), 7.33 (s, 5H), 7.27 (s,

3H), 6.94 (s, 4H), 5.06 (s, 4H), 3.92 (s, 3H), 2.53 (s, 4H), 1.24 (s, 6H), 1.08 (s, 6H). MALDI-TOF (M+H): Calc. for Chemical Formula: C₅₃H₄₉BF₂N₂O₄: 826.38 amu, found: 826.99 amu.

2.4.11 4,4'-Difluoro-8-(4-methyl ester phenyl)-1,7-dimethyl-3,5,-di-styryl-(4'-benzyloxy)-4-bora-3a,4a-diaza-s-indacene (11)

100 mg of (1), 4-(benzyloxy)benzaldehyde (0.535 mmol, 3 mole eq.) and glacial acetic acid (0.4 mL) were dissolved in dry benzene (20 mL) under Ar with stirring. Piperidine (0.4 mL) was added slowly, and the solution was heated to reflux for 2 h under Ar. A Dean-Stark trap was employed for the azeotropic removal of water formed during the condensation reaction. The reaction was quenched with water, and the organic phase was dried and separated using column chromatography with silica gel.



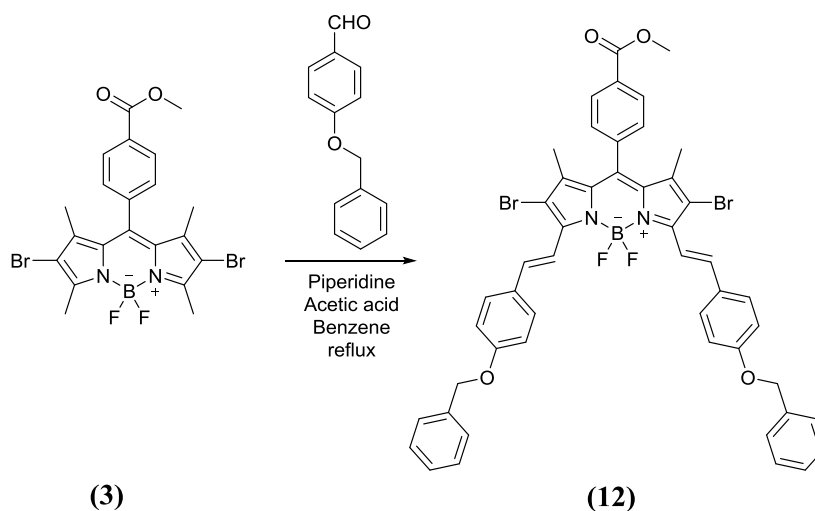
Scheme 2.11 Knoevenagel condensation of 4-(benzyloxy)benzaldehyde and (1) resulting in the synthesis of di-(4-benzyloxy)styryl BODIPY (11).

Product (11) was separated by flash chromatography using ethyl acetate/petroleum ether (1:4) as an eluent. Obtained: dark blue crystalline powder. ¹H NMR (600 MHz, CDCl₃) δ 8.22 (s, 2H), 7.63 (d, J = 16.6 Hz, 6H), 7.45 (d, J = 25.2 Hz, 10H), 7.38 (s, 2H), 7.24 (d, J = 16.2 Hz, 2H), 7.02 (s, 4H), 6.64 (s, 2H), 5.14 (s, 4H), 4.00 (s, 3H), 1.60 (s, 6H) ppm. ¹³C NMR (151 MHz, CDCl₃) δ 166.62, 159.65, 153.10, 141.43, 140.23, 136.66, 136.44, 136.07, 132.68,

130.67, 130.28, 129.74, 129.14, 129.02, 128.68, 128.15, 127.55, 117.77, 117.21, 115.08, 70.09, 31.23, 14.21 ppm. MALDI-TOF (M+H): Calc. for C₄₉H₄₁BF₂N₂O₄: 770.7 amu, found: 771.3 amu.

2.4.12 4,4'-Difluoro-8-(4-methyl ester phenyl)-1,7-dimethyl-2,6-dibromo-3,5,-di-styryl-(4'-benzyloxy)-4-bora-3a,4a-diaza-s-indacene (12)

100 mg of (3), 4-(benzyloxy)benzaldehyde (0.535 mmol, 3 mole eq.) and glacial acetic acid (0.4 mL) were dissolved in dry benzene (20 mL) under Ar with stirring. Piperidine (0.4 mL) was added slowly, and the solution was heated to reflux for 2 h under Ar. A Dean-Stark trap was employed for the azeotropic removal of water formed during the condensation reaction. The reaction was quenched with water, and the organic phase was dried and separated using column chromatography with silica gel.



Scheme 2.12 Knoevenagel condensation of 4-(benzyloxy)benzaldehyde and (3) resulting in the synthesis of di-(4-phenoxy)styryl BODIPY (12).

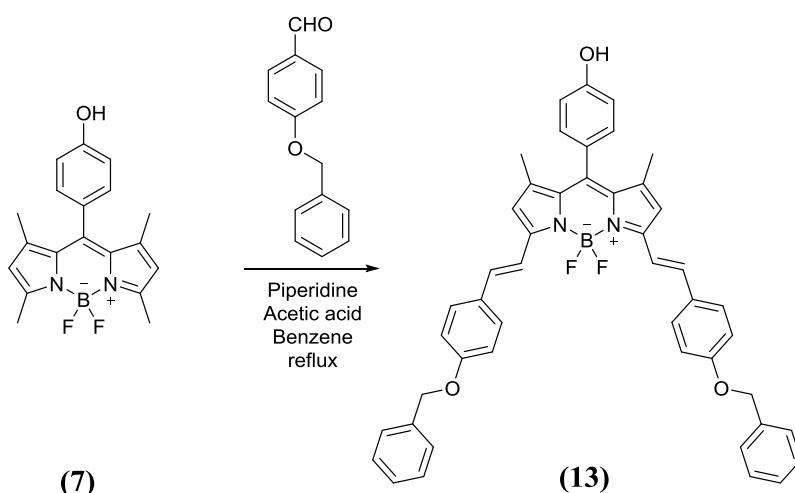
Product (12) was separated by flash chromatography using ethyl acetate/petroleum ether (1:4) as an eluent. Obtained: dark blue crystalline powder. ¹H NMR (600 MHz, CDCl₃) δ (ppm): 8.22 (s, 2H), 7.63 (d, *J* = 16.6 Hz, 6H), 7.45 (d, *J* = 25.2 Hz, 10H), 7.38 (s, 2H), 7.24

(d, $J = 16.2$ Hz, 2H), 7.02 (s, 4H), 6.64 (s, 2H), 5.14 (s, 4H), 4.00 (s, 3H), 1.60 (s, 6H).

MALDI-TOF (M+H): Calc. for $C_{49}H_{39}B_1Br_2F_2N_2O_3$: 928.1 amu, found: 929.1 amu.

2.4.13 4,4'-Difluoro-8-(4-hydroxyphenyl)-1,7-dimethyl-3,5-di-styryl-(4'-benzyloxy)-4-bora-3a,4a-diaza-s-indacene (13)

100 mg of (7), 4-(benzyloxy)benzaldehyde (0.535 mmol, 3 mole eq.) and glacial acetic acid (0.4 mL) were dissolved in dry benzene (20 mL) under Ar with stirring. Piperidine (0.4 mL) was added slowly, and the solution was heated to reflux for 2 h under Ar. A Dean-Stark trap was employed for the azeotropic removal of water formed during the condensation reaction. The reaction was quenched with water, and the organic phase was dried and separated using column chromatography with silica gel.



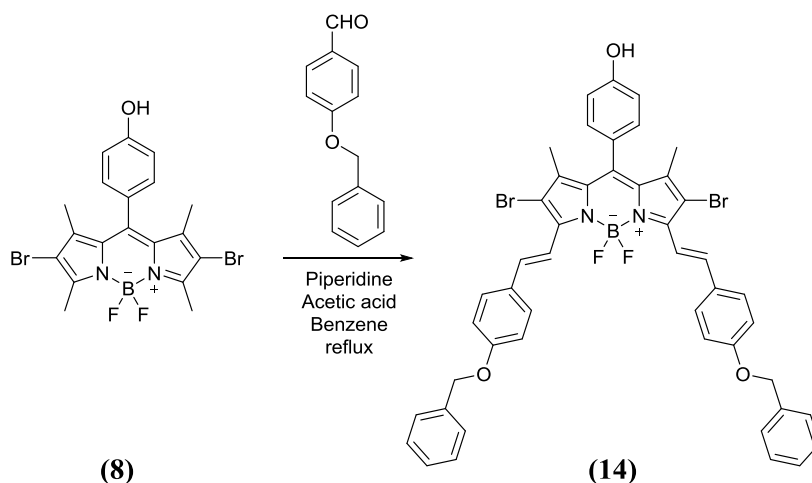
Scheme 2.13 Knoevenagel condensation of 4-(benzyloxy)benzaldehyde and (7) resulting in the synthesis of di-(4-phenoxy)styryl BODIPY (13).

Product (13) was separated by flash chromatography using ethyl acetate/petroleum ether (1:4) as an eluent. Obtained: dark blue crystalline powder. 1H NMR (600 MHz, $CDCl_3$) δ 7.58 (d, $J = 7.7$ Hz, 5H), 7.46 (s, 4H), 7.42 (s, 5H), 7.36 (s, 3H), 7.22 (s, 1H), 7.19 (s, 1H), 7.14 (s, 2H), 7.01 (s, 4H), 6.96 (s, 2H), 6.61 (s, 2H), 5.12 (s, 4H), 1.49 (s, 6H) ppm. ^{13}C NMR (151 MHz, $CDCl_3$) δ 159.51, 152.56, 141.88, 136.66, 135.65, 133.57, 129.90, 129.76, 129.07, 128.70,

128.14, 127.59, 117.37, 116.04, 115.15, 70.07, 29.65, 14.91 ppm. MALDI-TOF (M+H):
Calc. for C₄₇H₃₉BF₂N₂O₃: 728.6 amu, found: 729.3 amu.

2.4.14 4,4'-Difluoro-8-(4-hydroxyphenyl)-1,7-dimethyl-2,6-dibromo-3,5-di-styryl-(4'-benzyloxy)-4-bora-3a,4a-diaza-s-indacene (**14**)

100 mg of (**8**), 4-(benzyloxy)benzaldehyde (0.535 mmol, 3 mole eq.) and glacial acetic acid (0.4 mL) were dissolved in dry benzene (20 mL) under Ar with stirring. Piperidine (0.4 mL) was added slowly, and the solution was heated to reflux for 2 h under Ar. A Dean-Stark trap was employed for the azeotropic removal of water formed during the condensation reaction. The reaction was quenched with water, and the organic phase was dried and separated using column chromatography with silica gel.



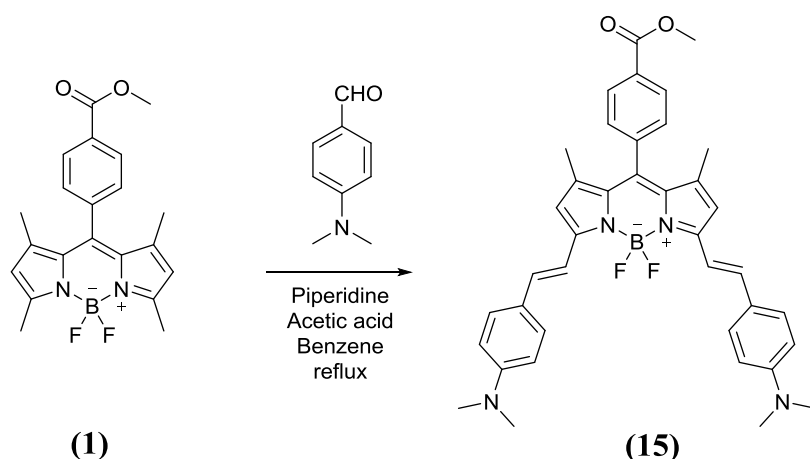
Scheme 2.14 Knoevenagel condensation of 4-(benzyloxy)benzaldehyde and (**8**) resulting in the synthesis of di-(4-benzyloxy)styryl BODIPY (**14**).

Product (**14**) was separated by flash chromatography using ethyl acetate/petroleum ether (1:4) as an eluent. Obtained: dark blue crystalline powder. ¹H NMR (600 MHz, CDCl₃) δ 8.15 (d, J = 16.6 Hz, 2H), 7.63 (t, J = 13.7 Hz, 6H), 7.48 (d, J = 7.2 Hz, 4H), 7.46 (s, 2H), 7.44 (t, J = 7.5 Hz, 5H), 7.38 (t, J = 7.1 Hz, 3H), 7.05 (d, J = 8.5 Hz, 4H), 5.15 (s, 4H), 1.54 (s, 6H) ppm. ¹³C NMR (151 MHz, CDCl₃) δ 160.06, 150.51, 148.85, 140.44, 139.29, 136.66, 134.26,

132.14, 132.05, 129.89, 129.44, 128.70, 128.18, 127.51, 116.15, 115.17 (m), 111.08, 70.22, 53.79, 33.52, 32.29, 29.74, 29.12, 24.65, 22.76, 14.48 ppm. MALDI-TOF (M+H): Calc. for $C_{47}H_{38}B_1Br_2F_2N_2O_3$: 887.4 amu, found: 888.1 amu.

2.4.15 4,4'-Difluoro-8-(4-methyl ester phenyl)-1,7-dimethyl-3,5,-di-styryl-(4'-dimethylamino)-4-bora-3a,4a-diaza-s-indacene (15)

100 mg of (1), 4-(dimethylamino)benzaldehyde (0.535 mmol, 3 mole eq.) and glacial acetic acid (0.4 mL) were dissolved in dry benzene (20 mL) under Ar with stirring. Piperidine (0.4 mL) was added slowly, and the solution was heated to reflux for 2 h under Ar. A Dean-Stark trap was employed for the azeotropic removal of water formed during the condensation reaction. The reaction was quenched with water, and the organic phase was dried and separated using column chromatography with silica gel.

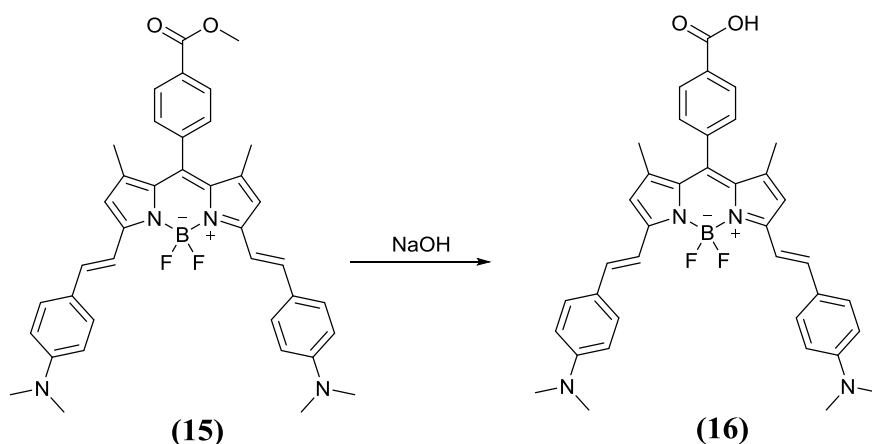


Scheme 2.15 Knoevenagel condensation of 4-(dimethylamino)benzaldehyde and (1) resulting in the synthesis of di-(4-dimethylamino)styryl BODIPY (15).

Product (15) was separated by flash chromatography using ethyl acetate/petroleum ether (1:4) as an eluent. Obtained: dark blue crystalline powder at 22 % yield. 1H NMR (600 MHz, $CDCl_3$) δ (ppm): 8.17 (s, 2H), 7.54 (s, 6H), 7.21 (s, 4H), 6.72 (s, 4H), 6.60 (s, 2H), 3.03 (s, 12H), 2.17 (s, 6H).

2.4.16 4,4'-Difluoro-8-(4-methyl ester phenyl)-1,7-dimethyl-3,5,-di-styryl-(4'-dimethylamino)-4-bora-3a,4a-diaza-s-indacene (16)

To a solution of the BODIPY (15) (0.060 g, 0.068 mmol), in EtOH (2mL) and H₂O (1mL), was added NaOH (0.027 g, 0.68 mmol). The mixture was stirred at room temperature for 10 hours until complete consumption of the starting material was observed by TLC (H₂O/EtOH, 1: 4). The solution was then added HCl (10%) until neutral, then evaporated.

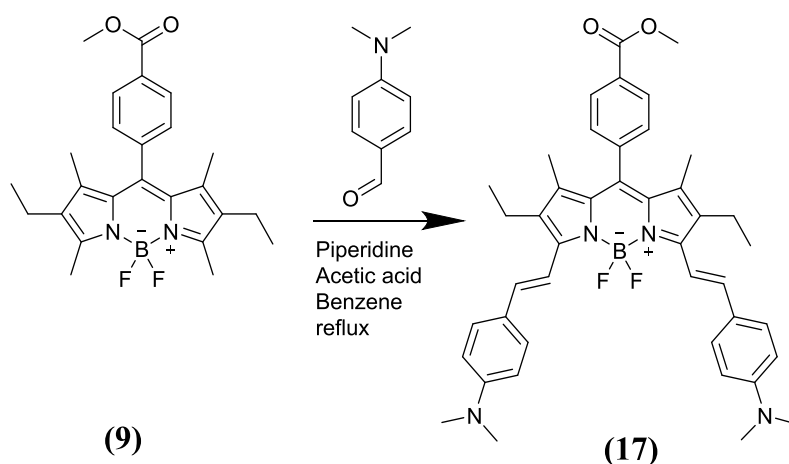


Scheme 2.16 Synthesis of 4,4'-difluoro-8-(4-carboxyphenyl)-1,3,5,7-tetramethyl-2,6-diiodo-4-bora-3a,4a-diaza-s-indacene (16) via hydrolysis of BODIPY (15).

Product (16) was separated by flash chromatography using ethyl acetate/petroleum ether (1:4) as an eluent. Obtained: dark blue crystalline powder at 90% yield. ¹H NMR (600 MHz, CDCl₃) δ (ppm): 8.17 (s, 2H), 7.54 (s, 6H), 7.21 (s, 4H), 6.72 (s, 4H), 6.60 (s, 2H), 3.03 (s, 12H), 2.17 (s, 6H). MALDI-TOF (M+H): Calc. for C₃₇H₃₅BF₂N₄O₂ Expected: 630.30 amu; found: 629.91 amu.

2.4.17 4,4'-Difluoro-8-(4-methyl ester phenyl)-1,7-dimethyl-2,6-diethyl-3,5, -di-styryl-(4'-dimethylamino)-4-bora-3a,4a-diaza-s-indacene (17)

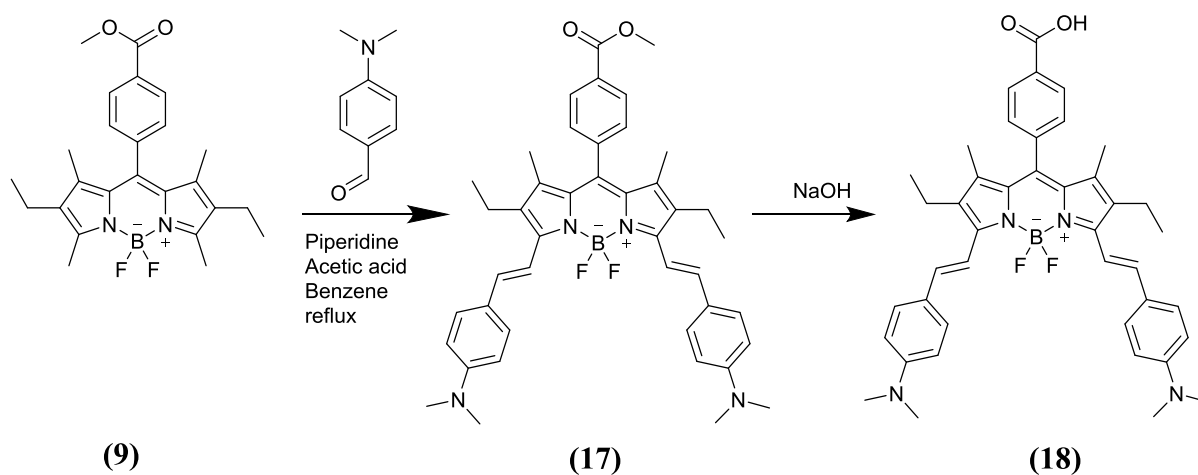
100 mg of (16), 4-(dimethylamino)benzaldehyde (0.535 mmol, 3 mole eq.) and glacial acetic acid (0.4 mL) were dissolved in dry benzene (20 mL) under Ar with stirring. Piperidine (0.4 mL) was added slowly, and the solution was heated to reflux for 2 h under Ar. A Dean-Stark trap was employed for the azeotropic removal of water formed during the condensation reaction. The reaction was quenched with water, and the organic phase was dried and separated using column chromatography with silica gel.



Scheme 2.17 Knoevenagel condensation of 4-(dimethylamino)benzaldehyde and (9) resulting in the synthesis of di-(4-dimethylamino)styryl BODIPY (17).

2.4.18 4,4'-Difluoro-8-(4-carboxyphenyl)-1,7-dimethyl-2,6-diethyl-3,5,-di-styryl-(4'-dimethylamino)-4-bora-3a,4a-diaza-s-indacene (18)

To a solution of the BODIPY (17) (0.060 g, 0.068 mmol), in EtOH (2mL) and H₂O(1mL), was added NaOH (0.027 g, 0.68 mmol). The mixture was stirred at room temperature for 10 hours until complete consumption of the starting material was observed by TLC (H₂O/EtOH, 1: 4). The solution was then added HCl (10%) until neutral, then evaporated.

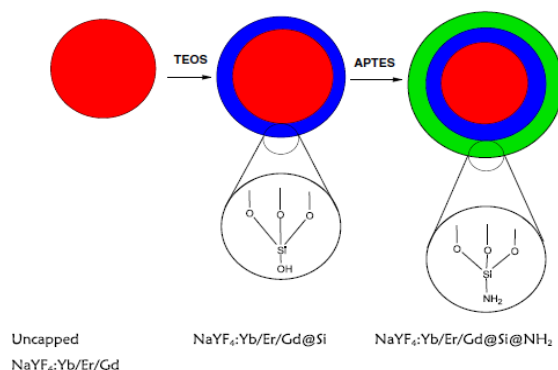


Scheme 2.18 Knoevenagel condensation of 4-(dimethylamino) benzaldehyde and (9) resulting in the synthesis of di-(4-dimethylamino)styryl BODIPY (17). Hydrolysis of BODIPY (17) to obtain BODIPY (18).

Product (17) was separated by flash chromatography using ethyl acetate/petroleum ether (1:4) as an eluent. Obtained: dark blue crystalline powder at 30% yield.

Product (18) was separated by flash chromatography using ethyl acetate/petroleum ether (1:4) as an eluent. Obtained: dark blue crystalline powder at 50% yield. ^1H NMR (600 MHz, DMF) δ (ppm): 8.27 (s, 2H), 7.68 (s, 4H), 7.60 (s, 4H), 7.39 (s, 2H), 6.93 (d, $J = 50.5$ Hz, 4H), 3.08 (s, 12H), 1.80 (s, 4H), 1.39 (s, 6H), 1.17 (s, 6H). MALDI-TOF ($M+H$): Calc. for Chemical Formula: $\text{C}_{42}\text{H}_{45}\text{BF}_2\text{N}_4\text{O}_2$: 686.36 amu, found: 687.04 amu.

2.5 Synthesis and characterization of UCNPs



Scheme 2.20. Schematic of UCNPs capping and functionalization.

2.5.1 Uncapped NaYF₄:Yb/Er/Gd

The UCNPs were synthesized using a method reported in the literature [60] with slight modifications as follows [60-65]: the lanthanide salts consisting of ErCl₃·(H₂O)₆ (0.0061 g, 0.016 mmol), YbCl₃·(H₂O)₆ (0.0558 g, 0.144 mmol), GdCl₃·(H₂O)₆ (0.0441 g, 0.1186 mmol) and Y(NO₂)₃·(H₂O)₆, (0.1992 and 0.595 mmol) were dispersed in 4 ml methanol and added to a mixture of OA (6 ml) and 1-octadecene (4 ml) in a 100 ml round bottomed flask. The mixture was heated to 160 °C while stirring for 30 min. The solution was allowed to cool down to room temperature. NH₄F (0.1185 g, 2.2 mmol) and NaOH (0.08 g, 2 mmol) were added to 10 ml of methanol and sonicated until fully dispersed. This mixture was then added to the solution above and stirred at room temperature for 30 min. A 70 °C heating step took place for 30 min, to remove excess solvent, and then the mixture was cooled to room temperature. The solution was flushed with argon for 30 min before the heating began. The solution was then heated to 300 °C for 90 min, with the temperature being monitored with an external thermocouple. After 90 min heating, the solution was cooled to room temperature and then washed with ethanol. The precipitate was collected by centrifuge for 20 min at 3000 rpm and then dried at 70 °C for 24 h. The resulting nanoparticles are termed uncapped NaYF₄: Yb/Er/Gd UCNPs.

2.5.2 Silica capped NaYF₄:Yb/Er/Gd@Si

The uncapped NaYF₄: Yb/Er/Gd UCNPs (70 mg) prepared above, were dispersed in cyclohexane (60 ml) in a round-bottomed flask. Igepal CO-520 (1 ml), which acts as a surfactant for the facilitation of the silicon oxide layer, was added. After 5 min, a second portion of Igepal CO-520 (4 ml) and 0.92 ml of 30 % ammonia were added to facilitate the capping of the nanoparticles with a silicon oxide layer. The solution was sonicated until a transparent emulsion was obtained. TEOS (400 μl) was added drop-wise, and then the reaction mixture was left to stir for 4 days. The silica-capped nanoparticles were then precipitated out with methanol, and then washed using a 1:1 EtOH and H₂O mixture. The nanoparticles were collected by centrifugation for 20 min at 3000 rpm and left to dry. The resulting nanoparticles are described as NaYF₄:Yb/Er/Gd@Si UCNPs, **Scheme 2.20**. The NaYF₄:Yb/Er/Gd@Si UCNPs were washed with anhydrous ethanol followed by toluene.

2.5.3 Amino capped NaYF₄:Yb/Er/Gd@Si@NH₂

The cleaned NaYF₄:Yb/Er/Gd@Si UCNPs (10 mg) were added to DMF (12 ml) and toluene (8 ml) in a 100 ml round bottomed flask and stirred for 10 min. APTES (1000 μl) was subsequently added drop-wise. The mixture was stirred for 24 h at room temperature under an argon atmosphere. The particles were washed with toluene, methanol and then collected by centrifuge. The resulting nanoparticles are described as NaYF₄:Yb/Er/Gd@Si@NH₂UCNPs,

2.5.4 Conjugation of amine-functionalized UCNPs and iodinated carboxylic acid BODIPY.

Carbodiimide compounds provide the most popular and versatile method for labeling or crosslinking to carboxylic acids. The most readily available and commonly used carbodiimides are the water-soluble EDC for aqueous crosslinking and the water-insoluble

DCC for non-aqueous organic synthesis methods. In this work, we used DCC because we are working with organic and inorganic species that are not soluble in water.

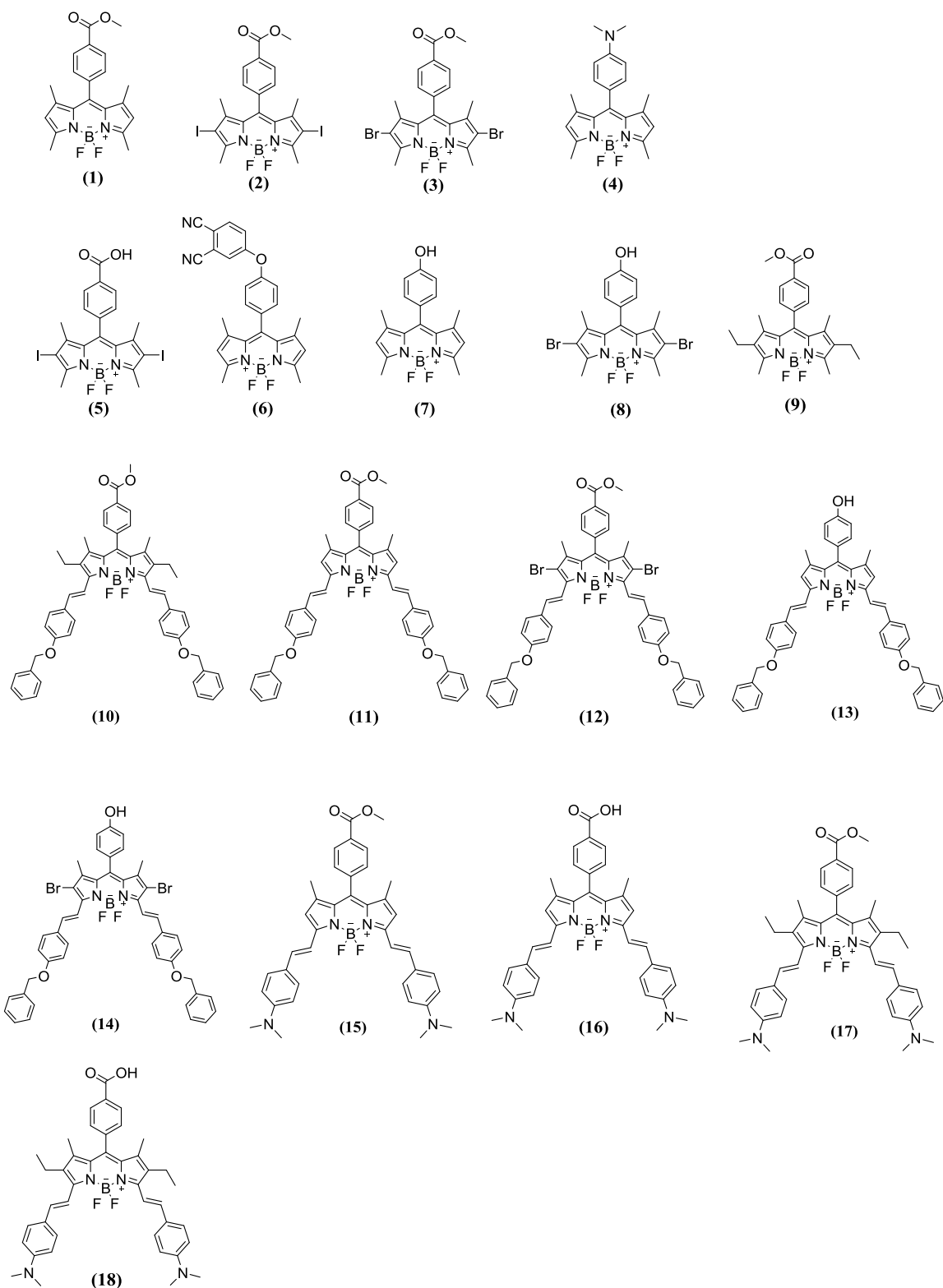
BODIPY (**5**) (0.1 g, 0.092 mmol) and 0.02 g (0.097 mmol) DCC was stirred in 4 mL DMF at room temperature for 48 h. NaYF₄:Yb/Er/Gd@Si@NH₂ (0.1 g) dissolved in 2 mL DMF was added drop-wise to the mixture, and stirring continued for a further 48 h [124-126]. The crude product was collected, and was then washed several times by centrifugation successively with acetone, MeOH and EtOH to remove DMF, unbound BODIPY (**5**), and excess DCC, respectively. The dry nanocomposite (NaYF₄:Yb/Er/Gd@Si@NH₂) was obtained by oven drying at 110 °C for 48 h. Yield: 0.13 g.

2.6 Preparation of thin films

Polystyrene (100 mg) and 0.1 mg of (**11**), (**12**), (**13**), and (**14**) were dissolved in DCM (1.5 mL) and sonicated until a homogeneous mixture of BODIPY–polymer solution was obtained. The obtained BODIPY–polystyrene solutions were dropped on glass substrates placed in a Petri dish, and the solvent was allowed to evaporate at room temperature. The average film thickness was determined to be ca. 23, 22, 24 and 24 μm for BODIPYs (**11**), (**12**), (**13**), and (**14**) in polystyrene respectively, using the knife edge attachment of a Bruker D8 Discover X-ray diffractometer.

**Chapter 3:
Synthesis and Spectroscopic
Characterization of BODIPY
Dyes**

3 Synthesis and characterization of BODIPY dyes



Scheme 3.01. The structures of all the eighteen BODIPY dyes synthesized in this thesis.

3.1 Synthesis, spectroscopic properties and characterization of the BODIPY dyes

This chapter presents the photophysical and photochemical properties of the compounds synthesized in this work and explores the synthesis of four BODIPY cores; some of their 2,6-dibrominated/iodinated analogues; and some 3,5-distyryl analogues with highly red-shifted spectral bands. The BODIPY cores were synthesized by using the classic “one-pot three-step” acid catalyzed condensation reaction, and were then used as precursors for BODIPY dyes with increasingly complex structures. The photophysical properties of these dyes were investigated in a number of different solvents, since significant changes have been observed when structural changes are made [11]. BODIPY core compounds such as **(1)**, **(8)**, and **(9)** are expected to be highly fluorescent, while BODIPY **(4)** has been reported to be fluorescent only under acid conditions due to the difference in the *meso*-aryl groups [37].

3.1.1 4,4'-Difluoro-8-(4-methyl ester phenyl)-1,3,5,7-tetramethyl-4-bora-3a,4a-diaza-s-indacene (**1**)

Although it has previously been reported [34, 35], BODIPY **(1)** was synthesized as a precursor for other dyes investigated in this study. BODIPY **(1)** was synthesized *via* the “one-pot three-step” TFA-catalyzed condensation of 2,4-dimethylpyrrole and 4-methyl ester benzaldehyde in DCM (**Scheme 2.01**). The methyl groups on the pyrrole served to sterically block the 2,4-position carbons, reducing unwanted polymerization of the pyrrole unit and hence improving the overall yield of the reaction. The characterization results were consistent with those reported in the literature [34, 35].

The electronic absorption spectrum for BODIPY **(1)** is typical of that of a *meso*-substituted BODIPY, with an absorbance maximum at 505 nm in benzene (**Fig. 3.02**) that similar to that

which has been previously reported [35, 127]. The emission spectrum is typical for a tetramethyl BODIPY (**Fig. 3.02**) [33]. **Table 3.01** summarizes the absorption, excitation and emission band wavelength maxima for BODIPY (**1**) in a number of different solvents. BODIPY (**1**) is highly soluble in a range of solvents, and did not show signs of aggregation. BODIPY (**1**) is extremely fluorescent due to its lack of ISC and its rigid π -system, which limits the rate of nonradiative decay [33]. The low rate of ISC also results in very low singlet oxygen quantum yields. Φ_{Δ} values were determined using the comparative method with Rose Bengal as the standard, using DPBF as a chemical trap for singlet oxygen. BODIPY (**1**) shows no measurable decrease in the main absorption band upon irradiation, indicating good photostability. Additionally, there is no measurable decrease of the main DPBF absorption, indicating the absence of significant singlet oxygen generation.

The $\log \epsilon$ value of 4.81 obtained for BODIPY (**1**) in benzene corresponds closely with the reported values of 4.80 (in DCM) and 4.81 (in THF) [34]. The fluorescence quantum yield (Φ_F) of 0.82 in benzene was comparable to the literature value of 0.93, recorded in DCM [34].

Table 3.01 Photophysical data BODIPY (**1**)

Solvent	Log ϵ	λ_{abs} [nm]	λ_{exc} [nm]	λ_{em} [nm]	τ_f [ns]	Φ_f	Φ_{Δ}
Benzene	4.81	505	505	519	2.78	0.82	---
ACN ^a	---	498	---	512	---	0.56	---
DCM ^a	4.80	501	---	510	---	0.94	---
THF ^a	4.81	501	---	509	---	0.93	---

^a Values reported in the literature [34, 35].

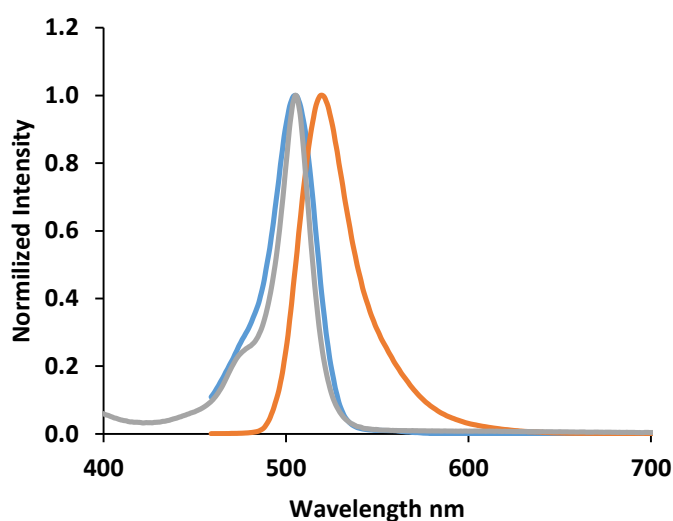


Figure 3.01 Normalized absorption (gray), excitation (blue) and emission (orange) spectra of BODIPY (**1**) in benzene.

3.1.2 4,4'-Difluoro-8-(4-methyl ester phenyl)-1,3,5,7-tetramethyl-2,6-diiodo-4-bora-3a,4a-diaza-s-indacene (**2**)

Halogenation of BODIPY dyes is relatively easy and must be carried out in an inert atmosphere. This structural modification drastically changes the photophysical properties of the BODIPY core in a manner that improves their utility for singlet oxygen applications. The increase in ISC is desirable for PDT. Of all the positions on the BODIPY core, the 2,6-positions are the most prone to nucleophilic halogenation (See reaction **Scheme 2.02.**) [21], the protons on the benzene ring are also prone to halogenation but, the first positions to be halogenated are the 2,6-positions [21]. As a result, BODIPY (**2**) has been reported in the literature by iodination of BODIPY (**1**) [34]. The characterization results were consistent with those reported in the literature [34].

The electronic absorption spectrum for BODIPY (**2**) is typical of a BODIPY dye, with the absorbance maximum occurring at 538 nm in benzene (**Fig. 3.04**): a red shift of ca. 33 nm with respect to its parent dye, BODIPY (**1**). Attachment of iodine atoms at the 2,6-positions

causes a destabilization of the HOMO with respect to the LUMO, resulting in a reduced HOMO–LUMO gap, and hence a red shift of the main spectral bands. **Table 3.02** summarizes the absorption, excitation, and emission wavelength maxima for BODIPY (**2**) in a number of different solvents. BODIPY (**2**) is highly soluble in a range of solvents. BODIPY (**2**) did not show signs of aggregation. The presence of iodine atoms at the 2,6-positions of BODIPY (**2**) increases the rate of ISC by relaxation of the spin-selection rule due to the heavy atom effect. This, in turn, increases the ability of the BODIPY dye to produce singlet oxygen. As expected, BODIPY (**2**) shows a significantly higher Φ_{Δ} value than BODIPY (**1**) (**Table 3.02**).

Table 3.02 Photophysical data BODIPY (**2**)

Solvent	Log ϵ	λ_{abs} [nm]	λ_{exc} [nm]	λ_{em} [nm]	τ_f [ns]	Φ_f	Φ_{Δ}
Benzene	4.82	538	538	557	0.20	0.02	0.86
ACN ^a	---	532	---	551	---	0.01	---
DCM ^a	4.82	534	---	546	---	0.04	---
THF ^a	4.77	532	---	546	---	0.05	---

^a Values reported in the literature [34, 35].

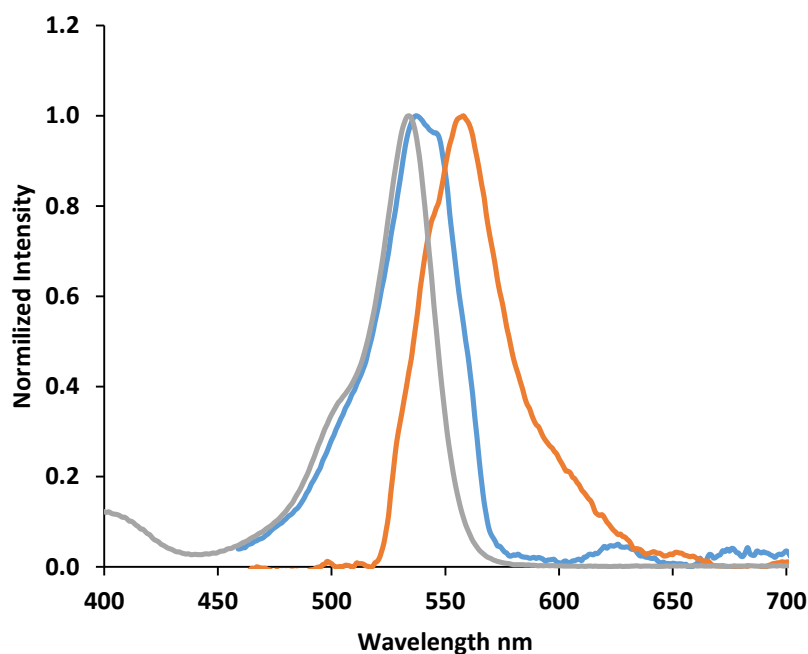


Figure 3.02 Normalized absorption (gray), excitation (blue) and emission (orange) spectra of BODIPY (**2**) in benzene.

3.1.3 4,4'-Difluoro-8-(4-methyl ester phenyl)-1,3,5,7-tetramethyl-2,6-dibromo-4-bora-3a,4a-diaza-s-indacene (3)

Scheme 2.03 shows the acid-catalyzed synthesis of BODIPY (3), which is similar to BODIPY (1). The characterization results were consistent with those reported in the literature [35].

The spectroscopic properties of BODIPY (3) are similar to those of BODIPY (2).

Table 3.03 Photophysical data BODIPY (3)

Solvent	Log ϵ	λ_{abs} [nm]	λ_{exc} [nm]	λ_{em} [nm]	τ_f [ns]	Φ_f	Φ_Δ
Benzene	4.86	531	531	557	0.97	0.03	0.84
ACN ^a	---	526	---	543	---	0.10	---

^a Values reported in the literature [35].

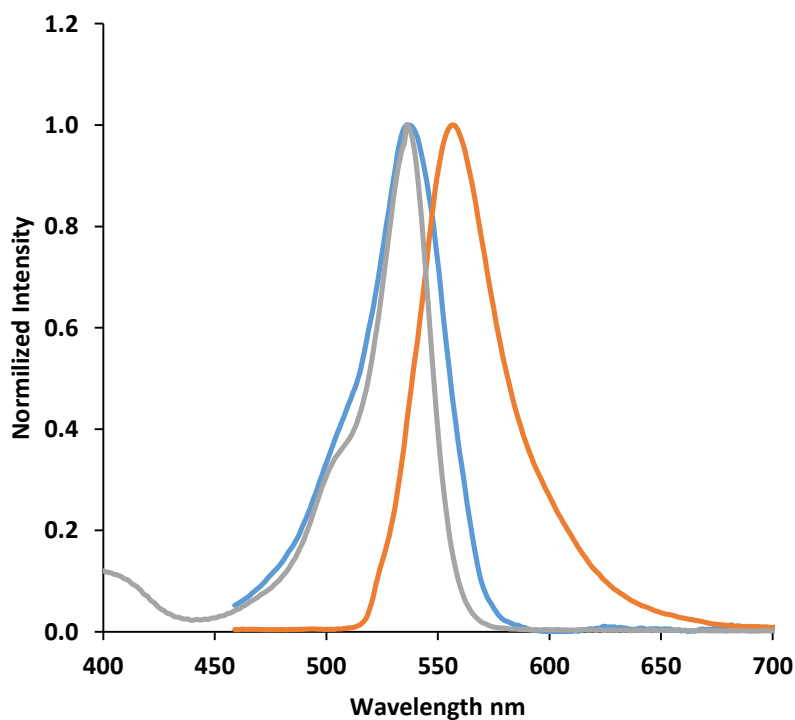


Figure 3.03 Normalized absorption (gray), excitation (blue) and emission (orange) spectra of BODIPY (3) in benzene.

3.1.4 4,4'-Difluoro-8-(4-dimethylamino phenyl)-1,3,5,7-tetramethyl-4-bora-3a,4a-diaza-s-indacene (4)

BODIPY (4) was synthesized using the acid catalyzed one-pot synthesis (Scheme 2.04), the same method as BODIPY (1). The characterization results were consistent with those reported in the literature [37].

Although the spectroscopic properties of BODIPY (4) are similar to those of BODIPY (1), there are, however, significant differences. The electronic absorption spectrum for BODIPY (4) is typical of that of a *meso*-substituted BODIPY, with an absorbance maximum at 503 nm in benzene (Fig. 3.08) and similar to that which has been previously reported [37]. The emission spectrum is typical for a tetra-methyl BODIPY (Fig. 3.08) [33]. Table 3.04 summarizes the absorption, excitation and emission band wavelength maxima for BODIPY (4) in a number of different solvents. BODIPY (4) is highly soluble in a range of solvents and did not show signs of aggregation. BODIPY (4) shows a lower fluorescence quantum yield due to changes in conformation and the intramolecular charge transfer (ICT) character of the S_1 state due to the presence of the electron-donating dimethylamino group on the *meso*-aryl ring [128-130]. Φ_Δ values were determined by using the comparative method with Rose Bengal as a standard. BODIPY (4) shows no measurable decrease in the main absorption band upon irradiation, indicating good photostability. Additionally, there was no measurable decrease of the main DPBF absorption, indicating a lack of significant singlet oxygen generation.

The log ϵ value of 4.82 obtained for BODIPY (4) in benzene is in the accepted range as other dyes of similar nature have been reported [34]. The fluorescence quantum yield (Φ_F) of 0.38 in benzene was comparable to the literature value of 0.44, recorded in n-hexane [130].

Table 3.04 Photophysical data BODIPY (4)

Solvent	Log ϵ	λ_{abs} [nm]	λ_{exc} [nm]	λ_{em} [nm]	τ_f [ns]	Φ_f	Φ_{Δ}
Benzene	482	503	503	515	4.53	0.38	---
Methanol ^a	---	496	---	510	---	0.003	---
n-Hexane ^a	---	500	---	511	---	0.44	---
ACN ^a	---	496	---	508	---	0.06	---

^a Values reported in the literature [130].

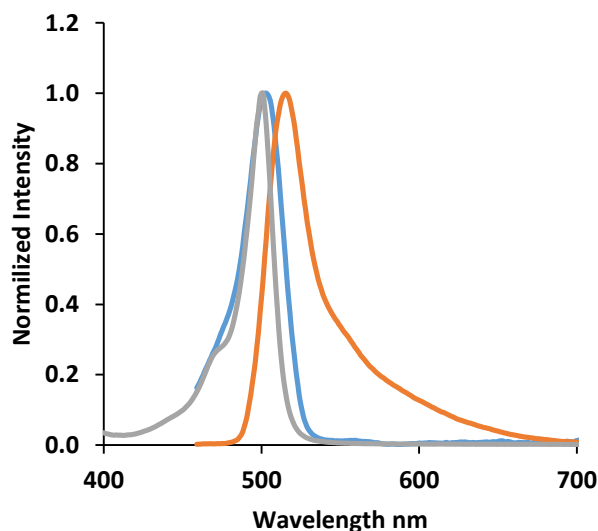


Figure 3.04 Normalized absorption (gray), excitation (blue) and emission (orange) spectra of BODIPY (4) in benzene.

3.1.5 4,4'-Difluoro-8-(4-carboxyphenyl)-1,3,5,7-tetramethyl-2,6-diiodo-4-bora-3a,4a-diaza-s-indacene (5)

BODIPY (5) was hydrolyzed under basic conditions to prevent the decomplexation of the BF_2 moiety, (Scheme 2.05). The characterization results were consistent with those reported in the literature [35].

The spectroscopic properties of BODIPY (5) are similar to those of BODIPY (2).

Table 3.05 Photophysical data BODIPY (5)

Solvent	Log ϵ	λ_{abs} [nm]	λ_{exc} [nm]	λ_{em} [nm]	τ_f [ns]	Φ_f	Φ_{Δ}
ACN ^a	4.87	531	---	548	0.77	0.02	---
DMSO	---	539	539	560	0.21	0.01	0.76

^a Values reported in the literature [35]

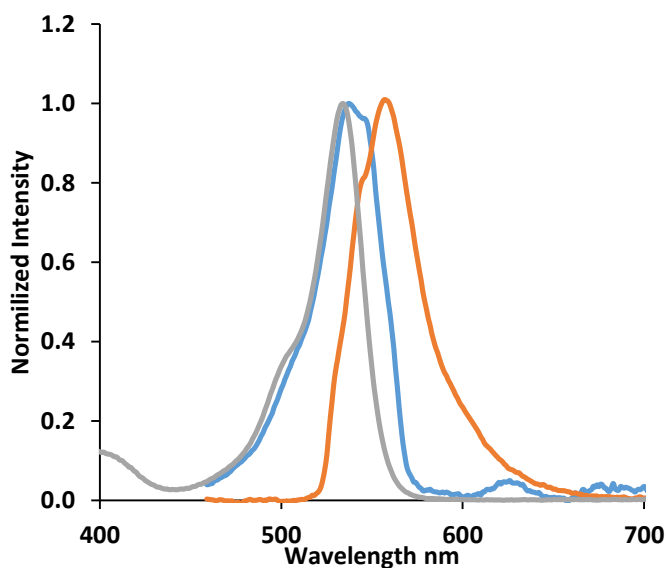


Figure 3.05 Normalized absorption (gray), excitation (blue) and emission (orange) spectra of BODIPY (**5**) in benzene.

3.1.6 4,4'-Difluoro-8-(4-phenoxyphthalonitrile)-1,3,5,7-tetramethyl-2,6,4-bora-3a,4a-diaza-s-indacene (**6**)

Before synthesis of BODIPY (**6**), an aldehyde was initially synthesized as seen in **Scheme 2.06**, thereafter the same method as BODIPY (**1**) was used to obtain BODIPY (**6**). The characterization results were consistent with those reported in the literature [94].

The spectroscopic properties of BODIPY (**6**) are similar to those of BODIPY (**1**).

Table 3.06 Photophysical data BODIPY (**6**)

Solvent	Log ϵ	λ_{abs} [nm]	λ_{exc} [nm]	λ_{em} [nm]	τ_f [ns]	Φ_f	Φ_{Δ}
Benzene	4.84	505	505	518	3.14	0.76	---
THF ^a	---	501	---	528	---	0.12	---
DMSO ^a	---	502	---	530	---	0.17	---
DCM ^a	---	503	---	523	---	0.27	---
CHCl ₃ ^a	---	505	---	524	---	0.37	---

^a Values reported in the literature [94].

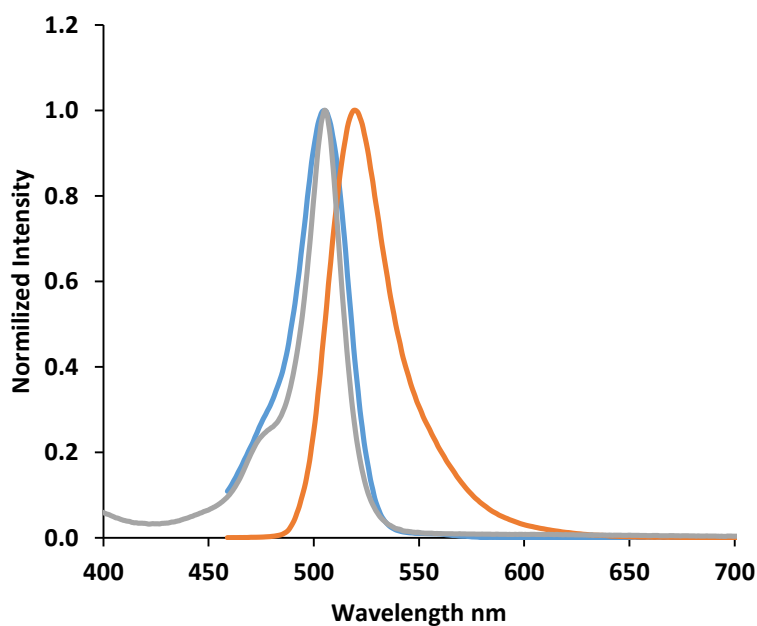


Figure 3.06 Normalized absorption (gray), excitation (blue) and emission (orange) spectra of BODIPY (**6**) in benzene.

3.1.7 4,4'-Difluoro-8-(4-hydroxyphenyl)-1,3,5,7-tetramethyl-4-bora-3a,4a-diaza-s-indacene (**7**)

The one pot acid catalyzed method was employed to obtain BODIPY (**7**) as seen **Scheme 2.07**. This method is the same as the one employed for BODIPY (**1**). The characterization results were consistent with those reported in the literature [121].

The spectroscopic properties of BODIPY (**7**) are similar to those of BODIPY (**1**).

Table 3.07 Photophysical data BODIPY (**7**)

Solvent	Log ϵ	λ_{abs} [nm]	λ_{exc} [nm]	λ_{em} [nm]	τ_f [ns]	Φ_f	Φ_{Δ}
Benzene	4.88	503	503	512	---	0.55	---
CHCl ₃ ^a	---	502	---	510	---	0.54	---
THF ^a	---	500	---	508	---	0.50	---

^a Values reported in the literature [121].

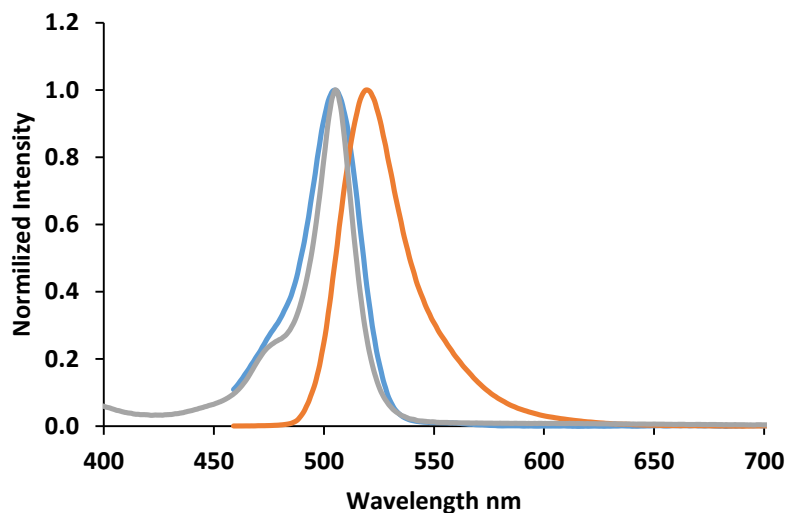
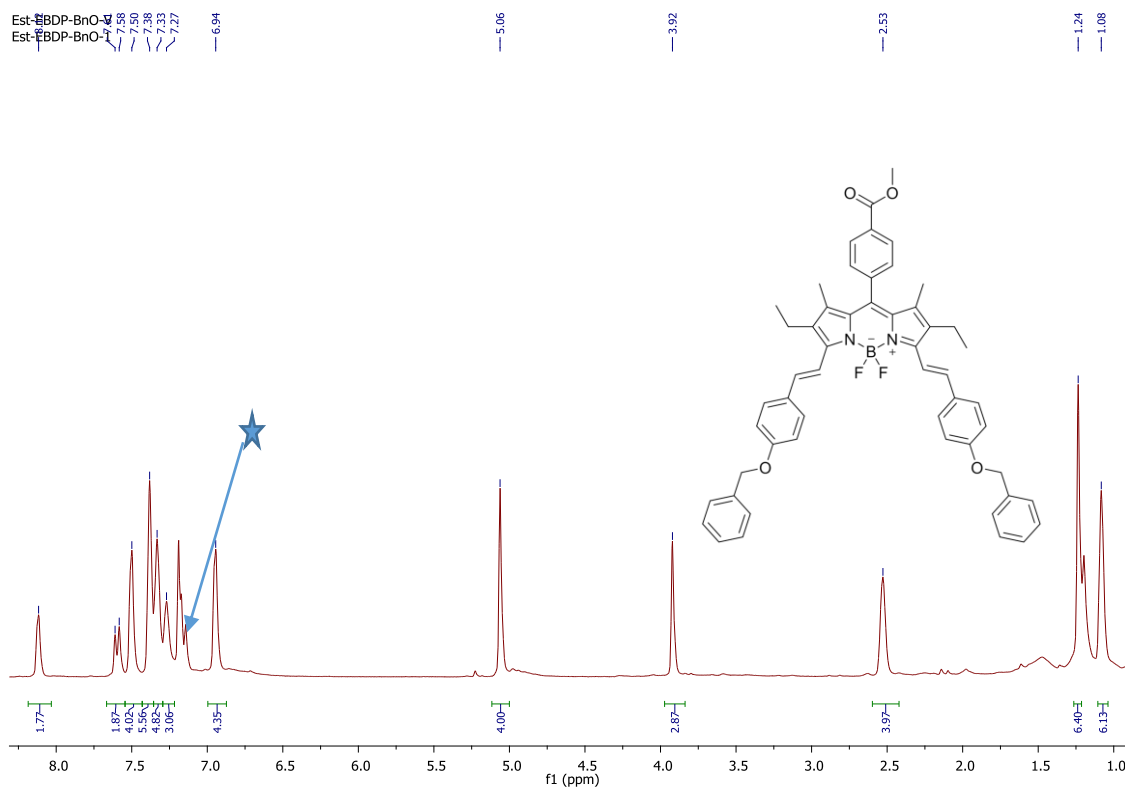


Figure 3.07 Normalized absorption (gray), excitation (blue) and emission (orange) spectra of BODIPY (7) in benzene.

3.1.8 4,4'-Difluoro-8-(4-methyl ester phenyl)-1,7-dimethyl-2,6-diethyl-3,5,-di-styryl-(4' benzyloxy)-4-bora-3a,4a-diaza-s-indacene (10)

BODIPY (10) was synthesized using a modified Knoevenagel condensation reaction [37, 41, 42] (Scheme 2.10). The condensation reaction is conducted in dry conditions. However, as water is formed as a by-product of the reaction, a Dean-Stark trap was used for the azeotropic removal of water [42].



★-Solvent peak

Figure 3.08 ^1H NMR spectrum of BODIPY (**10**) in CDCl_3 .

All forty-nine protons can be identified in the ^1H NMR spectrum of BODIPY (**10**) (**Fig. 3.08**). In the aromatic region, the peaks integrate to twenty-six protons, as would be expected for the phenyl ring and styryl double bond protons. The four proton peak at 5.06 ppm can be assigned to the $-\text{CH}_2$ benzyloxy protons and the three proton peak at 2.92 ppm was attributed to the ester group on the *meso*-aryl ring. Two singlets at 2.53 ppm and 1.08 ppm which integrate to four and six protons, respectively, can be assigned to the ethyl groups at the 2,6-positions. Lastly, the singlet at 1.24 ppm, which integrates to six protons, can be assigned to the methyl groups at the 1,7-positions of the BODIPY core. The predicted molecular mass of 826.38 amu for BODIPY (**10**) was confirmed by MALDI-TOF mass spectrometry, since the primary peak was observed at 826.99 am.

The absorbance maximum of BODIPY (**10**) lies at 667 nm in benzene (**Fig. 3.09**), and is red-shifted by ca. 138 nm when compared to its parent dye, BODIPY (**9**). BODIPY (**10**) shows a high fluorescence quantum yield due to the absence of heavy atoms. This suggests that in non-polar solvents such as benzene, the quantum yield value can be comparable to those of BODIPY cores and that in the absence of significant intramolecular charge transfer effects associated with the introduction of styryl groups at the 3,5-positions, the energy gap law does not result in large increases in the rate of nonradiative decay. Φ_{Δ} values were determined by using the comparative method. There was no measurable decrease of the main DPBF absorption, indicating an absence of significant singlet oxygen generation.

Table 3.08 Photophysical data BODIPY (**10**)

Solvent	Log ϵ	λ_{abs} [nm]	λ_{exc} [nm]	λ_{em} [nm]	τ_f [ns]	Φ_f	Φ_{Δ}
Benzene	4.74	664	665	682	3.87	0.72	---
DMSO	---	667	666	681	---	---	---

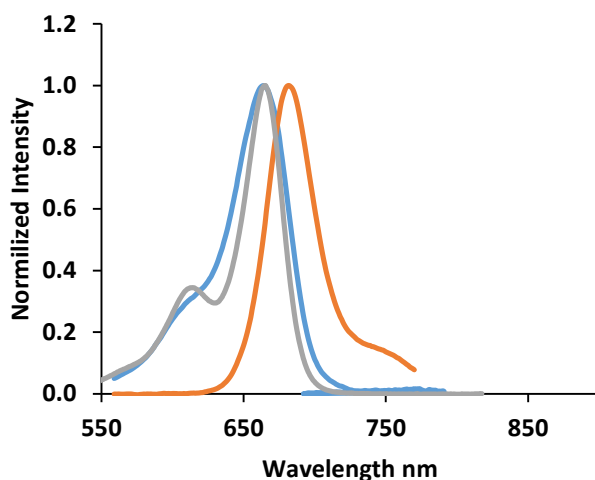


Figure 3.09 Normalized absorption (gray), excitation (blue) and emission (orange) spectra of BODIPY (**10**) in benzene.

3.1.9 4,4'-Difluoro-8-(4-methyl ester phenyl)-1,7-dimethyl-3,5,-di-styryl-(4'-benzyloxy)-4-bora-3a,4a-diaza-s-indacene (**11**)

BODIPY (**11**) was synthesized using the same method as BODIPY (**10**) as can be seen in **Scheme 2.11**. Completion of the reaction was confirmed by using TLC plates with ethyl

acetate/petroleum ether (1:4) as the eluent. The characterization of this dye, including both ^{13}C and ^1H NMR spectral data, has already been published as part of an OL study that is described in detail in Chapter 4 [91]. All thirty-eight protons were identified in the ^1H NMR spectrum. In the aromatic region, in the range of 8.5–6.5 ppm, the peaks integrate to the twenty-eight protons anticipated for the phenyl groups, the two styryl double bonds and the 2,6-position protons. The singlet at 6.64 ppm integrates to two protons and was assigned to the 2,6-position protons. Singlets at 5.14 and 4.00 ppm integrate to four and three protons respectively and were assigned to the $-\text{CH}_2$ benzyloxy protons and the ester group of the *meso*-aryl ring. Lastly, the singlet at 1.60 ppm which integrates to six was assigned to the two methyl groups at the 1,7-positions of the BODIPY core. The predicted molecular mass of 770.7 amu for BODIPY (**11**) was confirmed by MALDI-TOF mass spectrometry, since the primary peak was observed at 771.3 amu.

The electronic absorption spectrum for BODIPY (**11**) is typical of a BODIPY dye, with the absorbance maximum occurring at 649 nm in DMF (**Fig. 3.10**). The absorption maximum of BODIPY (**11**) is red-shifted by ca. 146 nm when compared to its parent dye, BODIPY (**1**). BODIPY (**11**) shows a high fluorescence quantum yield due to the absence of heavy atoms. Φ_{Δ} values were determined by using the comparative method with DPBF as the singlet oxygen scavengers. The values were found to be relatively low due to the low rate of ISC in the absence of heavy atoms at the 2,6-positions.

Table 3.09 Photophysical data BODIPY (**11**)

Solvent	Log ϵ	λ_{abs} [nm]	λ_{exc} [nm]	λ_{em} [nm]	τ_f [ns]	Φ_f	Φ_{Δ}
DMF	---	649	651	666	4.01	0.50	0.06
DMSO	4.60	653	651	672	3.72	0.49	0.06

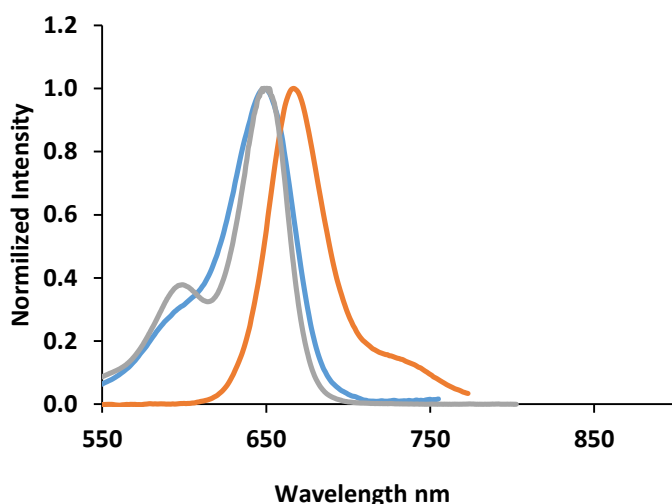


Figure 3.10 Normalized absorption (gray), excitation (blue) and emission (orange) spectra of BODIPY (**11**) in DMF.

3.1.10 4,4'-Difluoro-8-(4-methyl ester phenyl)-1,7-dimethyl-2,6-dibromo-3,5-di-styryl-(4'-benzyloxy)-4-bora-3a,4a-diaza-s-indacene (**12**)

BODIPY (**12**) was synthesized using the same method as BODIPY (**10**) as can be seen in **Scheme 2.12**. Completion of the reaction was confirmed by using TLC plates with ethyl acetate/petroleum ether (1:4) as the eluent. The characterization of this dye has already been published as part of an OL study that is described in detail in Chapter 4 [91]. All thirty-six protons were identified in the ^1H NMR spectrum of BODIPY (**12**). In the aromatic region, the peaks integrate to the anticipated twenty-six protons for the phenyl rings and the styryl double bonds. No peak analogous to the two proton singlet at 6.64 ppm in the spectrum of (**11**) was observed in the spectrum of (**12**) due to bromination at the 2,6-positions. Two singlets at 5.15 and 4.01 ppm integrate to four and three protons, respectively, and were assigned to the $-\text{CH}_2$ benzyloxy protons and the ester group of the *meso*-aryl ring. Lastly, the singlet at 1.60 ppm which integrates to six was assigned to the two methyl groups on the 1,7-positions of the BODIPY core. The predicted molecular mass of 928.1 amu for BODIPY (**12**) was confirmed by MALDI-TOF mass spectrometry, since the primary peak was observed at 929.1 amu.

The electronic absorption spectrum for BODIPY (**12**) is typical of a distyryl BODIPY dye, with the absorbance maximum occurring at 675 nm in DMF (**Fig. 3.11**). The absorption maximum of BODIPY (**12**) is red-shifted by ca. 142 nm when compared to its parent dye, BODIPY (**3**). BODIPY (**12**) shows a lower fluorescence quantum yield due to the presence of the bromine atoms at the 2,6-positions, which bring about the heavy atom effect and hence enhances spin-orbit coupling. The enhancement of spin-orbit coupling results in higher triplet state quantum yield. There is a higher population of molecules in the triplet state than the singlet state and hence a few to none fluoresce. Additionally, the high rate of ISC also results in moderately high Φ_{Δ} values (**Table 3.10**) when the rate at which the DPBF absorption intensity decreased was compared to that of a standard, ZnPc (Φ_{Δ} value in DMSO = 0.67 [112]). Notwithstanding, that higher Φ_{Δ} values have been reported for the BODIPY core dyes, the OL application envisaged for (**12**) does not require a high Φ_{Δ} value, since the interest is only to compare the effect of ESA in the singlet and triplet manifolds.

Table 3.10 Photophysical data BODIPY (**12**)

Solvent	Log ϵ	λ_{abs} [nm]	λ_{exc} [nm]	λ_{em} [nm]	τ_f [ns]	Φ_f	Φ_{Δ}
DMF	---	675	674	707	3.67	0.18	0.20
DMSO	5.06	677	674	707	3.42	0.14	0.26

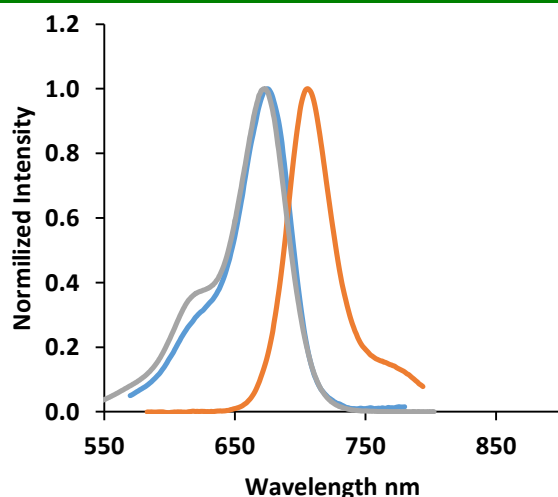


Figure 3.11 Normalized absorption (gray), excitation (blue) and emission (orange) spectra of BODIPY (**12**) in DMSO.

3.1.11 4,4'-Difluoro-8-(4-hydroxyphenyl)-1,7-dimethyl-3,5-di-styryl-(4'-benzyloxy)-4-bora-3a,4a-diaza-s-indacene (13)

BODIPY (13) was synthesized using the same method as BODIPY (10) as can be seen in **Scheme 2.13**. Completion of the reaction was confirmed by using TLC plate with ethyl acetate/petroleum ether (1:4) as the eluent. The characterization of this dye, including the ^{13}C and ^1H NMR spectral data, has already been published as part of an OL study that is described in detail in Chapter 4 [91]. All thirty-seven protons were identified in the ^1H NMR spectrum of BODIPY (13). In the aromatic region, the peaks associated with the phenyl rings, the styryl double bond and the 2,6-position protons are expected to integrate to twenty-nine protons, while the observed number of protons is thirty. The extra proton signal at 7.22 ppm was assigned to the hydroxy proton on the *meso*-aryl ring. A singlet at 6.61 ppm which integrates to two protons was attributed to the protons at the 2,6-positions of the BODIPY core. The singlet at 5.12 ppm, which integrates to four protons, was attributed to the four $-\text{CH}_2$ benzyloxy protons. Lastly, the singlet at 1.49 ppm which integrates to six protons was assigned to the two methyl groups on the 1,7-positions of the BODIPY core. The predicted molecular mass of 728.6 amu for BODIPY (13) was confirmed by MALDI-TOF mass spectrometry, since the primary peak was observed at 729.3 amu.

The spectroscopic properties of BODIPY (13) are similar to those of BODIPY (11), since the structures differ only in the nature of the para substituent on the *meso*-aryl ring.

Table 3.11 Photophysical data BODIPY (13)

Solvent	Log ϵ	λ_{abs} [nm]	λ_{exc} [nm]	λ_{em} [nm]	τ_f [ns]	Φ_f	Φ_{Δ}
DMF	---	642	645	659	3.85	0.56	0.07
DMSO	4.97	646	646	663	3.87	0.53	0.08

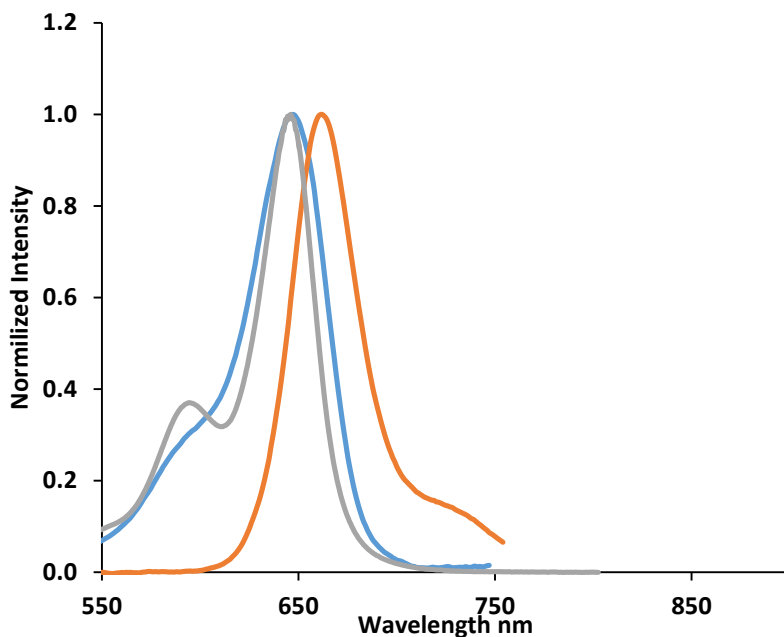


Figure 3.12 Normalized absorption (gray), excitation (blue) and emission (orange) spectra of BODIPY (**13**) in DMSO.

3.1.12 4,4'-Difluoro-8-(4-hydroxyphenyl)-1,7-dimethyl-2,6-dibromo-3,5,-di-styryl-(4' benzyloxy)-4-bora-3a,4a-diaza-s-indacene (**14**)

BODIPY (**14**) was synthesized using the same method as BODIPY (**10**) as can be seen in **Scheme 2.14**. Completion of the reaction was confirmed by using TLC plate with ethyl acetate/petroleum ether (1:4) as the eluent. The characterization of this dye, including the ^{13}C and ^1H NMR spectral data, has already been published as part of an OL study that is described in detail in Chapter 4 [91]. All thirty-five protons were identified in the ^1H NMR spectrum of BODIPY (**14**). In the aromatic region, the peaks integrate to twenty-seven protons, while the expected number of protons for the phenyl rings and styryl double bonds is twenty-six. The extra peak was assigned to the hydroxy proton on the *meso*-aryl ring. No peak analogous to the two proton singlet at 6.61 ppm in the spectrum of (**13**) was observed in the spectrum of (**14**), due to bromination at the 2,6-positions. The singlet at 5.15, which integrates to four protons, was attributed to the four $-\text{CH}_2$ benzyloxy protons. Lastly, the

singlet at 1.54 ppm which integrates to six protons was attributed to the two methyl groups on the 1,7-positions of the BODIPY core. The predicted molecular mass of 887.4 amu for BODIPY (**14**) was confirmed by MALDI-TOF mass spectrometry, since the primary peak was observed at 888.1. amu.

The spectroscopic properties of BODIPY (**14**) are broadly similar to those of BODIPY (**12**), since the structures differ only in the nature of the para substituent on the *meso*-aryl ring.

Table 3.12 Photophysical data BODIPY (**14**)

Solvent	Log ϵ	λ_{abs} [nm]	λ_{exc} [nm]	λ_{em} [nm]	τ_f [ns]	Φ_f	Φ_{Δ}
DMF	---	670	670	694	2.65	0.08	0.33
DMSO	5.10	671	671	698	2.34	0.07	0.38

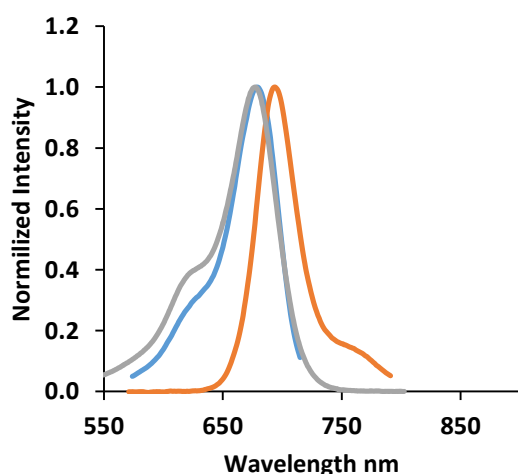


Figure 3.13 Normalized absorption (gray), excitation (blue) and emission (orange) spectra of BODIPY (**14**) in DMSO.

3.1.13 4,4'-Difluoro-8-(4-methyl ester phenyl)-1,7-dimethyl-3,5,-di-styryl-(4'-dimethylamino)-4-bora-3a,4a-diaza-s-indacene (**16**)

BODIPY (**15**) was synthesized using a modified Knoevenagel condensation reaction [37, 41, 42] (**Scheme 2.10**) and it was further hydrolyzed to form (**16**) using a base (NaOH) to avoid the decomplexation of the BF₂ moiety in acidic conditions. Thirty-six protons were readily identified in the ¹H NMR spectrum of BODIPY (**16**). In the aromatic region, in the range of

8.3–6.5 ppm, there are a number of peaks that integrate to eighteen protons, as would be expected for the three phenyl rings, the two styryl double bonds and the two protons at the 2,6-positions. The two proton doublet at 6.60 ppm can be readily assigned to the latter. The singlet at 3.03 ppm, which integrates to twelve, was attributed to the four methyl groups of dimethylaminostyryl. Lastly, the singlet at 2.17 which integrates to six was attributed to the two methyl groups on the 1,7-positions of the BODIPY core. Although the peak for the carboxylic acid proton could not be identified, possibly due to overlap with a residual solvent peak or exchange with deuterium from the CDCl₃, the predicted molecular mass of 630.30 amu for BODIPY (**10**) was confirmed by MALDI-TOF mass spectrometry, since the primary peak was observed at 629.91 amu.

The electronic absorption spectrum for BODIPY (**16**) is typical of a BODIPY dye, with the absorbance maximum occurring at 716 nm in benzene (**Fig. 3.14**). The absorption maximum of BODIPY (**16**) is red-shifted by ca. 211 nm when compared to its parent dye, BODIPY (**1**). BODIPY (**16**) has a low fluorescence quantum yield value (**Table 3.13**) due to changes in conformation and the ICT character of the S₁ state due to the electron-donating dimethylamino group at the 3,5 positions [128-130]. When Φ_{Δ} values were determined using the comparative method and ZnPc as the standard (Φ_{Δ} value in DMSO = 0.67 [112]), no measurable decrease was observed in the main absorption band upon irradiation, indicating good photostability. There was also no measurable decrease of the main DPBF absorption band indicating a lack of significant singlet oxygen generation.

Table 3.13 Photophysical data BODIPY (**16**)

Solvent	Log ϵ	λ_{abs} [nm]	λ_{exc} [nm]	λ_{em} [nm]	τ_f [ns]	Φ_f	Φ_{Δ}
Benzene	4.91	716	716	738	2.46	0.15	---
DMSO	---	732	732	806	---	---	---
ACN	---	704	704	784	---	---	---

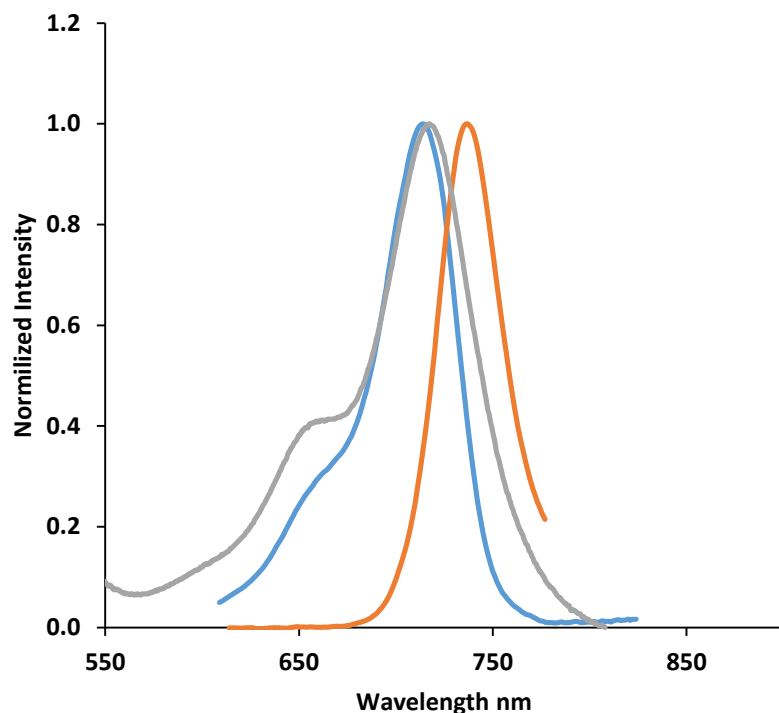


Figure 3.14 Normalized absorption (gray), excitation (blue) and emission (orange) spectra of BODIPY (**16**) in benzene.

3.1.14 4,4'-Difluoro-8-(4-carboxyphenyl)-1,7-dimethyl-2,6-diethyl-3,5-di-styryl-(4'-dimethylamino)-4-bora-3a,4a-diaza-s-indacene (**18**)

BODIPY (**18**) was synthesized using the same method as BODIPY (**10**) as can be seen in **Scheme 2.18**. Completion of the reaction was confirmed by using TLC plates with ethyl acetate/petroleum ether (1:4) as the eluent. All forty-nine protons can be identified in the ^1H NMR spectrum of BODIPY (**18**). In the aromatic region, the peaks integrate to sixteen protons as would be expected for the three phenyl rings and two styryl double bonds. No peak analogous to the two proton singlets at ca. 6.60 ppm in the spectra of (**11**) and (**13**) was observed in the spectrum of (**18**) due to the ethyl groups at the 2,6-positions. Singlets at 5.85 and 3.08 ppm integrate to one and twelve protons, respectively, and can be assigned to the phenyl carboxylic acid proton and the dimethylamino protons. Two singlets at 1.80 ppm and 1.17 ppm which integrate to four and six protons respectively, can be attributed to the ethyl groups at the 2,6-positions of the BODIPY dye. Lastly, the singlet at 1.39 ppm which

integrates to six protons can be assigned to the methyl groups at the 1,7-positions of the BODIPY core. The predicted molecular mass of 686.36 amu for BODIPY (**18**) was confirmed by MALDI-TOF mass spectrometry, since the primary peak was observed at 687.04 amu.

The spectroscopic properties of BODIPY (**18**) are broadly similar to those of BODIPY (**16**).

Table 3.14 Photophysical data BODIPY (**18**)

Solvent	Log ϵ	λ_{abs} [nm]	λ_{exc} [nm]	λ_{em} [nm]	τ_f [ns]	Φ_f	Φ_{Δ}
Benzene	4.91	717	717	753	2.65	0.11	---
DMSO	---	738	738	807	---	---	---

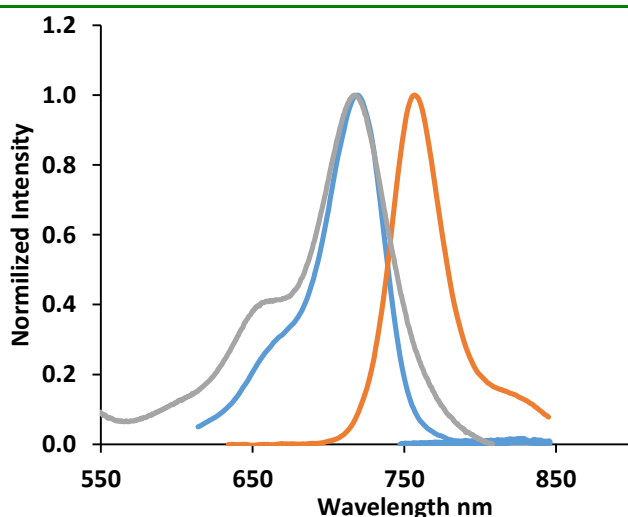


Figure 3.15 Normalized absorption (gray), excitation (blue) and emission (orange) spectra of BODIPY (**18**) in benzene.

3.2 Concluding remarks

Four BODIPY cores, (**1**), (**4**), (**6**), and (**7**) were synthesized and characterized using $^1\text{H-NMR}$, CHNS elemental analysis and FT-IR. Additionally, the melting point for BODIPY (**6**) corresponds to the one reported in the literature [123]. All the BODIPY cores were synthesized using the classic “one-pot-three-step” acid catalyzed condensation reaction. BODIPYs (**1**), (**6**), and (**7**) show high similar fluorescence quantum yields despite the differences in their structures. However, BODIPY (**4**) shows relatively low fluorescence

quantum yields compared to the other cores. This can be attributed to electron-donating nature of the dimethylamino phenyl group at the *meso*-position, since this enhances ICT in the S₁ state which ultimately results in the low fluorescence quantum yield [128-130]. All the BODIPY cores show good photostability. Changing the solvent had very little effect on the main spectral bands of these BODIPY dyes, except for BODIPY (**4**) which shows significant differences in different solvents due to ICT [128-130].

The addition of styryl groups to the BODIPY core to form 3,5-distyryl BODIPYs causes a decrease in fluorescence quantum yield in polar solvents as well as a decrease in singlet oxygen quantum yield, which was expected as the inclusion of styryl groups introduces greater scope for intramolecular charge transfer effects and hence enhanced rates of nonradiative decay. This provides another reason why the conjugation of a brominated or iodinated BODIPY core is preferred in the context of UCNP conjugation in addition to the good spectral overlap between the upconversion nanoparticles for a good FRET.

The main spectral bands of BODIPYs (**12**) and (**14**) were red-shifted to lie well within the therapeutic window, at 671 and 677 nm respectively, and had a Φ_{Δ} value of 0.26 and 0.38 in DMSO. Both BODIPYs (**12**) and (**14**) could be potentially useful as photosensitizers in PDT.

BODIPYs (**2**), (**3**) and (**5**) displayed large singlet oxygen quantum yields that equalled that of the standard, Rose Bengal. Additionally, these BODIPYs exhibited superior photostability than the standard in ethanol, suggesting that they might be useful standards for Φ_{Δ} measurements. BODIPY (**5**) was selected for conjugation to amine functionalized UCNPs and the results are described in Chapter 5. BODIPYs (**3**), (**16**), and (**18**) have low fluorescence quantum yields despite not having heavy atoms. This is because of ICT that quenches the fluorescence [128-130]. This property is noteworthy as far as non-linear optical applications are concerned, and this will be discussed in detail in Chapters 4 and 6.

**Chapter 4:
NLO parameters of BODIPY
dyes in solution and
embedded in polymer thin
films**

4 NLO parameters of BODIPY dyes in solution and in polymer thin films

4.1 BODIPYs for NLO studies

As has been described in the introduction, there has been a limited amount of work carried out on the utility of BODIPYs in the field of NLO. Given their structures, BODIPYs are expected to exhibit an OL response, since it has been demonstrated that π -conjugated systems possess large electronic polarizabilities [128, 129]. An important feature in the design of BODIPY dyes for NLO applications is its dipole moment. In this work, we show that BODIPY dyes with a higher dipole moment are better optical limiters as far as the nonlinear absorption coefficient (β), the second order hyperpolarizability (γ) and imaginary third-order susceptibility ($\text{Im}[\chi^{(3)}]$), values are concerned [128-132]. Molecules with donor (D) and acceptor (A) moieties that are separated by a π -conjugation system (D- π -A) BODIPY cores are also known to exhibit large β values than those who possess (A- π -A) configuration, this is because of a large dipole moment in the molecule. In this study, the effect of having D- π -A and A- π -A substitution patterns on the BODIPY core is compared, along with the effect on the OL properties of modifying the electron donating properties of styryl groups at the 3,5-positions and adding ethyl groups at the 2,6-positions of π -extended BODIPYs with D- π -A structures [132-137]. In addition, we also look at the effect of introducing heavy atoms in the 2,6-positions of the BODIPY dyes [91], and explore solvent dependence in the main OL parameters and the effect of increasing the input energy.

4.2 NLO parameters

NLO parameters were determined using the open aperture z-scan setup described in Chapter 2 (Fig 2.01). Studies were carried out in solution as well as in solid-state. Solution studies were conducted in DMSO, DCM and benzene, to investigate the effects of different solvents

on the OL properties of the BODIPYs studied, and solid state studies were conducted on polystyrene thin films. The parameters reported in this work are the nonlinear absorption coefficient (β), the second order hyperpolarizability (γ) and imaginary third-order susceptibility ($\text{Im}[\chi^{(3)}]$), absorption coefficient (α), and the OL threshold (I_{lim}). Although the determination of how effective an optical limiter cannot be characterized by a single parameter, the γ values are particularly useful because, they incorporate concentration changes and can hence be used for meaningful comparisons of different samples [77].

The nonlinear absorption coefficient, β , is one of the important parameters in certifying the suitability of materials for OL. On the nanosecond timescale, the β value typically depends on the population of molecules in the first excited state of the singlet and triplet manifolds. It provides a measure of the degree of NLA. On a femtosecond timescale, this parameter depends only on a simultaneous 2PA process. Since there is more than one process that can result in nonlinear absorption on the nanosecond timescale, it is referred to as the β_{eff} value in the context of this study. In molecules where the linear absorption at the laser wavelength of 532 nm is zero, all absorption at that wavelength must be due ultimately to 2PA [78]. However, when there are non-zero α values, this may also be due to sequential ground state absorbance and ESA (as opposed to concerted 2PA) [127]. The BODIPYs studied with the exception of BODIPY (4) have a small amount of linear absorbance occurring at 532 nm, so the observed OL properties are due to a combination of mechanisms.

The z-scan plots for BODIPYs (4) and (10), (11), (12), (13), (14), (16), and (18) in solution are shown in **Fig. 4.01**. The concentration and incident laser pulse intensity were kept constant to negate any variation that may result because of change in concentration or change in beam intensity. In other words, this ensures that the variation in the results is largely due to the structural differences. The z-scan plots show a typical nonlinear absorption behavior, with

RSA profiles. The imaginary component of the third order susceptibility, $\text{Im}[\chi^{(3)}]$, is directly proportional to β_{eff} , since the $\text{Im}[\chi^{(3)}]$ describes the speed of the NLA response of the material. **Equations 11** was used to determine the $\text{Im}[\chi^{(3)}]$ values for each sample, **Table 4.01**. The $\text{Im}[\chi^{(3)}]$ values for BODIPYs **(4)**, **(10)**, **(16)** and **(18)** benzene solution were found to be 1.49×10^{-10} , 5.16×10^{-10} , 7.21×10^{-10} , and 5.53×10^{-10} esu respectively. The $\text{Im}[\chi^{(3)}]$, values for BODIPYs **(11-14)** in DMSO solution were found to be 3.99×10^{-10} , 3.24×10^{-10} , 6.57×10^{-10} and 4.47×10^{-10} esu respectively. This suggests that BODIPY **(16)** (substituted with dimethylaminophenyl at the 3,5-positions) showed a better $\text{Im}[\chi^{(3)}]$, value compared to BODIPYs **(4)**, **(10)**, and **(18)** which have a lower dipole moment values as compared to **(16)**. Since the concentration and the energy were kept constant for all the compounds studied in this work; error due to those factors was minimized. Additionally, BODIPY **(16)** has a better $\text{Im}[\chi^{(3)}]$ value than BODIPY **(18)**, and this suggests that the electron donating inductive effect of the ethyl groups in the 2,6-positions does not enhance the OL properties of the dye as will be seen with other parameters. Furthermore, BODIPY **(13)** and **(14)** have better $\text{Im}[\chi^{(3)}]$ values when compared to BODIPYs **(11)** and **(12)**, and this again can be attributed to the dipole moments of the molecules. The magnitudes of the $\text{Im}[\chi^{(3)}]$ values for BODIPYs **(4)** and **(10)**, **(11)**, **(12)**, **(13)**, **(14)**, **(16)**, and **(18)** lie between 10^{-9} - 10^{-15} . This range of values has been previously reported for other organic compounds with promising OL properties [77, 78, 91]. Most of the BODIPYs studied in this thesis therefore have considerable potential as far OL applications are concerned.

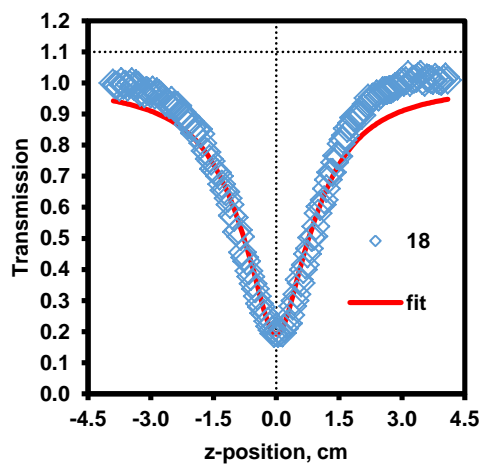
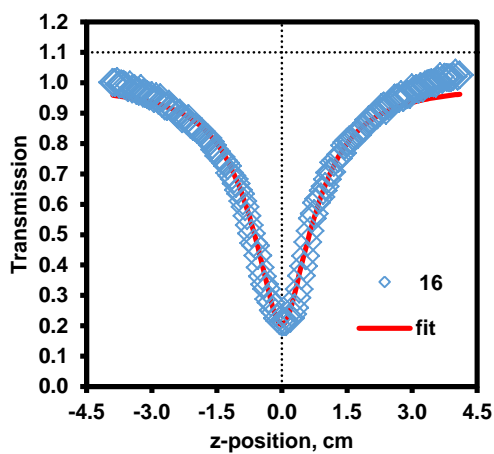
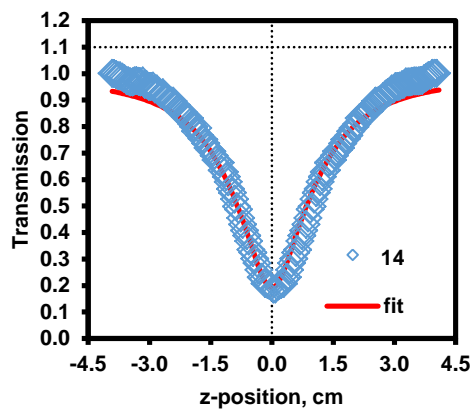
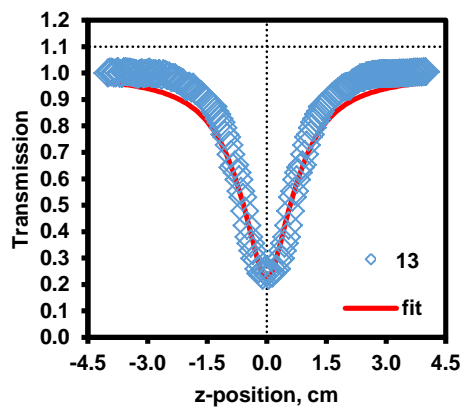
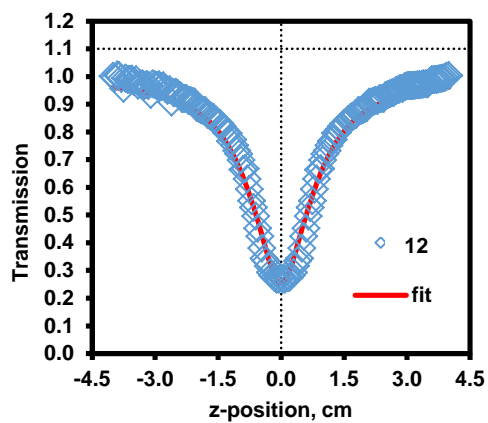
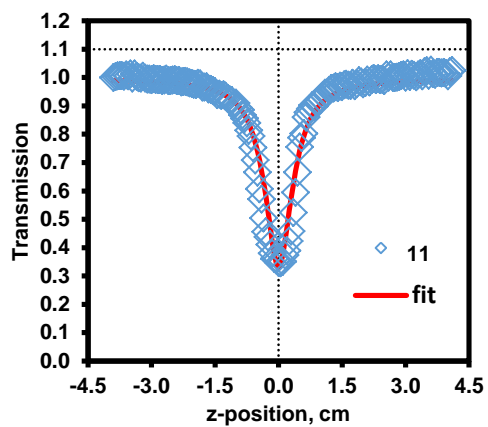
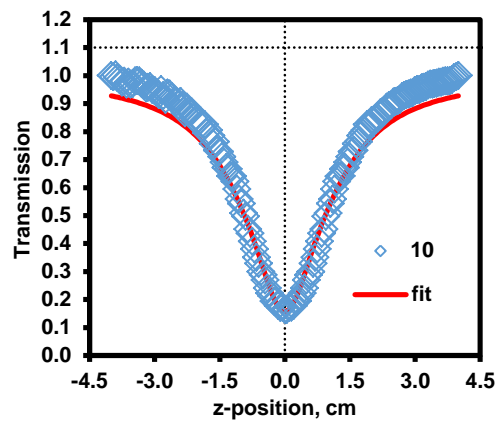
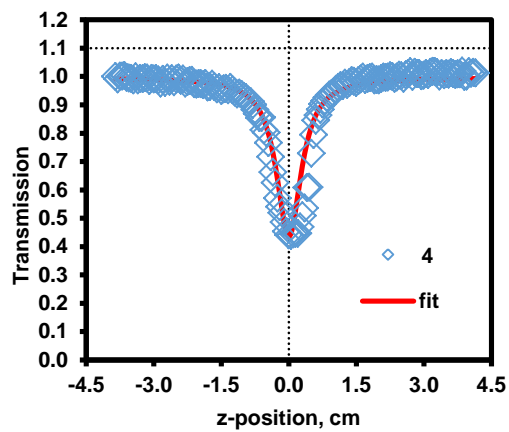


Figure 4.01 Open-aperture z-scans for all of the BODIPYs in DMSO for BODIPY (**11-14**) and in benzene for BODIPYs (**4**), (**10**), (**16**) and (**18**) at a fixed concentration of 21.6 μM and a laser pulse input energy of ca. 26 μJ . Detailed NLO parameters are provided in **Table 4.01**.

The second order hyperpolarizability, γ , is also a very important parameter when comparing the OL properties of different dyes. It measures the interaction of an incident photon with the permanent dipole moment of the BODIPY dyes at a molecular level, **Table 4.01** summarizes γ values of BODIPYs (**4**), (**10**), (**11**), (**12**), (**13**), (**14**), (**16**), and (**18**) in solution and in thin films for (**11-14**). This parameter is of significant importance when comparing the OL efficiencies of different molecules since it factors in concentration. The γ values for BODIPY (**16**) and BODIPY (**18**) appear to be superior to those of the other BODIPYs, which have lower dipole moment values than (**16**) and (**18**) (see Chapter 6) and this suggests that introducing a strong push-pull effect significantly enhances the OL properties.

4.2.1 Heavy atom effects

Table 4.01 contains the OL parameters for BODIPY (**11-14**). The motivation for this study was to investigate the effect of heavy atoms on the optical limiting properties of BODIPY dyes. These dyes were studied in DMSO, at a fixed concentration of 21.6 μM and a laser pulse input energy of 26 μJ , to enable direct comparisons. BODIPY (**11**) and (**13**) which are not brominated have better results with respect to the brominated analogues as far as their second order hyperpolarizabilities and third order susceptibilities are concerned. Additionally, a similar result is observed when the dyes are embedded in polystyrene polymer thin films. This suggests that for these dyes, the ESA is more efficient in the singlet manifold as compared to the triplet manifold and there is no obvious advantage provided by halogenating the structures at the 2,6-positions. The results of this part of the study were

recently published [91]. BODIPY (**13**) shows excellent OL results both in solution and in the polystyrene thin film. This suggests that BODIPY (**13**) is a good candidate for OL applications.

Table 4.01 The NLO parameters of the synthesized BODIPYs (**11-14**) in solution (DMSO) and thin films.

	^a Conc. [μM]	β_{eff} [cm.GW ⁻¹]	$Im[\chi^{(3)}]$ [esu]	γ × 10 ⁻³⁰ [esu]	α [cm ⁻¹]	I_{lim} [J·cm ²]	I_{00} [MW·cm ⁻²]
	^b Thick. [μm]	^b [cm.MW ⁻¹]					
(11)	^a 21.6	170	3.99×10^{-10}	8.1	0.77	1.09	355
(12)	^a 21.6	120	3.24×10^{-10}	4.8	0.72	0.87	355
(13)	^a 21.6	280	6.57×10^{-10}	13.3	2.08	0.76	355
(14)	^a 21.6	202	4.74×10^{-10}	9.6	0.77	1.09	355
(11)_TF	^b 23	^b 151	5.67×10^{-7}	7.4	173	0.049	47
(12)_TF	^b 22	^b 44	4.86×10^{-8}	5.1	46	0.056	47
(13)_TF	^b 24	^b 180	4.76×10^{-7}	15	165	0.094	47
(14)_TF	^b 24	^b 51	4.99×10^{-8}	10	58	0.078	47

4.2.2 Donor-acceptor effects

Table 4.02 contains OL parameters for BODIPYs (**4**), (**6**), (**10**), (**16**), and (**18**). The interest in this study is to investigate the effect donor and acceptor groups at different positions of the BODIPY core on the optical limiting properties of BODIPY dyes. These dyes were studied in benzene, at the same concentration and incident laser pulse energy, to enable a direct comparison.

The first comparison was made for BODIPY (**4**) and (**6**). BODIPY (**4**) possesses a D- π -A type core structure, while BODIPY (**6**) has an A- π -A type core (**Scheme 3.01**). The donor group in (**4**) is the *meso*-dimethylaminophenyl ring, and the acceptor of (**6**) is the phenoxyphthalonitrile group. The acceptor in both compounds are the two fluorine groups at the 4 and 4' positions of the BODIPY core. BODIPY (**4**) shows better OL properties than (**6**) which exhibits SA instead of RSA. This observation suggests that the presence of a large dipole moment generated by the D- π -A type structure is necessary to obtain an enhanced OL response.

BODIPYs (**10**), (**16**), and (**18**) which are π -extended BODIPYs with D- π -A type structures with differing push-pull effects (**Scheme 3.01**) were also studied. The extension of the π system by adding styryl groups in the 3,5-positions enhances the OL limiting properties of BODIPY dyes [77]. BODIPYs (**16**) and (**18**) have a much strong push-pull effect than the other π -extended BODIPY dyes because the presence of strong EDGs and EWGs enables electron transfer to occur across the structures. BODIPYs (**16**) and (**18**) display better OL properties when compared to the other dyes because of this property. The strength of the push-pull effect has been demonstrated to be of significant importance as far as designing dye molecules for future applications, since dyes with much stronger push-pull effects have better OL properties. More details will be provided on the calculation of dipole moments in Chapter 6.

Lastly, where BODIPYs (**16**) and (**18**) are concerned (**Scheme 3.01**), the introduction of ethyl groups at the 2,6-positions of the BODIPY core has no significant effect as far as OL limiting properties are concerned. When ethyl groups which have a donating effect relative to the hydrogen atom in (**16**) are introduced, the second order hyperpolarizability and third order susceptibility values decrease indicating that having protons at these positions has a

significant influence on the OL parameters, hence making BODIPY (16) the best candidate in this study for OL applications.

Table 4.02 The NLO parameters of the synthesized BODIPYs (4), (6), (10), (16), and (18) in benzene.

	Conc. [μM]	β_{eff} [$\text{cm}\cdot\text{GW}^{-1}$]	$Im[\chi^{(3)}]$ $\times 10^{-10}$ [esu]	γ $\times 10^{-30}$ [esu]	α [cm^{-1}]	I_{lim} [$\text{J}\cdot\text{cm}^2$]	I_{00} [$\text{MW}\cdot\text{cm}^{-2}$]
(4)	18.4	62	1.49	2.86	1.15×10^{-7}	2.53	355
(6)	18.4	SA	SA	SA	1.15×10^{-7}	SA	355
(10)	18.4	215	5.16	9.95	1.02	0.791	355
(16)	18.4	300	7.21	13.9	3.93	0.679	355
(18)	18.4	230	5.53	10.7	3.97	0.746	355

SA – saturable absorbance signal observed

4.2.3 Solvent effects

Table 4.03 contains OL parameters for BODIPY (4), (16), and (18), in different solvents. The objective of this study was to establish if the best performing dyes have solvent dependent properties. Interestingly, all the dyes perform poorly in DMSO which suggests that very polar solvent have negative effects on the OL properties of these dyes. The dyes display very low fluorescence quantum yields and lifetimes in DMSO than in benzene which suggests that in DMSO the S_1 state is less populated hence less ESA will occur. In contrast, the dyes perform better in less polar solvents, such as benzene. These dyes show high fluorescence quantum yields and lifetimes in benzene as can be seen in Chapter 3, and this means that the S_1 state is highly populated hence more ESA will occur. DCM has a dipole moment of 1.60 D, which is less than DMSO at 3.96 D, hence, as expected BODIPY (16)

behaves better in DCM than in DMSO. BODIPY **(16)** and **(18)** are prone to solvent effects because of the lone pairs on the dimethylamino groups (**Scheme 3.01**). These two compounds were also studied in DMSO and DCM to compare the effect of polar solvents on the OL properties of these two compounds. The other compounds were also studied in a different solvent, but they showed no significant difference. The results obtained are in agreement with the fluorescence quantum yields and lifetimes obtained in different solvents, since dyes with higher Φ_F and τ_F values have a greater population in the S1 state and hence are more likely to undergo ESA.

Table 4.03 The NLO parameters of the synthesized BODIPYs **(4)**, **(16)** and **(18)** in different solvents.

	Conc. [μM]	β_{eff} [cm.GW ⁻¹]	$\text{Im}[\chi^{(3)}]$ [esu]	γ [esu]	α [cm ⁻¹]	I_{lim} [J·cm ²]	Solvent
(4)	21.6	62	1.49×10^{-10}	2.86×10^{-31}	1.15×10^{-7}	2.53	Benzene
(4)	21.6	13.0	1.92×10^{-11}	3.61×10^{-31}	1.15×10^{-7}	---	DMSO
(16)	21.6	300	7.21×10^{-10}	13.9×10^{-30}	3.93	0.679	Benzene
(16)	21.6	301	6.56×10^{-10}	15.5×10^{-30}	0.54	1.21	DCM
(16)	21.6	10.1	1.50×10^{-11}	2.81×10^{-31}	3.93	---	DMSO
(18)	21.6	230	5.53×10^{-10}	10.7×10^{-30}	3.97	0.746	Benzene
(18)	21.6	10.0	1.49×10^{-11}	2.78×10^{-31}	3.97	---	DMSO

4.2.4 Energy variations

Table 4.03 provides OL parameters for BODIPY **(16)**. The objective of this study was to establish whether the best BODIPY increases its OL behavior as the input energy increases or otherwise. Only three energies were chosen, and interestingly as the input energy increases

the magnitude of the OL parameters decreases. Similar results were observed with the other dyes.

Table 4.04 The NLO parameters of the synthesized BODIPY (16) at different laser pulse input energies.

	Conc. [μM]	β_{eff} [cm.GW ⁻¹]	$\text{Im}[\chi^{(3)}]$ [esu]	γ [esu]	α [cm ⁻¹]	I_{lim} [J·cm ²]	I_{00} [MW.cm ⁻²]
(16)	36.9	420	9.80×10^{-10}	2.31×10^{-29}	0.621	0.557	490
(16)	36.9	540	1.18×10^{-9}	2.78×10^{-29}	0.621	0.461	400
(16)	36.9	686	1.49×10^{-9}	3.52×10^{-29}	0.621	0.300	290

4.2.5 Concentration variations

A concentration study was conducted for dye (16), which exhibited superior OL properties. The energy was kept constant (Table 4.05) and the study was done in benzene. As expected the OL parameters increased with increasing concentration. Similar results were observed with the other dyes.

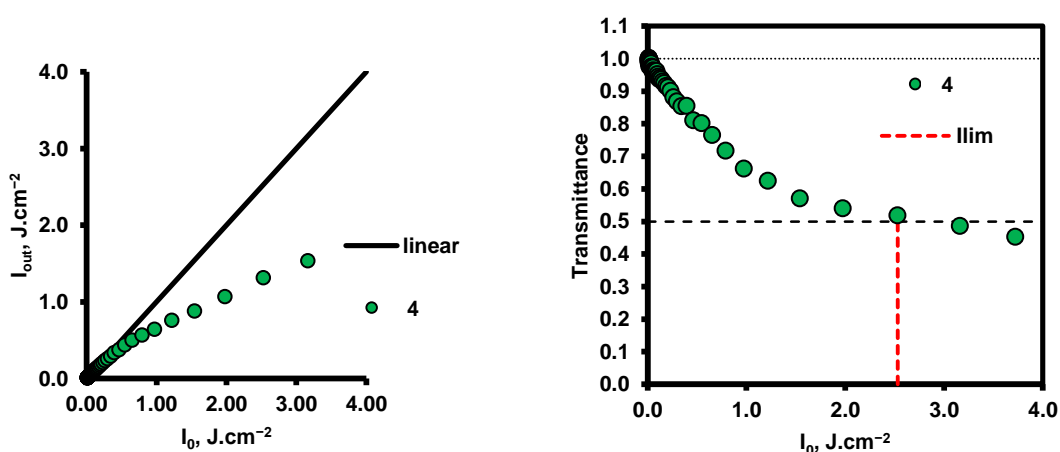
Table 4.05: The NLO parameters of the synthesized BODIPY (16) at different concentrations.

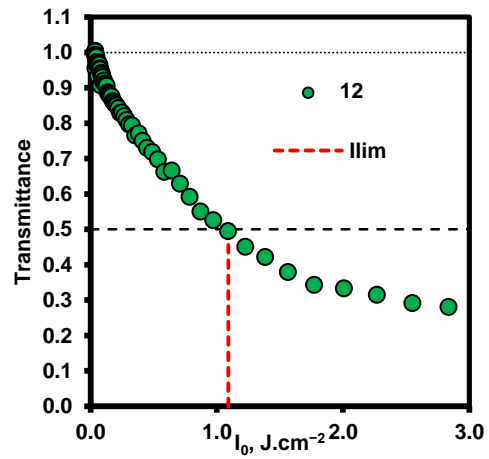
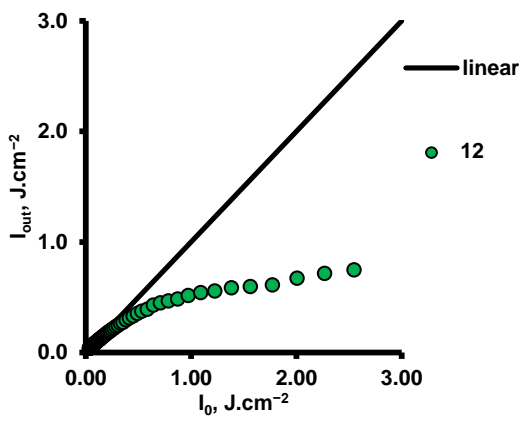
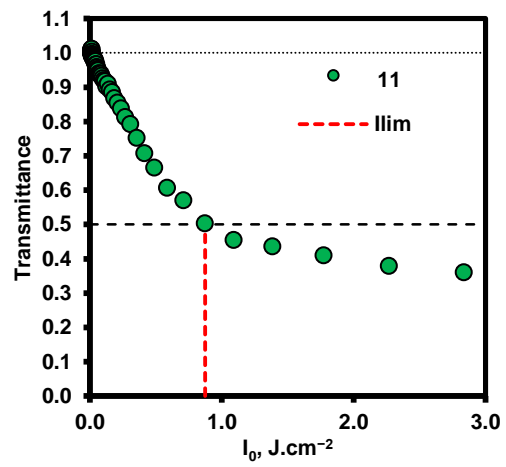
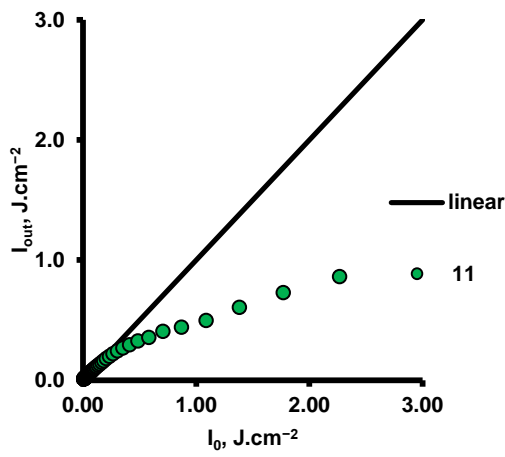
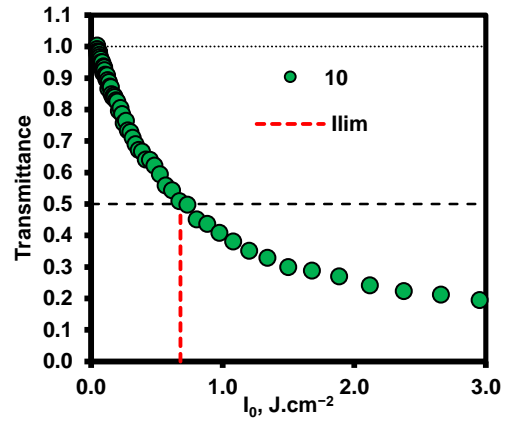
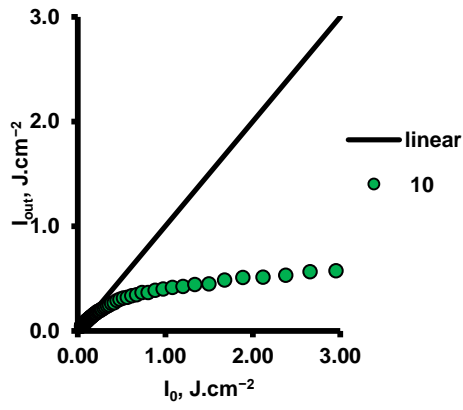
	Conc. [μM]	β_{eff} [cm.GW ⁻¹]	$\text{Im}[\chi^{(3)}]$ [esu]	γ [esu]	α [cm ⁻¹]	I_{lim} [J·cm ²]	I_{00} [MW.cm ⁻²]
(16)	12.3	45	9.80×10^{-11}	2.31×10^{-30}	0.541	1.21	418
(16)	18.4	271	5.91×10^{-10}	1.39×10^{-29}	0.553	1.19	418
(16)	24.6	351	7.65×10^{-10}	1.80×10^{-29}	0.564	0.652	418

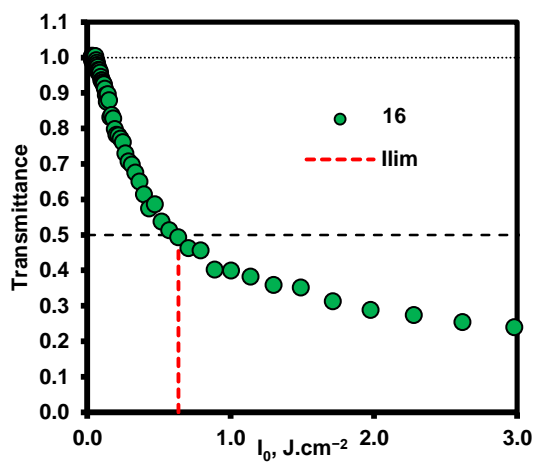
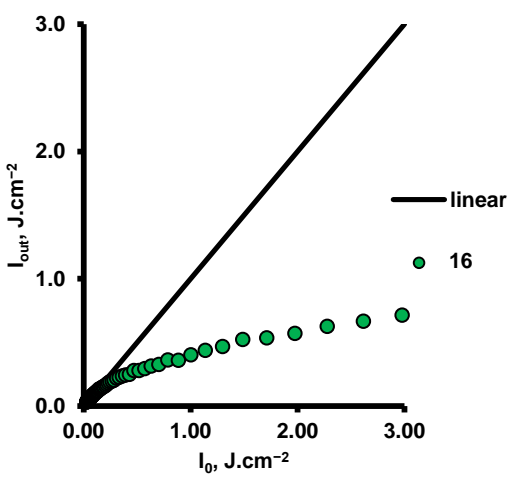
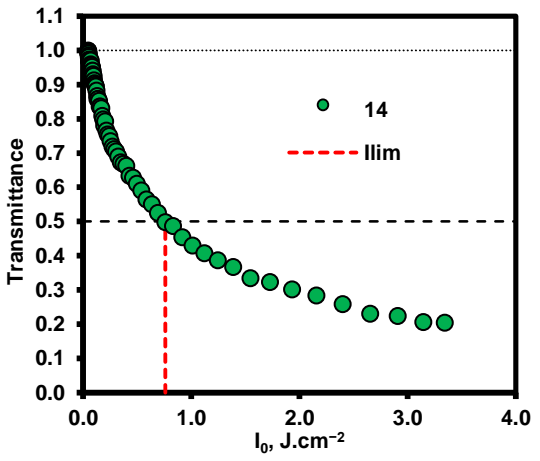
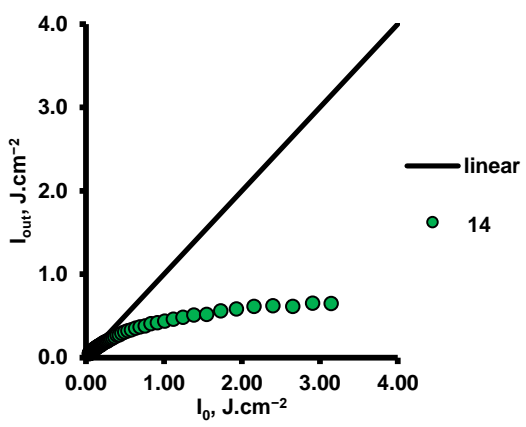
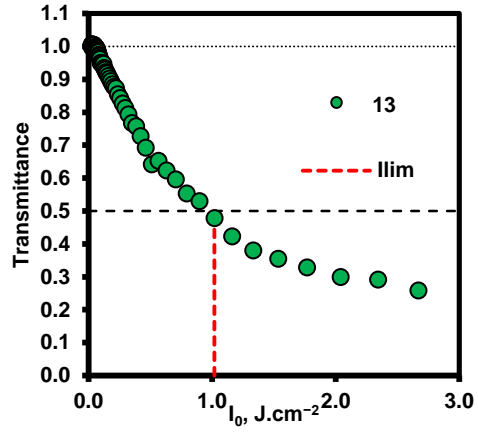
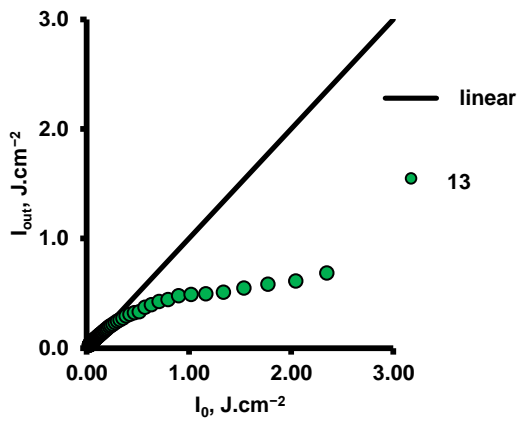
(16)	30.7	441	9.61×10^{-10}	2.27×10^{-29}	0.587	0.540	418
(16)	36.9	540	1.18×10^{-9}	2.78×10^{-29}	0.621	0.461	418

4.2.6 OL threshold (I_{lim})

The limiting threshold intensity or fluence, I_{lim} , is defined as the input fluence at which nonlinear transmittance is 50 % of the linear transmittance [134-137]. In other terms, this is the I_0 value where the material starts acting as an optical limiter. It is thus ideal to have I_l as low as possible, so that the material can start limiting at lower incident intensities. The values obtained in this work are well within damage threshold of $0.95 \text{ J}\cdot\text{cm}^{-2}$ [77]. The dyes that possess good OL properties have demonstrated to limit at low intensities which is desirable. This parameter is also affected by concentration, energy, solvent and push pull variations as can be seen in the previous sections. The value of I_{lim} drastically decreases when dye molecules are in the solid state, as can be observed with BODIPYs (11-14) (Table 4:01). This is desirable because for practical applications the dyes will be in solid state. The value of I_{lim} was determined using the plot transmittance vs. input fluence (Fig. 58).







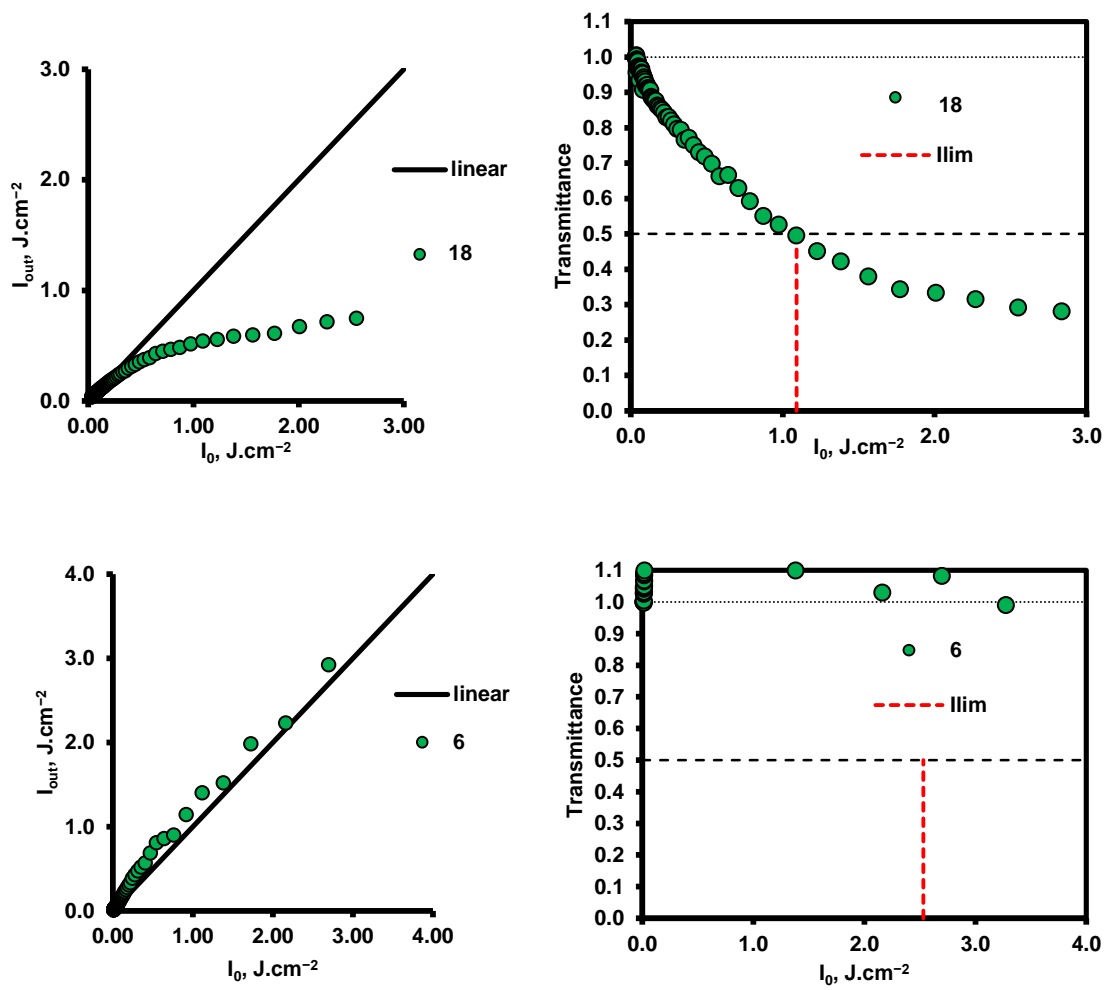


Figure 4.02 Output fluence (I_{out}) versus input fluence (I_0) curves for the BODIPYs at a fixed concentration of 21.6 μM and a laser pulse input energy of 26 μJ . The red dotted lines indicate the limiting threshold.

4.3 BODIPY– polystyrene thin films

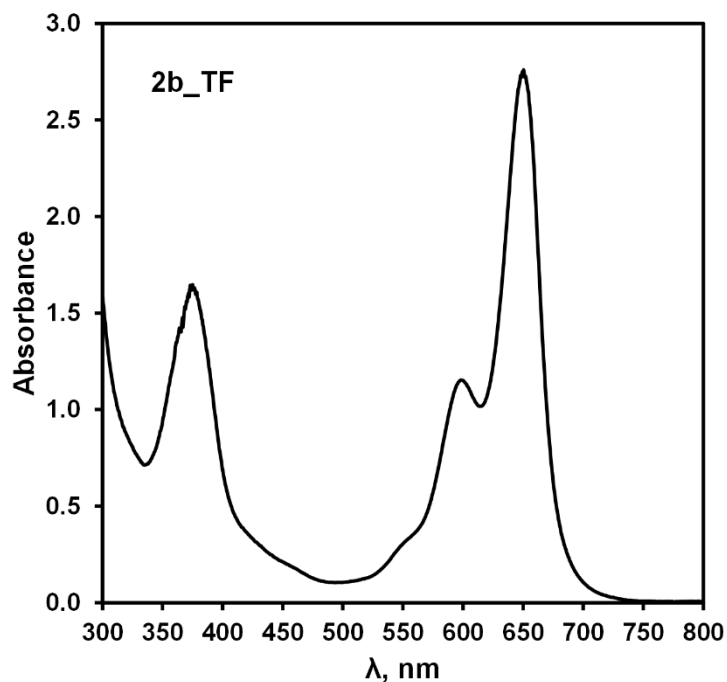


Figure 4.03 The UV-visible absorption spectrum of BODIPY (**13**) in the polystyrene thin film used for z-scan measurements. Reprinted with permission from Ref. 91; Journal of Porphyrins and Phthalocyanines 2018.

Transparent organic solutions are convenient for exploring the OL properties of dye molecules, because the concentration of the dye present in solution can be accurately determined. Furthermore, solution studies allow for nuanced determining of the OL properties of dye molecules, since it allows for concentration, solvent effects, energy variations, temperature variation studies to be conducted. However, since for practical applications the dyes must be in the solid state, the OL properties in solid state also have to be explored. Hence some of the dyes studied in this work were embedded in polymer thin films. In this work, BODIPYs (**11-14**) were embedded in polystyrene polymer thin films. The results of this portion of the study have already been published [91]. As would normally be anticipated [77], the OL properties of the dyes are enhanced once embedded in thin films (**Table 4.01**). The dyes showed no sign of band broadening due to aggregation in the thin films (**Fig 1.03**), so NLS due to aggregation is not anticipated. The most likely explanation

for the improved performance is the significantly greater concentration of the dye that was used in this context. The concentrations of the thin films were estimated using the Beer-Lambert Law to be 9, 11, 11, and 10 mM for BODIPY (**11-14**) [91], respectively. The β_{eff} and $[\text{Im}\chi^{(3)}]$ values are significantly higher than those obtained in solution (**Table 4.01**), but the γ values are comparable since the concentration of the BODIPY forms part of the calculation of this parameter.

4.4 Concluding remarks

From the results, we can conclude that some of the dyes with a higher dipole moment exhibit relatively high β_{eff} values and have very promising OL properties, since the incorporation of strongly electron donating styryl groups and electron withdrawing *meso* aryl groups results in a strong permanent dipole moment [128, 129]. The $\text{Im}[\chi^{(3)}]$ and γ values for BODIPY (**16**) and (**18**) appear to be superior than those of the other BODIPYs, which have lower dipole moment values (see Chapter 6). This can be attributed to presence of strong EWGs and EDGs in the molecule, which increases the dipole moment and hence increases the third order susceptibility. The results reported also explore the question of whether ISC to the triplet state enhances the optical limiting. When the results obtained for BODIPYs (**11**) and (**12**) are taken into consideration, BODIPY (**11**) was found to be superior to its brominated analogue BODIPY (**12**) (**Scheme 3.01**). The same trend was observed for BODIPYs (**13**) and (**14**). This suggests that the ESA process in the singlet manifold performs better than ESA in the triplet manifold as far as OL applications are concerned and that there is no significant advantage obtained through introducing heavy atoms at the 2,6-positions [128, 137]. Overall, BODIPY (**16**), (**13**) and (**18**) appear to be superior to the other BODIPYs with (**16**) performing best, followed by (**13**) and then (**18**), due to the relative magnitudes of their dipole moments [127, 128]. Most of the BODIPYs studied in this work have moderately high

α values at 532 nm. This suggests that there both 2PA and linear absorption are involved in populating the first excited state, **Fig 1.12**, and that ESA shapes the OL properties since nanosecond laser pulses were used during the studies.

Chapter 5:

Upconversion nanoparticles

5 UCNPs

The anti-Stokes process observed for UCNPs has gathered a lot of research interest in the last couple of decades due to its possible use in biological applications [65]. This is because of the ability to absorb NIR radiation, which is in the biological window (650-1350 nm), and produce a high energy output through the various energy transfer mechanisms detailed in **Section 1.35**. The UCNPs synthesized in this work have three main emission bands at 540 nm, 660 and 830 nm. The 540 nm band is more intense than the other two by design. Since BODIPY (**5**) absorbs at 539 nm in DMSO there will be a very good spectral overlap between the 540 nm emission of the UCNPs and the 539 nm absorption of BODIPY (**5**) in **Scheme 3.01**. Additionally, a good spectral overlap yields an efficient FRET. Furthermore, the objective in linking the BODIPY and the amine-functionalized UCNPs is to have a shorter distance between the donor and the acceptor to enable efficient FRET. Given that BODIPY (**5**) (the photosensitizer (PS)) is expected to have efficient ISC to the T_1 state and a high singlet oxygen quantum yield, FRET will result in a high singlet oxygen quantum yield for the conjugate. The main advantage this conjugate provides lies in the low signal to noise ratio, in the context of biological autofluorescence [65], which is often a major drawback for photosensitizers absorbing in the high energy region of the spectrum.

This section explores the conjugation of the carboxylic acid functionalized BODIPY (**5**) and the amine-functionalized UCNPs, the singlet oxygen production of BODIPY alone and lastly the singlet oxygen generation of the conjugate for potential application in PDT. The nanoparticles were synthesized following a thermal decomposition method utilizing Yb^{3+} as the sensitizer and Er^{3+} as the activator in a fluoride host matrix as detailed in **Section 1.33** and **2.5**. Characterization of the UCNPs was carried out using a number of techniques. Transmission electron microscopy (TEM) and atomic force microscopy (AFM) were used to

determine particle size and dispersity. Energy-dispersive X-ray spectroscopy (EDS) was carried out to confirm the elemental composition of the particles and the conjugate. Powder x-ray diffraction (XRD) was used to examine the phase purity, and steady state and time-resolved fluorescence spectroscopy (TCSPC) to study the emission characteristics measured upon 978 nm laser excitation. Functionalization of the UCNPs with amine groups was characterized by infrared spectroscopy (IR) and (EDS) to confirm the presence of the amine group.

5.1 Characterization of UCNPs

5.1.1 Transmission electron microscopy (TEM)

TEM provides the first level characterization of the nanoparticles, **Fig 5.01**. Consistently, uncapped UCNPs (oleate@UCNPs) exhibited low levels of aggregation and were well dispersed with a good size distribution. The oleate@UCNPs displays a narrow size distribution with relatively small spherical shapes (average diameter of ca. 40 nm) due to a restriction of the Oswald ripening process with the temperatures being held at 280 °C for the duration of the annealing phase [138, 139]. With the Si@UCNPs, we see an increase in the size distribution and this can be vividly seen with the silica shell around the nanoparticles (average diameter of ca. 50 nm). Additionally, Si@UCNPs display small amounts of aggregation and this is also observed in the silanized particles, **Fig 5.01**. This aggregation is related to slow evaporation of the solvent during sample preparation. It is observed, however, that the NH₂@UCNPs show high levels of aggregation as they exhibit considerable clustering, **Fig 5.01**. This aggregation can be attributed to the presence of the NH₂ group [140].

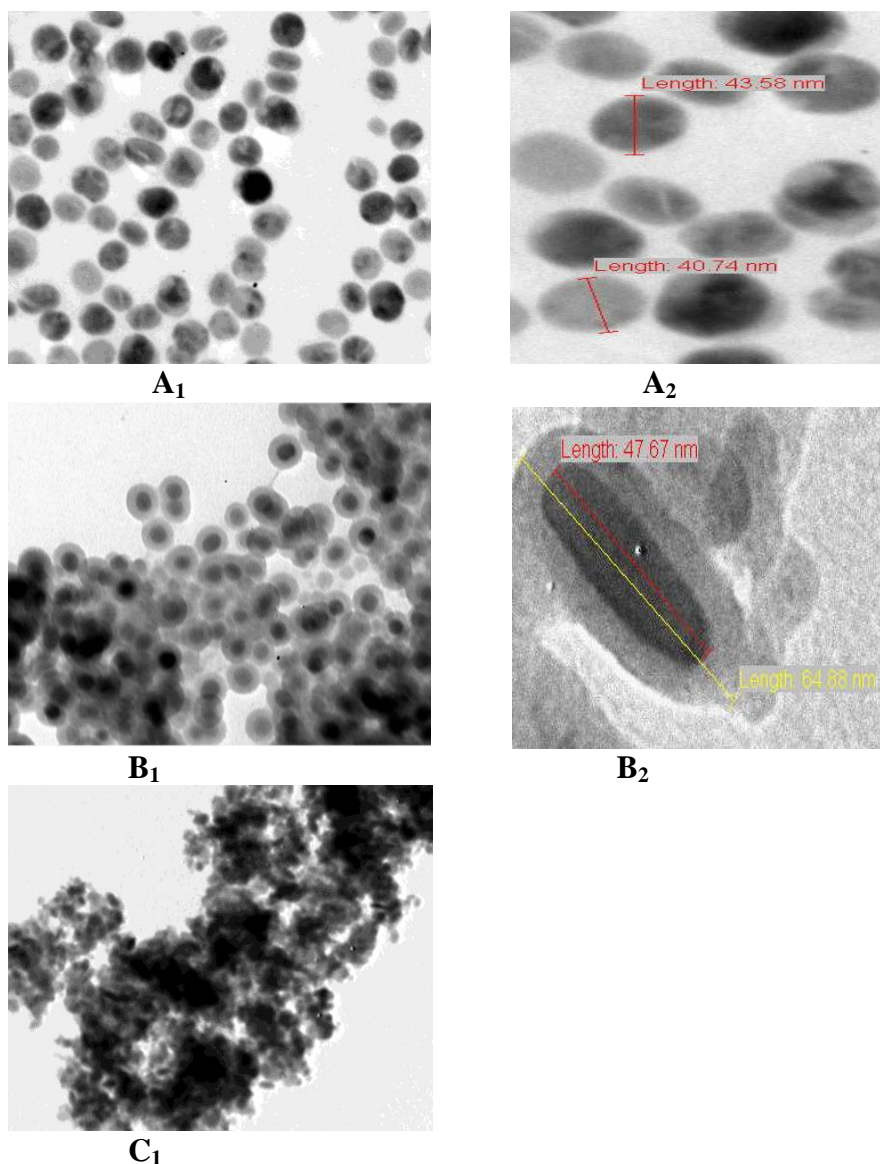


Figure 5.01 TEM images of Oleate@UCNPs (A₁, A₂), Si@UCNPs (B₁, B₂) and NH₂@UCNPs (C₁).

5.1.2 Atomic force microscopy (AFM)

AFM has three major utilities: force measurement, imaging, and manipulation. For our purposes, we used AFM for imaging which is a complementary technique to the TEM study above. The purpose of carrying out both AFM and TEM is because of the resolution power of AFM; hence, the results from both techniques complement each other. The NH₂@UCNPs and the BODIPY@UCNP conjugate are analyzed by this technique to compare the size distribution of the two after conjugation of the BODIPY to UCNPs. As expected, it is evident

that the average diameter distribution of the $\text{NH}_2\text{@UCNPs}$ is ca. 50 nm **Fig 5.02**, which is complementary to the value obtained for the Si@UCNPs **Fig 5.01**. Additionally, with AFM we were able to determine the size distribution of the highly aggregated $\text{NH}_2\text{@UCNPs}$. The BODIPY@UCNP conjugate shows a size distribution three times that of the $\text{NH}_2\text{@UCNPs}$ (average diameter of ca. 150 nm) and this can be attributed aggregation, as organic materials are known to aggregate when viewed with an imaging technique [140]. It is noteworthy that without AFM it would have been very difficult to obtain the size distribution of the conjugate simply because of the high levels of aggregation.

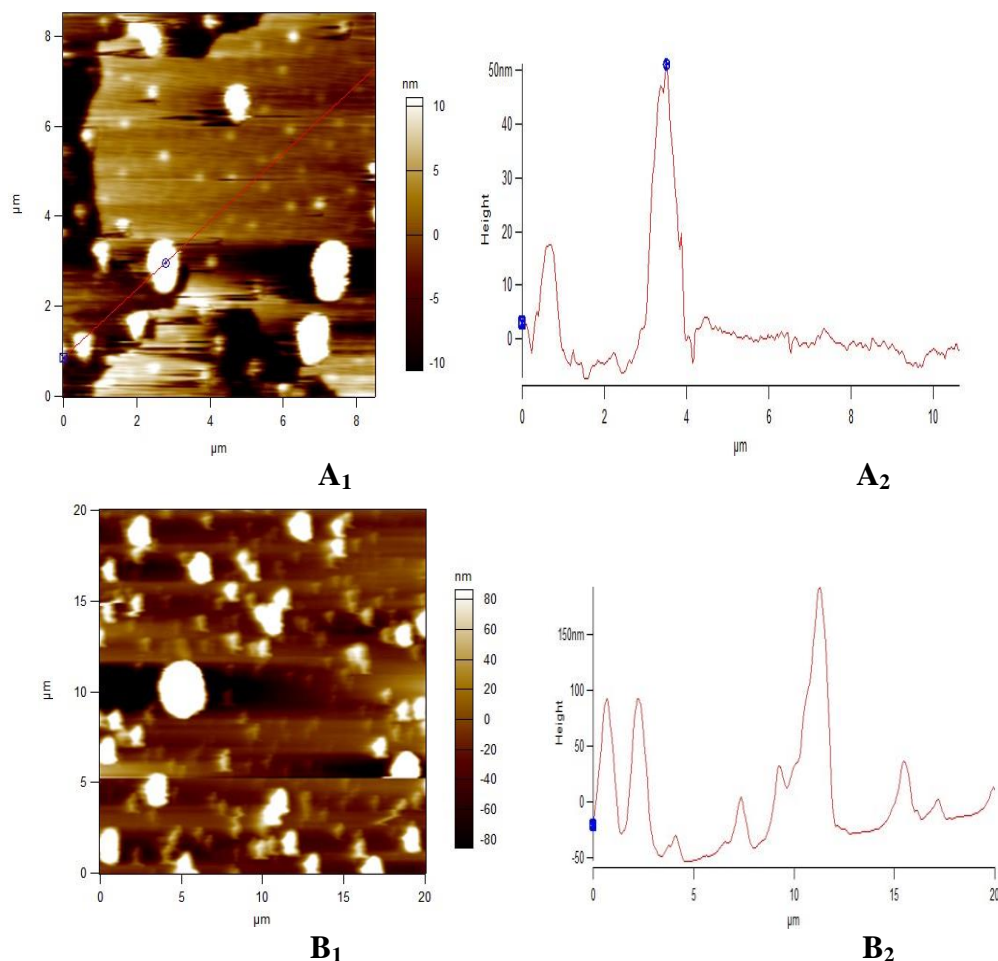


Figure 5.02 AFM images and average size distribution of $\text{NH}_2\text{@UCNPs}$ (A₁, A₂) and of BODIPY@UCNPs (B₁, B₂), respectively.

5.1.3 Energy-dispersive X-ray spectroscopy (EDS)

The elemental composition of the oleate@UCNPs, Si@UCNPs, NH₂@UCNPs and BODIPY@UCNPs was confirmed by EDS. **Fig 5.03A** shows the oleate@UCNPs and the expected essential elements Yb³⁺, Er³⁺, Y³⁺, F, are observed, this confirms the successful formation of the UCNPs. **Fig 5.03B** shows the presence silicon (Si) which confirms the successful coating with silica. Additionally, it also shows that the elements in oleate@UCNPs are preserved upon coating with silica. **Fig 5.03C** indicates the presence of the nitrogen element, which confirms successful functionalization with NH₂. It should be noted that it is challenging to identify nitrogen from EDS as it overlaps with oxygen. It is evident, however, that the nitrogen is present in **Fig 5.03C**. Lastly, **Fig 5.03D** shows the presence of iodine, which comes from the BODIPY dye that is conjugated on the surface of the UCNPs. This confirms the presence of BODIPY (**5**) on the surface of the UCNPs.

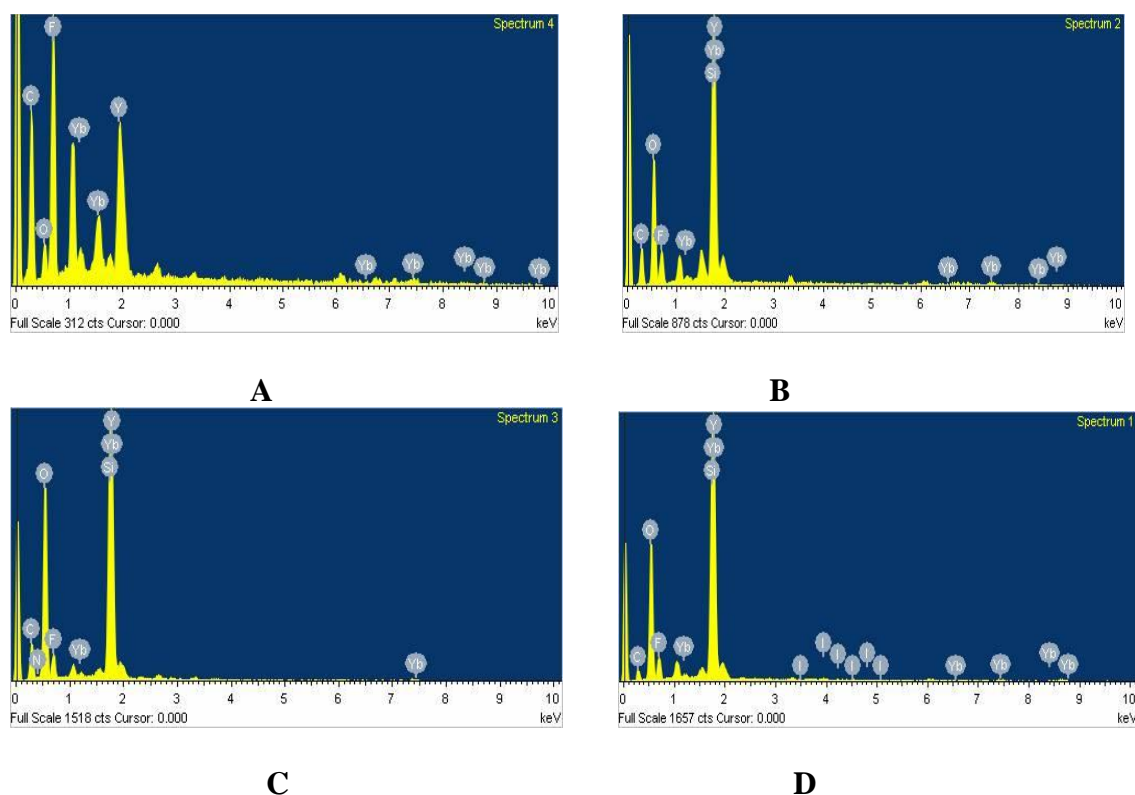
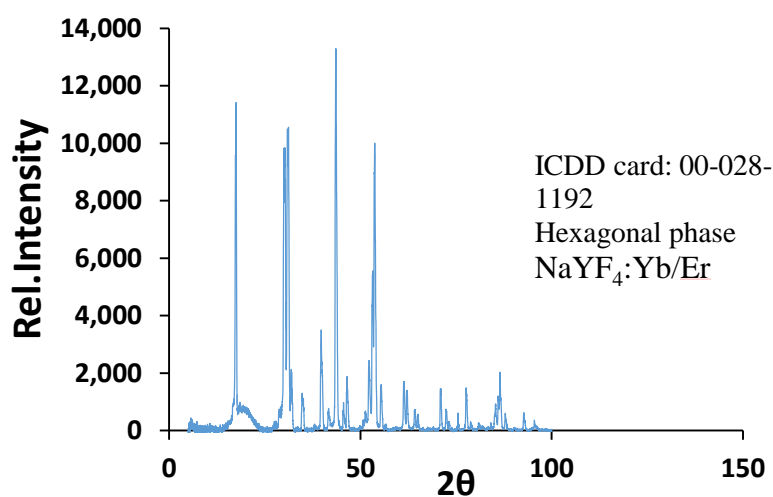


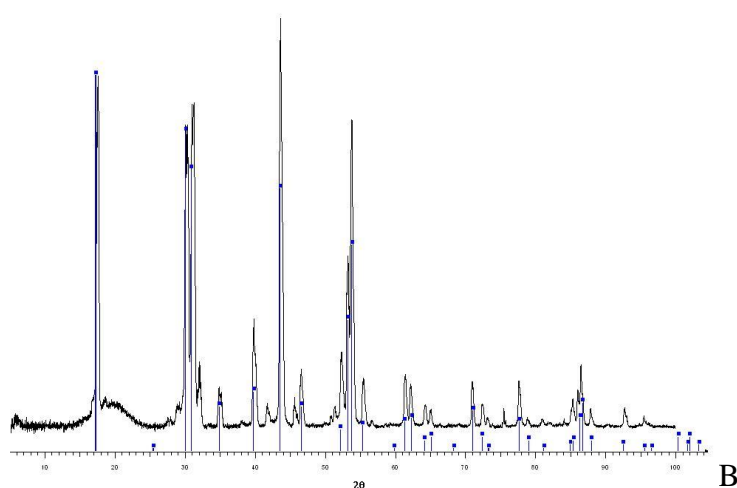
Figure 5.03 EDS images of Oleate@UCNPs (A), Si@UCNPs (B), NH₂@UCNPs (C) and BODIPY@UCNPs (D).

5.1.4 Powder x-ray diffraction (XRD)

The phase was confirmed with the XRD patterns indexed to the β - NaYF_4 nanocrystals below with 2θ values at 17.1, 29.9, 30.8, 34.7, 39.8, 43.5, 46.5, 53.7 and 61.3° corresponding to the (100), (110), (101), (200), (111), (201), (210), (211) and (112) hkl miller indices, respectively (JCPDS standard card no 28-1192). It should be noted that JCPDS is outdated and the ICDD is normally now used instead. Detailed analysis revealed that there were no impurities since the observed peaks are consistent with the pure β -phase. **Fig 5.04B** shows that the peaks obtained are an exact match to the reference peaks.



A



B

Figure 5.04 (A) The XRD pattern for β - NaYF_4 nanocrystals, (B) the XRD pattern for β - NaYF_4 nanocrystals with reference peaks highlighted.

5.1.5 Infrared spectroscopy (IR)

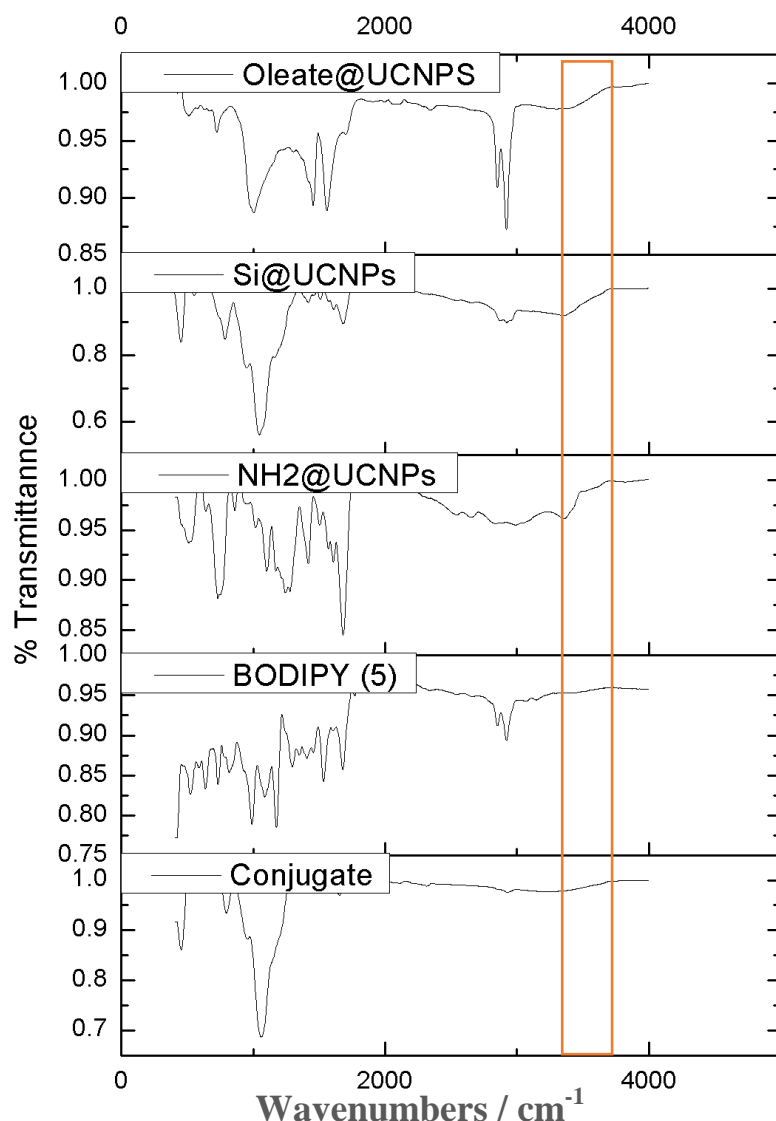


Figure 5.05 The FT-IR spectra of Oleate@UCNPs, Si@UCNPs, NH₂@UCNPs, BODIPY (5) and the UCNP-BODIPY conjugate. The red box highlights the presence and disappearance of amine stretch band.

The infrared spectroscopy in **Fig 5.05** provides evidence of functionalization and conjugation. The (O-H stretch) 3285 cm⁻¹ is observed in the spectra of the Oleate@UCNPs and Si@UCNPs. This is expected because of the carboxylic group from the Oleate@UCNPs and the OH from the Si@UCNPs as is evident in **Scheme 2.20**. An O-Si stretch at 1050 cm⁻¹ is observed upon coating with silica. The 3365 cm⁻¹ (N-H stretch) and 1680 cm⁻¹ (N-H bend)

peaks are observed upon functionalization with NH₂. As expected, the O-Si stretch is still consistently observed after the conjugate is formed. The spectrum of the conjugate shows the complete disappearance of 3365 cm⁻¹ (N-H stretch) and 1680 cm⁻¹ (N-H bend) peaks, which provides evidence that the conjugation was successful.

5.1.6 Steady-state and time-resolved fluorescence spectroscopy (TCSPC)

The steady-state fluorescence spectra for the UCNPs were obtained by excitation with an Ekspla NT-342B-20-AW laser. Various emission bands can be observed from the activated levels of Er³⁺ at ca. 840 (NIR), 658 (red), 540 (green) and 410 nm (blue). The transitions giving rise to these bands are shown in the spectra, **Fig 5.06B**. The dominant emission bands at ca. 540 and 658 nm are associated with the ²H_{11/2} and ⁴F_{9/2} states, respectively, and result from 2PA [54]. The relative intensities of the peaks reflect firstly the efficiency of the system as an upconverter, and secondly the relative extent to which weaker nonradiative relaxations occur.

The weaker 840 and 410 nm emission bands, **Fig 5.06A**, arise from the lowest and highest states, respectively, of the Er³⁺ ion by comparison with the 540 and 658 nm bands. Access to the higher energy states requires multiple steps of resonant absorption and this is of significantly lower likelihood in probability terms [53, 54]. The weak peak in the 840 nm region can be assigned to either direct absorption to the activator or a single resonant transfer from the sensitizer, due to the near resonance between the Er³⁺ state (⁴I_{11/2}) and a Yb³⁺ state (²F_{5/2}) which have a ca. 4 cm⁻¹ mismatch [53, 54]. We can also assume that since no emission bands are observed from the activator ⁴I_{11/2} or ⁴I_{13/2} states that cross relaxation from the Yb³⁺ ion and radiative relaxation from the ⁴I_{11/2} state does not occur [53-55]. **Fig 5.06B** shows the spectral overlap between the emission at 540 nm of the UCNPs and absorbance of BODIPY (**5**) at 539 nm. This good spectral overlap is a good indication that efficient FRET should

occur. Upon laser excitation of the conjugate at 978 nm, **Fig 5.06C**, the entire 540 nm emission band of the UCNPs was observed to be absorbed by the BODIPY dye. This demonstrates that the FRET process on which the intended application depends occurs.

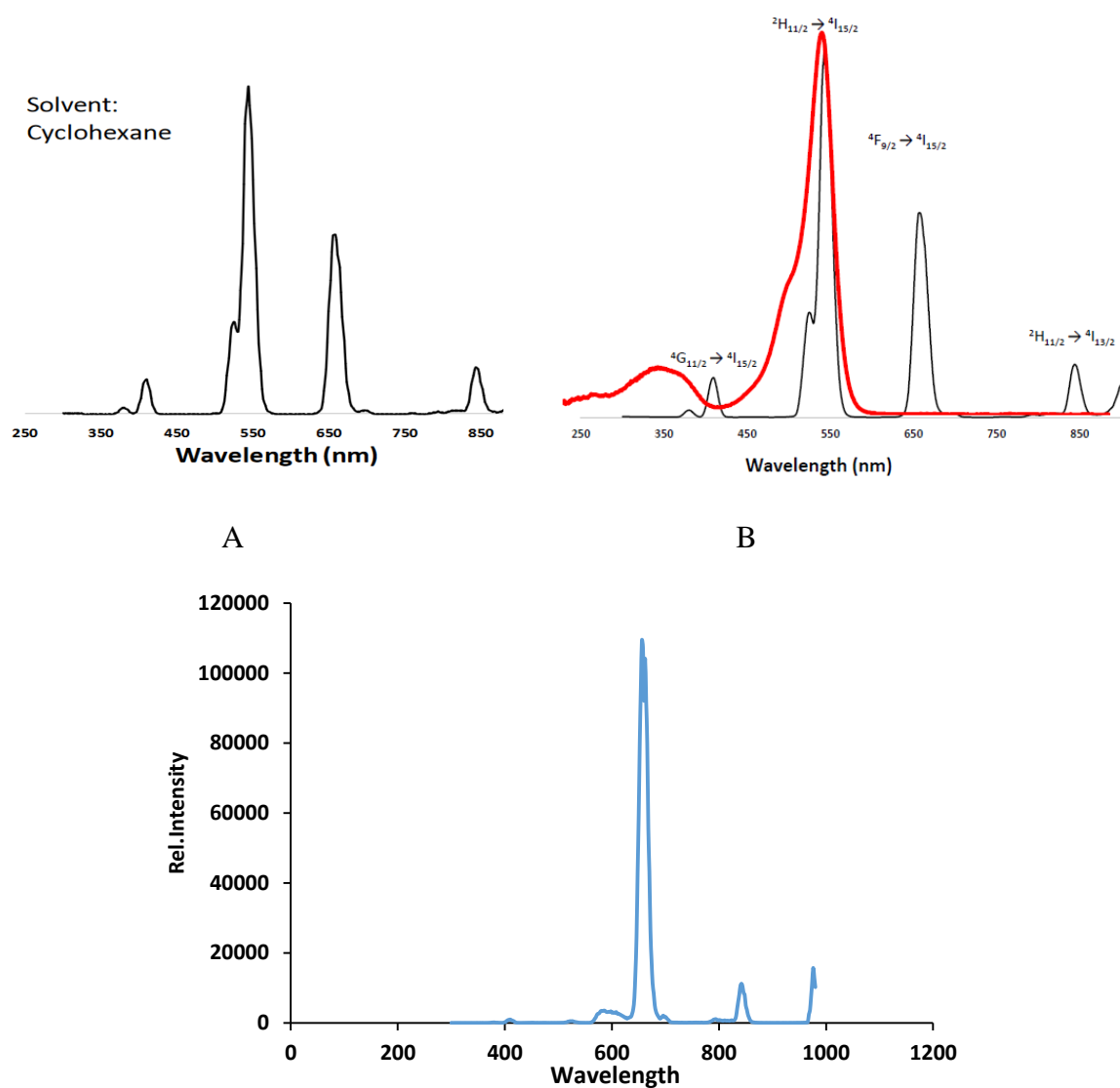


Figure 5.06 The fluorescence of the UCNPs (A), the spectral overlap of the UCNP fluorescence and the absorption bands of BODIPY (**5**) (B) and the effect of FRET on the fluorescence of the UCNP-BODIPY conjugate upon irradiation at 978 nm (C).

5.1.7 Photophysical properties.

Singlet oxygen and fluorescence quantum yield studies were carried out in DMSO. BODIPY (5) as expected has a high singlet oxygen quantum yield (Table 5.01). However, when the conjugate was irradiated at 978 nm there were problems with the photostability of the BODIPY dye, this made it impossible to determine a singlet oxygen quantum yield value and to carry the studies forward onto PDT related cell studies. This is not favourable as the photosensitizer needs to be stable throughout the irradiation process. When the conjugate was irradiated 540 nm, however, the conjugate was stable (Fig 5.08) and exhibited a slightly improved singlet oxygen quantum yield value relative to BODIPY (5) (Table 5.01).

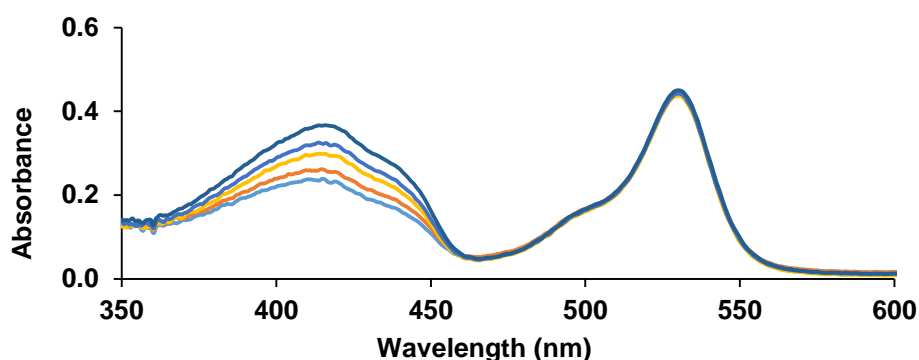


Figure 5.07 Degradation of DPBF by singlet oxygen generated through photoirradiation of BODIPY (5) measured at one minute intervals.

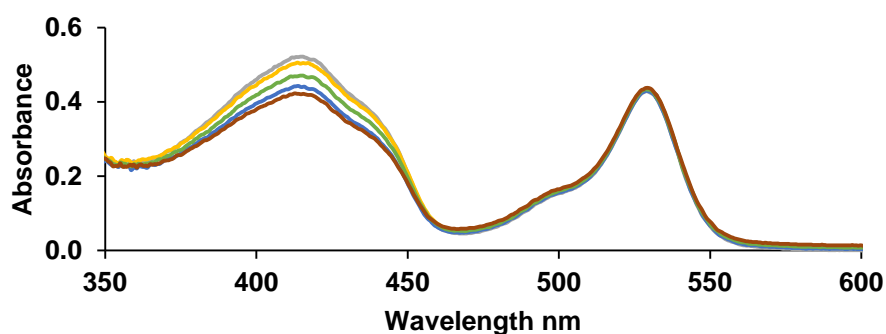


Figure 5.08 Degradation of DPBF by singlet oxygen generated through photoirradiation of the UCNP-BODIPY conjugate measured at one minute intervals.

Table 5.01 Photophysical data for BODIPY (**5**) and the UCNP-BODIPY conjugate.

Solvent	Compound	$\lambda_{\text{abs}}/\text{nm}$	Φ_{f}	Φ_{Δ}
DMSO	BODIPY (5)	539	0.01	0.76
DMSO	Conjugate	972	---	0.90

5.2 Concluding remarks

Silica-coated UCNPs were successfully synthesized and functionalized with amine groups. Carboxylic acid substituted BODIPY (**5**) was synthesized and successfully conjugated to the NH_2 @UCNPs. BODIPY (**5**) was selected for use in this context, since it has high a singlet oxygen quantum yield value. BODIPY (**5**) has an excellent spectral overlap with the main emission band of the UCNPs at 540 nm, **Fig 5.06B**. The excellent spectral overlap results in highly efficient FRET as was observed with the conjugate in **Fig 5.06C** under 978 nm laser excitation and this demonstrates that conjugates of this type merit further study. The initial goal of the study was to excite the conjugate at 978 nm and determine the singlet oxygen quantum yield at that wavelength. However, this was unsuccessful since there were problems with the photostability of the BODIPY dye and this made it impossible to determine a singlet oxygen quantum yield and continue onto PDT related cell studies. When the conjugate was excited at 540 nm, an increase in the singlet oxygen generation was observed, this could be due to changes in the amount of conformational flexibility due to the conjugation. The enhancement of the singlet oxygen quantum yield value could provide a potential breakthrough as far as deep tissue penetration is concerned with PDT, if 978 nm laser light can successfully be used in future.

Chapter 6: Molecular Modeling

6 Molecular modelling

6.1 Geometry optimizations and TD-DFT calculations

The density functional theory (DFT) method is a powerful tool that can be used to predict the photophysical properties of molecular dyes. It is, however, not always accurate in its predictions and suitable exchange-correlation functionals and basis sets need to be selected. Trends observed in DFT calculations can be used to inform the direction of a particular research project. The Gaussian 09 software package was used to perform geometry optimizations for BODIPY dyes **(1)**, **(3)**, **(10)**, **(11)**, **(12)** and **(18)** (**Scheme 3.01**) by using the B3LYP functional with SDD basis sets, which offers reasonable approximations for the heavy bromine atoms that were used in this study. While the B3LYP functional has been used extensively for structural analysis, it has a tendency to greatly underestimate long-range charge transfer excitations in TD-DFT calculations, which are frequently encountered with BODIPY dyes [141, 142]. TD-DFT calculations were carried out on the B3LYP optimized geometries using the Coulomb-attenuated B3LYP (CAM-B3LYP) functional in order to determine the electronic absorption properties of selected BODIPY dyes. The CAM-B3LYP functional is better suited to handling transitions with charge transfer character since it combines elements of the hybrid B3LYP functional with increasing fractions of Hartree-Fock (HF) exchange parameters, resulting in a functional with improved long-range capabilities [141, 142]. This proved to be sufficiently accurate for the determination of the main trends and structure-property relationships of the series of structurally related BODIPY dyes selected for study in this regard.

6.2 BODIPYs for NLO applications

Molecular modelling provides a lot of information regarding the spectroscopic properties of the compounds. The calculations also provide the dipole and quadrupole moments. For the purposes of this work, the focus will be on dipole moment (μ) values in Debyes derived from the TD-DFT calculations at the CAM-B3LYP/SDD level of theory. A comparison is made between the magnitude of the calculated dipole moment values and the main OL parameters of the compounds, **Table 6.01**. By definition, the second order hyperpolarizability, γ , measures the interaction of incident light with the permanent dipole moment of the BODIPY dye. A larger dipole moment should enhance the interaction with the incident light and hence larger γ values are anticipated for BODIPYs with D- π -A type structures.

BODIPY (**4**) has a larger dipole moment than BODIPY (**6**) (**Table 6.01**), hence as expected (**4**) has better OL properties than (**6**) as seen in **Table 4.02**. Furthermore, as stated in Chapter 4, BODIPYs (**10**), (**13**), and (**18**) have large dipole moments and hence have relatively large γ values. Again, as stated in Chapter 4, the two most important parameters for OL are γ and $\text{Im}[\chi^{(3)}]$, and since these two parameters are directly proportional, **Equation 12**, if one is enhanced so is the other. The positive relationship between these two parameters means that a compound with suitable 2PA properties in terms of a polarizable π -system and a higher dipole moment inherently should have superior OL properties. This postulate holds in **Table 6.01** with all of the compounds, as the dipole moment decreases so do the two most important OL parameters. The only obvious exception is BODIPY (**13**), which has values for γ and $\text{Im}[\chi^{(3)}]$ that are a bit higher than the predicted dipole moment would suggest. This could be a result of solvent effects since solvents interact with compounds differently [143]. This observation does not negate the significance of the overall trend identified in the calculated dipole moments and the OL parameters.

Table 6.01 The NLO parameters of the synthesized BODIPYs in solution with their calculated dipole moments.

	Conc. [μM]	β_{eff} [$\text{cm}\cdot\text{GW}^{-1}$]	$Im[\chi^{(3)}]$ $\times 10^{-10}$ [esu]	γ $\times 10^{-30}$ [esu]	α [cm^{-1}]	I_{lim} [$\text{J}\cdot\text{cm}^2$]	I_{00} [$\text{MW}\cdot\text{cm}^{-2}$]	Dipole mom. [μ]
(4)	21.6	62	1.49	2.86	1.15×10^{-7}	2.53	355	---
(10)	21.6	215	5.16	9.95	1.02	0.791	355	4.13
(11)	21.6	180	4.22	8.54	1.02	1.09	355	1.79
(13)	21.6	280	6.57	13.3	2.08	0.76	355	2.15
(16)	21.6	300	7.21	13.9	3.93	0.679	355	4.95
(18)	21.6	230	5.53	10.7	3.97	0.746	355	4.35

6.3 Molecular modelling for BODIPY dyes: (1), (3), (10), (11), (12), and (18)

The TD-DFT calculations predict that the lowest lying $S_0 \rightarrow S_1$ transition is almost entirely associated with the HOMO \rightarrow LUMO one-electron transition (**Table 6.02**). The C_{2v} symmetry possessed by BODIPYs because of complexation with a boron difluoride ligand results in the HOMO and LUMO being well-separated from other MOs [144]. Thus, when considering the impact of structural changes on the properties of the main spectral band, it is the HOMO and LUMO, which should be considered, since the other MOs are largely uninvolved. A red-shift of the BODIPY main spectral band arises when structural alterations change the energies of the HOMO and LUMO in such a way that the HOMO–LUMO band gap is narrowed.

Two major modifications are made to the BODIPY core in this work. To increase singlet oxygen generating capacity, bromine and iodine atoms are added at the 2,6-positions,

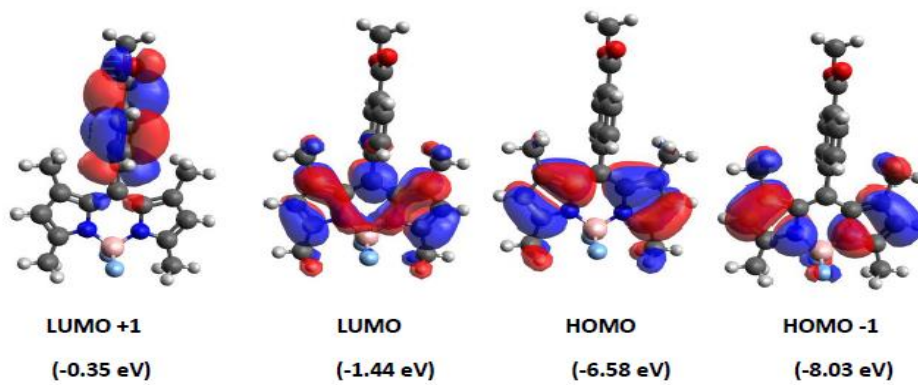
promoting ISC to the triplet state. Thereafter, styryl moieties are added at the 3,5-positions to red-shift the main spectral band of the BODIPY towards the biological window. Molecular modelling allows for a better understanding of these phenomena. The calculated oscillator strengths and band energies of BODIPY (**1**), its 2,6-dibrominated analogue (**3**), and its 3,5-di(4-benzyloxy)styryl and di(4-dimethylamino)styryl substituted counterpart (**Fig. 6.03**) indicate the predicted changes of the spectral bands upon modification. The addition of bromine and iodine groups at the 2,6-positions results in a red-shift of ca. 30 nm 39 nm, respectively. Although the addition of bromine/iodine atoms at these positions results in a stabilization of the whole stack of π -MOs (**Fig. 6.02**), halogens are able to donate a pair of electrons in resonance forms, which leads to some degree of destabilization due to the mesomeric interactions. At the 2,6-positions, there are significant MO coefficients in the HOMO, but smaller MO coefficients in the LUMO (**Fig. 6.01**). Hence, when bromine atoms are added at the 2,6-positions, they cause a net relative destabilization of the HOMO, resulting in the narrowing of the HOMO–LUMO band gap, which leads to the red-shift of the observed spectral bands.

It is evident in **Fig. 6.01** that the MO coefficients at the 3,5-positions are unevenly distributed in the HOMO and LUMO of the brominated and unbrominated compounds. A larger MO coefficient in the HOMO suggests that any structural alterations at this position should affect the HOMO to a more significant extent than the LUMO, and can thus result in a change in magnitude of the HOMO–LUMO band gap. Incorporating styryl moieties at the 3,5-positions therefore results in a further red-shift between 115–150 nm, depending on the functional groups present on the styryl moiety. In the experimental data, it is evident that styryl groups with strong EDGs attached to the benzene ring tend to destabilize the HOMO slightly more than those with strong EWGs as is seen in **Fig. 6.02**. The HOMO→LUMO transition remains the dominant one-electron transition for the main absorption band of the styryl-substituted

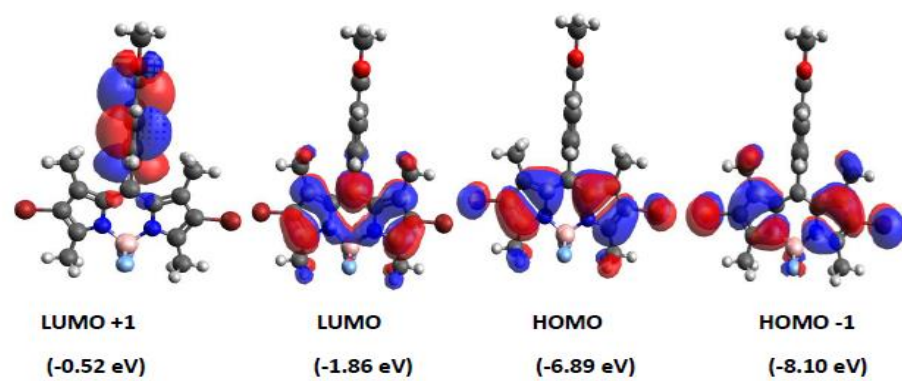
BODIPY dyes (**Table 6.02**). Other transitions with significant oscillator strengths are primarily associated with the styryl substituents and result in the absorption bands that are observed over the 300–450 nm region.

BODIPYs (**11**) and (**10**) are very similar, differing only in that BODIPY (**10**) has ethyl groups at the 2,6-positions. The introduction of these ethyl groups has a similar effect as the addition of bromine/iodine atoms to that position, in that there is a ca. 28 nm red-shift of the main spectral bands. The ethyl groups result in a lower red-shift than the incorporation of bromine atoms, which in turn results in a smaller red-shift than iodine atoms. This can be attributed to differences in the strength of the mesomeric interactions in each case. As a result, BODIPY (**10**) is more red-shifted than BODIPY (**11**). BODIPYs (**18**) and (**10**) differ by the nature of the styryl groups at the 3,5-positions. BODIPY (**18**) has a strong EDG, while (**10**) has an EWG. The presence of strong EDGs in (**18**) results in the main spectral band of the dye being slightly more red-shifted than that of (**10**) (**Fig 6.03** and **Table 6.02**).

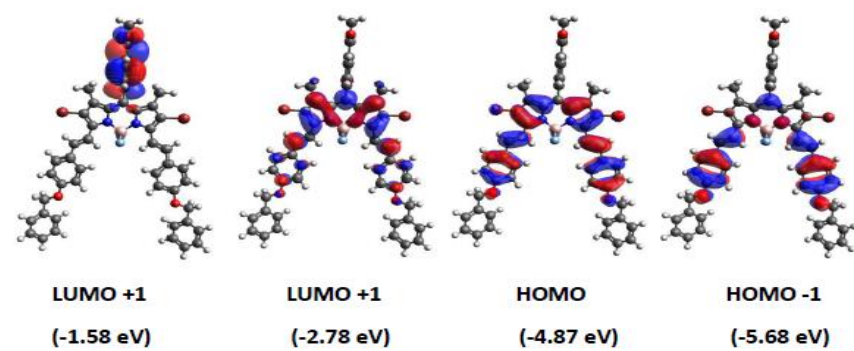
(1)



(3)



(12)



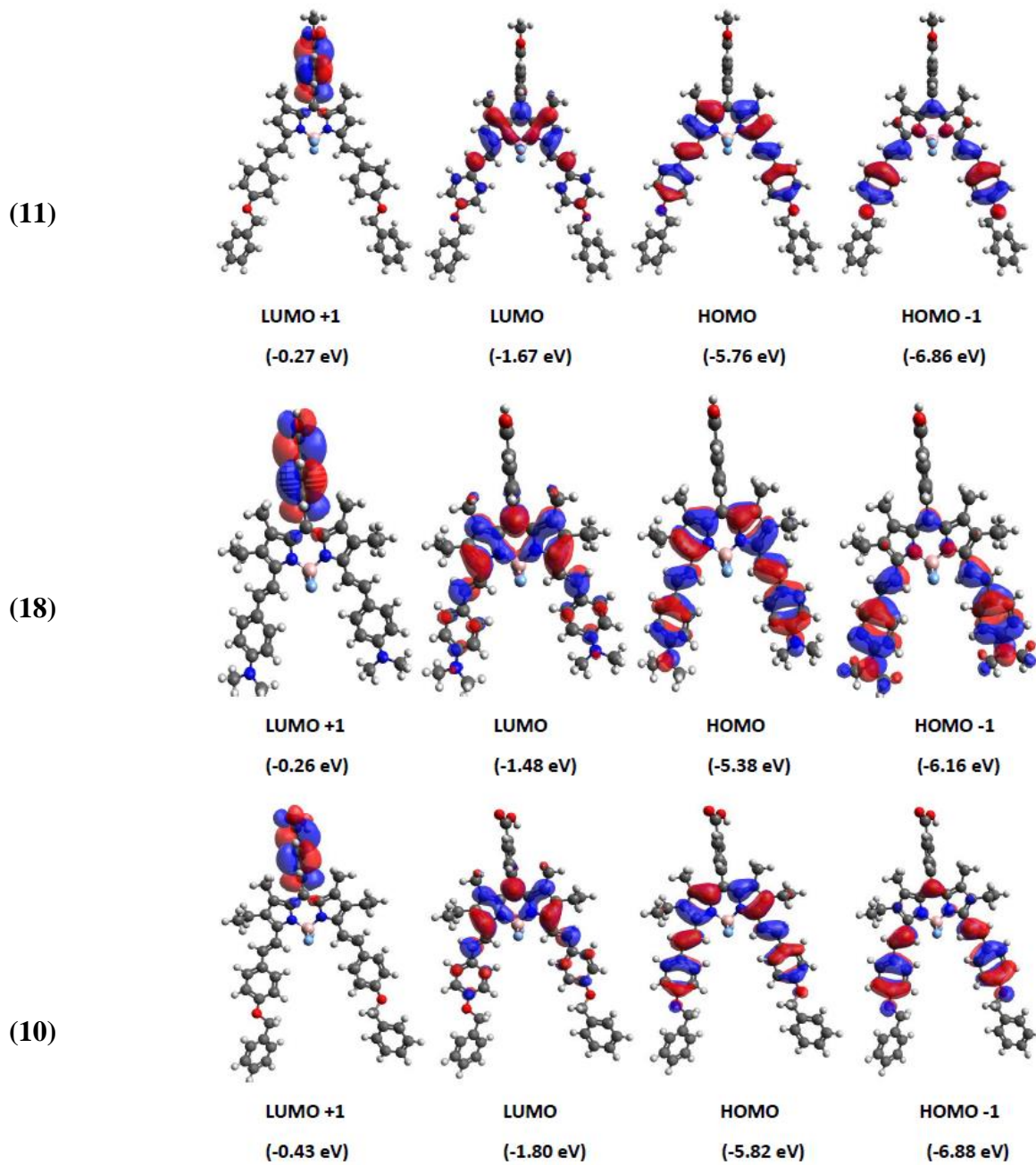


Figure 6.01 Nodal patterns at an isosurface value of 0.02 a.u. and frontier MO energies for BODIPYs (1), (3), (10), (11), (12), and (18) in TD-DFT calculations carried out using the CAM-B3LYP functional with SDD basis sets.

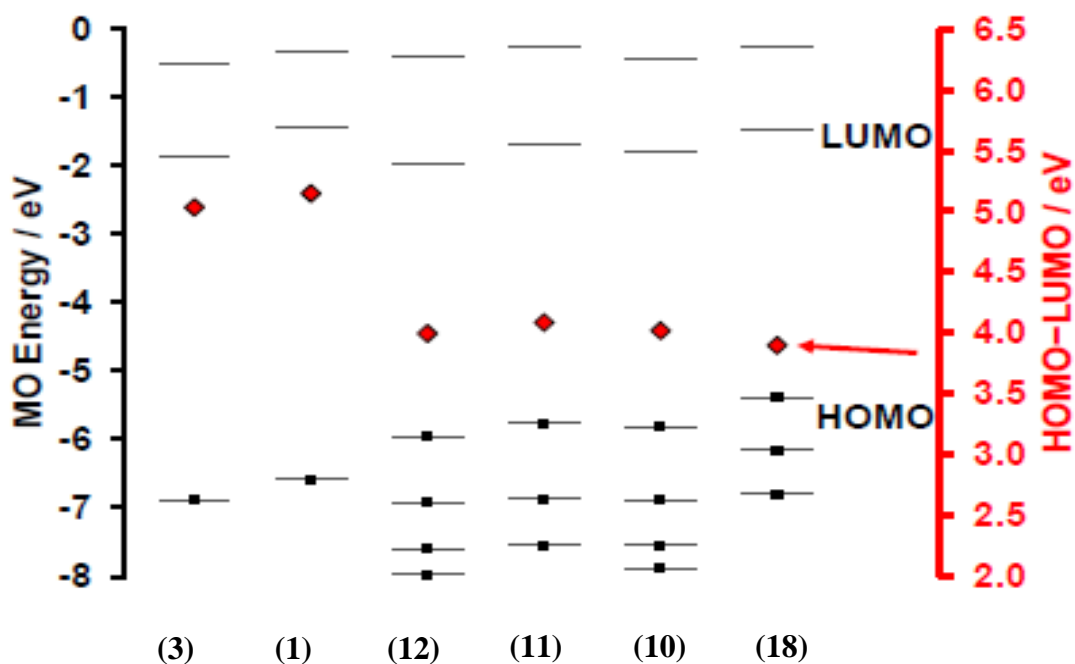


Figure 6.02 The frontier MO energies and HOMO–LUMO gaps for BODIPYs (1), (3), (10), (11), (12), and (18), using the CAM-B3LYP functional with the SDD basis set. The diamonds represent the HOMO–LUMO band gap energy and are plotted against a secondary axis. The dashes represent the MOs and the dots highlight the occupied MOs.

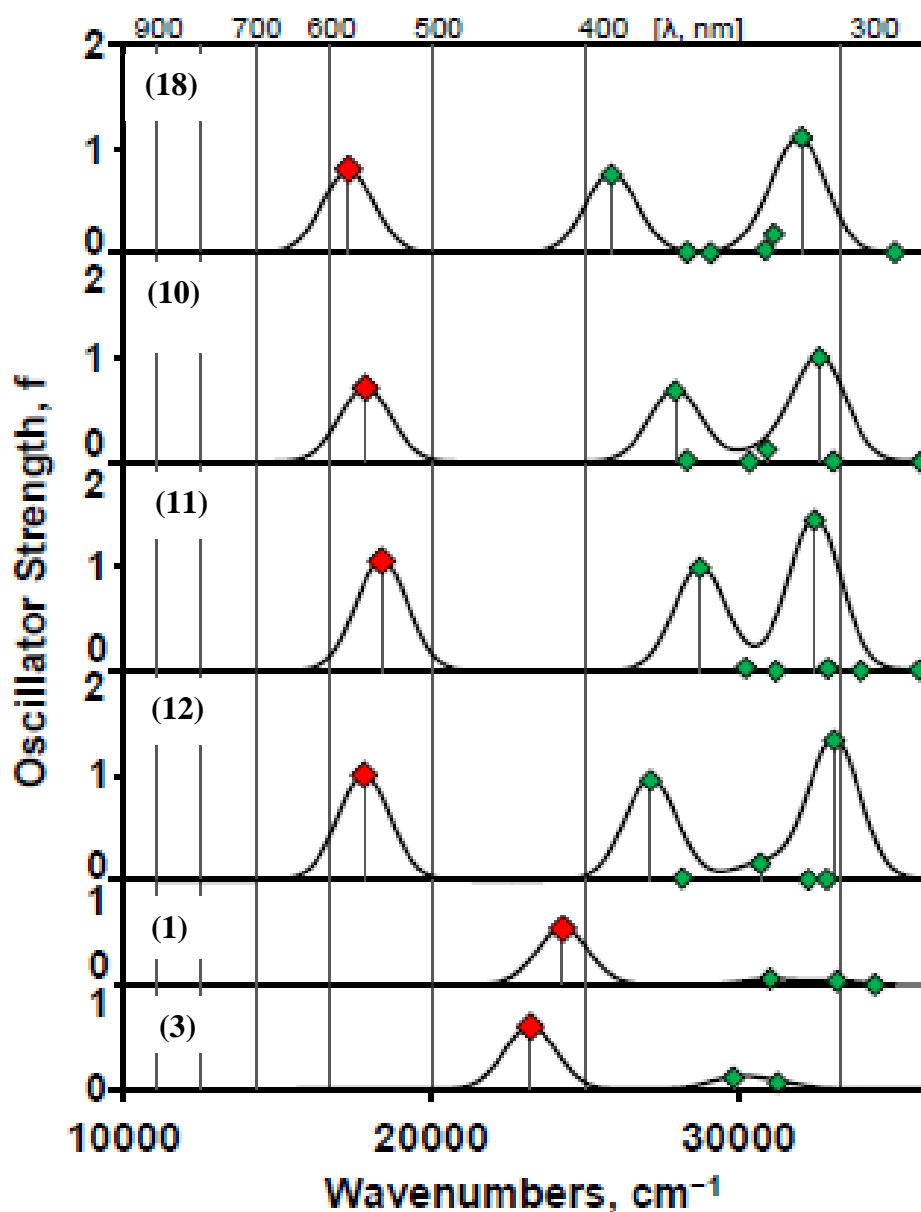


Figure 6.03 The TD-DFT calculations of BOIPYs (1), (3), (10), (11), (12), and (18) at the CAMB3LYP/6-31G (d) level of theory. Red diamonds are used to highlight the main visible region spectral bands. The details of the calculations are provided in **Table 6.02**.

Table 6.02 The TD-DFT calculations at the CAM-B3LYP/6-31G(d) basis sets for the B3LYP optimized structures of **(1)**, **(3)**, **(11)**, **(12)**, **(10)** and **(18)**.

# ^a	Calculated ^b			Experimental ^c		Wavefunction= ^d
	ν / cm^{-1}	λ / nm	f	ν / cm^{-1}	λ / nm	
						1
1	24.3	412	0.53	20.0	500	97% H → L; ...
						3
1	23.2	430	0.60	18.8	531	97% H → L; ...
						12
1	17.8	561	1.01	14.8	677	96% H → L; ...
2	27.1	369	0.96	---	---	93% H-1 ^{Sty} → L; ...
4	30.7	326	0.16	---	---	92% H-4 → L; ...
7	33.1	302	1.34	---	---	91% H-1 ^{Sty} → L+2 ^{Sty} ; 6% H-2 ^{Sty} → L+3 ^{Sty} ; ...
						11
1	18.4	544	1.06	15.3	653	96% H → L; ...
2	28.7	348	0.99	---	---	93% H-1 ^{Sty} → L; ...
5	32.5	308	1.45	---	---	89% H-1 ^{Sty} → L+2 ^{Sty} ; 5% H-2 ^{Sty} → L+3 ^{Sty} ; ...
						18
2	17.4	576	0.95	13.5	738	95% H → L; ...
2	25.9	386	0.94	---	---	94% H-1 ^{Sty} → L; ...
2	29.7	335	0.001	---	---	90% H-4 → L; ...
3	32.2	311	1.23	---	---	89% H-1 ^{Sty} → L+2 ^{Sty} ; 5% H-2 ^{Sty} → L+3 ^{Sty} ; ...
						10
1	17.9	559	0.94	14.9	667	94% H → L; ...
2	27.9	358	0.89	---	---	92% H-1 ^{Sty} → L; ...
5	32.6	306	1.31	---	---	90% H-1 ^{Sty} → L+2 ^{Sty} ; 5% H-2 ^{Sty} → L+3 ^{Sty} ; ...

^a The number of the state assigned in terms of ascending energy within the TD-DFT calculation. ^b Calculated band energies (10^3 cm^{-1}), wavelengths (nm) and oscillator strengths (c) in parentheses. ^c Observed energies (10^3 cm^{-1}) and wavelengths (nm) in DMSO. ^d The wave functions based on the eigenvectors predicted by TD-DFT. Only one-electron transitions of 5% or more are included. H and L are used to denote the HOMO and LUMO.

6.4 Concluding remarks

The TD-DFT calculations have proved to be a useful tool for establishing the structure-property relationships of a series of related BODIPY dyes, to enable a better understanding of their spectroscopic properties. The properties of the modelled dyes closely followed the trends observed for the synthesized dyes. Visualisation of the optimized geometries, and of the angular nodal patterns of these BODIPYs provided explanations for the spectral phenomena observed. Molecular modelling helps to provide an enhanced understanding of the trends that are observed experimentally, enabling the rational design of BODIPY dyes for use in applications such as PDT and NLO.

Chapter 7: Conclusions

7 Conclusion

A series of BODIPY cores, which generally have an intense absorption band at ca. 500 nm, were synthesized using the classic “one-pot-three-step” acid-catalyzed condensation reaction. Some of the BODIPY cores were synthesized as precursors for more complex structures to be studied for use in OL applications and in PDT. These core structures include BODIPYs (1), (7) and (9) (Schemes 2.01, 7 and 9). The spectroscopic properties of these dyes are very similar with the exception of BODIPY (9), which is red shifted by 28 nm when compared to the others in benzene. BODIPYs (4) and (6) were synthesized in the same manner as, (1), (7) and (16). However, although (4) and (6) were not used as precursors, their OL properties were explored to determine whether introducing a push-pull effect enhances the OL properties of BODIPY cores. BODIPY (4) has slightly differing spectroscopic properties as the fluorescence quantum yield is not as high as the other four BODIPYs, this is probably a result of the effect of intramolecular charge transfer on the S_1 state.

BODIPYs (1), (6), (7) and (9) were found to have negligible singlet oxygen quantum yields. In order to produce BODIPY dyes capable of generating singlet oxygen, BODIPYs (1) and (7) were brominated at the 2,6-positions, yielding BODIPYs (3) and (8) respectively. Furthermore, BODIPY (1) was iodinated and further hydrolyzed for conjugation to amine-functionalized UCNP to yield BODIPY (2) and (5) respectively. The attachment of bromine and iodine atoms to the BODIPY cores resulted in a red shift of ca. 30 and 39 nm respectively, with respect to the parent dyes. BODIPYs (2), (3) (8) and (5) displayed large singlet oxygen quantum yields that equalled that of the standard, Rose Bengal, and generally exhibited greater photostability than this compound, suggesting that they might prove useful as standards for Φ_{Δ} measurements. However, for the purposes of this work, the main interest was on BODIPY (5) as this dye was conjugated to the amine-functionalized UCNP to

explore the use of upconversion and FRET to generate singlet oxygen for biomedical applications.

UCNPs were synthesized, functionalized, and characterized. The nanoparticles were characterized by TEM, XRD, EDS, FT-IR spectroscopy, and AFM. Furthermore, the amine-functionalized UCNPs were successfully conjugated to a carboxylic acid functionalized BODIPY dye with a high singlet oxygen quantum yield value. The conjugation was confirmed through an analysis by TEM, EDS, FTIR spectroscopy and AFM. The conjugate displayed a lack of photostability when irradiated at 978 nm. After this was observed the conjugate was irradiated at 540 nm, and an increase in the singlet oxygen quantum yield of the BODIPY dye.

In order to red-shift the main spectral bands of the BODIPY dyes, BODIPYs **(1)**, **(3)**, **(7)**, **(8)** and **(9)** were modified by substitution at the 3,5-positions, *via* Knoevenagel condensation reactions. BODIPY **(1)** was reacted with 4-(dimethylamino)benzaldehyde to form **(9)**, which was further hydrolyzed to form **(16)**. Furthermore, BODIPY **(1)** was reacted with 4-(benzyloxy)benzaldehyde to form **(11)**. BODIPY **(3)** was reacted with 4-(benzyloxy)benzaldehyde to yield **(12)**. Additionally, BODIPY **(7)** and **(8)** were reacted with 4-(benzyloxy)benzaldehyde to yield **(13)** and **(14)** respectively. Lastly, BODIPY **(9)** was reacted with 4-(benzyloxy)benzaldehyde and 4-(dimethylamino)benzaldehyde to form **(10)** and **(17)** respectively, and **(17)** was further hydrolyzed to yield **(18)**.

BODIPY **(11)** formed by adding styryls to BODIPY **(1)** shows a much lower fluorescence quantum yield upon introduction of the styryl groups. A similar result is observed for BODIPYs **(10)**, **(13)**, **(16)**, and **(18)**. Additionally, there is a bigger decrease in the fluorescence quantum yield for **(1)**, and **(9)** upon adding dimethylaminostyryls at the 3,5-positions, and this can be attributed to the intramolecular charge transfer effects that are

brought about by the addition of strong EDGs to **(1)** and **(9)**. It is noteworthy that having EWGs around the BODIPY core does not reduce the fluorescence quantum yield as much as the effect of having a mix of EWGs and EDGs.

The NLO properties of BODIPY cores **(4)** and **(6)**, together with a number of 3,5-distyryl BODIPYs, **(10)**, **(11)** **(12)**, **(13)**, **(14)**, **(16)**, and **(18)**, were also investigated. All the 3,5-distyryl BODIPY dyes showed a good OL response at 532 nm in solution, with the best responses being observed for those with higher dipole moments. The superior OL properties of BODIPY **(4)** relative to those of BODIPY **(6)** provided good evidence of the importance of having push-pull structures through the introduction of EWG and EDG groups. BODIPYs **(11-14)** were embedded in PE as thin films and this greatly improved the OL properties. This allowed for a fair comparison of the heavy atom effect, and it was found that the introduction of heavy atoms at the 2,6-positions does not significantly enhance the OL properties.

Molecular modelling was used to investigate the spectral trends and structure-property relationships of the BODIPY dyes intended for use in PDT and NLO, and this helped to explain the red shifts of the main spectral band that are observed when the structure of the BODIPY fluorophore is modified. The values of the dipole moments obtained from the TD-DFT calculations was found to help in predicting which dyes will potentially have better OL properties. This assisted the rational design of the best dye as far as OL properties are concerned i.e. BODIPY **(16)** was designed to have a stronger dipole moment for optical OL applications.

7.1 Limitations and future work

- Further investigations are required on the methods used to conjugate the BODIPY to the UCNPs, since the BODIPY dye appeared to lack sufficient photostability upon irradiation at 978 nm. The evidence for FRET that was observed in the disappearance

of the 540 nm emission band of the UCNP conjugate upon excitation at 978 nm, demonstrates that further studies are merited.

- It was not possible to fully characterize 2PA with the nanosecond pulsed laser which was used in this study. In future, it would be helpful to use a femtosecond pulsed laser to fully characterize the 2PA nature of the dyes studied for OL.
- The open aperture technique was employed throughout in this work. Future studies using the closed aperture technique to investigate nonlinear refraction properties would potentially be of interest.
- The electronic structure of the BODIPY dye plays a crucial role in determining its properties. The structure, and therefore the OL response property of a molecule, is very sensitive to the level of theory and basis sets used. In this work, TD-DFT calculations were used to analyze trends in the lowest lying $S_0 \rightarrow S_1$ transition. In future, it would be helpful to employ both the DFT (B3LYP functional) and MP2 levels of theory to optimize the ground states of the BODIPY structures.
- The dipole moment values obtained from TD-DFT calculations seemed to correlate very well with the OL properties of the synthesized dyes. The higher the dipole moment values obtained from TD-DFT calculations, the better the OL properties of the dye. In future, this strong correlation will enable the rational design of significantly better optical limiters.
- Future studies will need to involve the use transient absorption spectroscopy for the S_1 and T_1 states [145, 146] to develop an enhanced understanding of what shapes the OL properties of BODIPY dyes.

8 References

1. A. Treibs and F. H. Kreuzer, *European Journal of Organic Chemistry*, **1968**, 718, 208-223.
2. F. J. Monsma, A. C. Barton, H. Chol Kang, D. L. Brassard, R. P. Haugland and D. R. Sibley, *Journal of Neurochemistry*, **1989**, 52, 1641-1644.
3. M. S. T. Gonçalves, *Chemical Reviews*, **2008**, 109, 190-212.
4. M. Shah, K. Thangaraj, M. L. Soong, L. T. Wolford, J. H. Boyer, I. R. Politzer and T. G. Pavlopoulos, *Heteroatom Chemistry*, **1990**, 1, 389-399.
5. G. Ulrich, R. Ziessel and A. Harriman, *Angewandte Chemie International Edition*, **2008**, 47, 1184-1201.
6. M. Baruah, W. Qin, R. A. Vallée, D. Beljonne, T. Rohand, W. Dehaen and N. Boens, *Organic Letters*, **2005**, 7, 4377-4380.
7. C. L. Amiot, S. Xu, S. Liang, L. Pan and J. X. Zhao, *Sensors*, **2008**, 8, 3082-3105.
8. J. O. Escobedo, O. Rusin, S. Lim and R. M. Strongin, *Current Opinion in Chemical Biology*, **2010**, 14, 64-70.
9. S. L. Niu, C. Massif, G. Ulrich, R. Ziessel, P.-Y. Renard and A. Romieu, *Organic & Biomolecular Chemistry*, **2011**, 9, 66-69.
10. V. Ntziachristos, C. Bremer and R. Weissleder, *European Radiology*, **2003**, 13, 195-208.
11. A. Loudet and K. Burgess, *Chemical Reviews*, **2007**, 107, 4891-4932.
12. R. Ziessel, G. Ulrich and A. Harriman, *New Journal of Chemistry*, **2007**, 31, 496-501.
13. A. B. Descalzo, H. J. Xu, Z. Shen and K. Rurack, *Annals of the New York Academy of Sciences*, **2008**, 1130, 164-171.
14. Y. W. Wang, A. B. Descalzo, Z. Shen, X. Z. You and K. Rurack, *Chemistry - A European Journal*, **2010**, 16, 2887-2903.
15. A. Harreus, *Pyrrrole. Ullmann's Encyclopedia of Industrial Chemistry*, Ludwigshafen, Wiley-VCH Verlag GmbH & Co. KGaA, 2000.
16. A. B. Descalzo, H.-J. Xu, Z.-L. Xue, K. Hoffmann, Z. Shen, M. G. Weller, X.-Z. You and K. Rurack, *Organic Letters*, **2008**, 10, 1581-1584.
17. Q. Zheng, G. Xu and P. N. Prasad, *Chemistry – A European Journal*, **2008**, 14, 5812-5819.

18. W. Qin, M. Baruah, W. M. De Borggraeve and N. Boens, *Journal of Photochemistry and Photobiology A: Chemistry*, **2006**, *183*, 190-197.
19. I. J. Arroyo, R. Hu, G. Merino, B. Z. Tang and E. Peña-Cabrera, *The Journal of Organic Chemistry*, **2009**, *74*, 5719-5722.
20. A. Schmitt, B. Hinkeldey, M. Wild and G. Jung, *Journal of Fluorescence*, **2009**, *19*, 755-758.
21. L. Li, B. Nguyen and K. Burgess, *Bioorganic & Medicinal Chemistry Letters*, **2008**, *18*, 3112-3116.
22. C. Thivierge, R. Bandichhor and K. Burgess, *Organic Letters*, **2007**, *9*, 2135-2138.
23. K. Tram, H. Yan, H. A. Jenkins, S. Vassiliev and D. Bruce, *Dyes and Pigments*, **2009**, *82*, 392-395.
24. A. C. Benniston and G. Copley, *Physical Chemistry Chemical Physics*, **2009**, *11*, 4124-4131.
25. L. Bonardi, G. Ulrich and R. Ziessel, *Organic Letters*, **2008**, *10*, 2183-2186.
26. E. V. De Wael, J. Pardoën, J. Van Koeveringe and J. Lugtenburg, *Recueil des Travaux Chimiques des Pays-Bas*, **1977**, *96*, 306-309.
27. R. Bandichhor, C. Thivierge, N. S. Bhuvanesh and K. Burgess, *Acta Crystallographica Section E: Structure Reports Online*, **2006**, *62*, o4310-o4311.
28. R. Hu, E. Lager, A. Aguilar-Aguilar, J. Liu, J. W. Lam, H. H. Sung, I. D. Williams, Y. Zhong, K. S. Wong and E. Pena-Cabrera, *The Journal of Physical Chemistry C*, **2009**, *113*, 15845-15853.
29. A. Kamkaew, S. H. Lim, H. B. Lee, L. V. Kiew, L. Y. Chung and K. Burgess, *Chemical Society Reviews*, **2013**, *42*, 77-88.
30. J. Michl, *Journal of the American Chemical Society*, **1978**, *100*, 6812-6818.
31. T. Yogo, Y. Urano, Y. Ishitsuka, F. Maniwa and T. Nagano, *Journal of the American Chemical Society*, **2005**, *127*, 12162-12163.
32. V. Lakshmi and M. Ravikanth, *Dalton Transactions*, **2012**, *41*, 5903-5911.
33. H. Lu, J. Mack, Y. Yang and Z. Shen, *Chemical Society Reviews*, **2014**, *43*, 4778-4823.
34. J. H. Gibbs, L. T. Robins, Z. Zhou, P. Bobadova-Parvanova, M. Cottam, G. T. McCandless, F. R. Fronczek and M. G. H. Vicente, *Bioorganic & Medicinal Chemistry*, **2013**, *21*, 5770-5781.
35. R. P. Sabatini, T. M. McCormick, T. Lazarides, K. C. Wilson, R. Eisenberg and D. W. McCamant, *The Journal of Physical Chemistry Letters*, **2011**, *2*, 223-227.

36. L. Jiao, W. Pang, J. Zhou, Y. Wei, X. Mu, G. Bai and E. Hao, *The Journal of Organic Chemistry*, **2011**, 76, 9988-9996.
37. S. Hoogendoorn, A. E. Blom, L. I. Willems, G. A. van der Marel and H. S. Overkleeft, *Organic Letters*, **2011**, 13, 5656-5659.
38. Y. Ni and J. Wu, *Organic & Biomolecular Chemistry*, **2014**, 12, 3774-3791.
39. K. Rurack, M. Kollmannsberger and J. Daub, *New Journal of Chemistry*, **2001**, 25, 289-292.
40. J. Chen, A. Burghart, A. Derecskei-Kovacs and K. Burgess, *The Journal of Organic Chemistry*, **2000**, 65, 2900-2906.
41. V. Leen, *Synthesis and Application of Reactive BODIPY dyes*, Katholieke Universiteit Leuven, Kasteelpark, Arenberg 11, B-3001 Heverlee (Leuven), Belgium 2010.
42. Z. Dost, S. Atilgan and E. U. Akkaya, *Tetrahedron*, **2006**, 62, 8484-8488.
43. P. Majumdar, X. Yuan, S. Li, B. Le Guennic, J. Ma, C. Zhang, D. Jacquemin and J. Zhao, *Journal of Materials Chemistry B*, **2014**, 2, 2838-2854.
44. H. Son, J. H. Lee, Y.-R. Kim, I. S. Lee, S. Han, X. Liu, J. Jaworski and J. H. Jung, *Analyst*, **2012**, 137, 3914-3916.
45. H. Son, H. Y. Lee, J. M. Lim, D. Kang, W. S. Han, S. S. Lee and J. H. Jung, *Chemistry – A European Journal*, **2010**, 16, 11549-11553.
46. N. Nombona, K. Maduray, E. Antunes, A. Karsten and T. Nyokong, *Journal of Photochemistry and Photobiology B: Biology*, **2012**, 107, 35-44.
47. G. M. F. Calixto, J. Bernegossi, L. M. de Freitas, C. R. Fontana and M. Chorilli, *Molecules*, **2016**, 21, 342.
48. J. Moan and Q. Peng, *Anticancer Research*, **2003**, 23, 3591-3600.
49. Y. Yang, Q. Guo, H. Chen, Z. Zhou, Z. Guo and Z. Shen, *Chemical Communications*, **2013**, 49, 3940-3942.
50. D. E. Dolmans, D. Fukumura and R. K. Jain, *Nature Reviews Cancer*, **2003**, 3, 380-387.
51. A. B. Ormond and H. S. Freeman, *Materials*, **2013**, 6, 817-840.
52. C. Hopper, *The Lancet Oncology*, **2000**, 1, 212-219.
53. F. Auzel, *Journal of Luminescence*, **1990**, 45, 341-345.
54. J.-C. G. Bünzli and S. V. Eliseeva, in *Lanthanide Luminescence*, Springer, Salmon Tower Building New York City, 2010, pp. 1-45.
55. P. Dorenbos, *Journal of Luminescence*, **2000**, 91, 91-106.

56. A. Aebischer, F. Gummy and J.-C. G. Bünzli, *Physical Chemistry Chemical Physics*, **2009**, *11*, 1346-1353.
57. F. Wang and X. Liu, *Chemical Society Reviews*, **2009**, *38*, 976-989.
58. J. Suyver, J. Grimm, K. Krämer and H.-U. Güdel, *Journal of Luminescence*, **2005**, *114*, 53-59.
59. D. Vennerberg and Z. Lin, *Science of Advanced Materials*, **2011**, *3*, 26-40.
60. J. Suyver, A. Aebischer, D. Biner, P. Gerner, J. Grimm, S. Heer, K. Krämer, C. Reinhard and H.-U. Güdel, *Optical Materials*, **2005**, *27*, 1111-1130.
61. J. Chen and J. X. Zhao, *Sensors*, **2012**, *12*, 2414-2435.
62. F. Auzel, *Chemical Reviews*, **2004**, *104*, 139-174.
63. Y. I. Park, S. H. Nam, J. H. Kim, Y. M. Bae, B. Yoo, H. M. Kim, K.-S. Jeon, H. S. Park, J. S. Choi and K. T. Lee, *The Journal of Physical Chemistry C*, **2013**, *117*, 2239-2244.
64. G.-M. Han, H. Li, X.-X. Huang and D.-M. Kong, *Talanta*, **2016**, *147*, 207-212.
65. G.-M. Han, H.-X. Jiang, Y.-F. Huo and D.-M. Kong, *Journal of Materials Chemistry B*, **2016**, *4*, 3351-3357.
66. J.-N. Liu, W.-B. Bu and J.-L. Shi, *Accounts of Chemical Research*, **2015**, *48*, 1797-1805.
67. M. Wang, G. Abbineni, A. Clevenger, C. Mao and S. Xu, *Nanomedicine: Nanotechnology, Biology and Medicine*, **2011**, *7*, 710-729.
68. P. Xie and S. C. Rand, *Optics Letters*, **1992**, *17*, 1198-1200.
69. H. Lian, Z. Hou, M. Shang, D. Geng, Y. Zhang and J. Lin, *Energy*, **2013**, *57*, 270-283.
70. Y. Liu, K. Ai and L. Lu, *Nanoscale*, **2011**, *3*, 4804-4810.
71. J. M. Meruga, W. M. Cross, P. S. May, Q. Luu, G. A. Crawford and J. J. Kellar, *Nanotechnology*, **2012**, *23*, 395-201.
72. C.-J. Carling, J.-C. Boyer and N. R. Branda, *Journal of the American Chemical Society*, **2009**, *131*, 10838-10839.
73. J.-C. Boyer, C.-J. Carling, B. D. Gates and N. R. Branda, *Journal of the American Chemical Society*, **2010**, *132*, 15766-15772.
74. M. Haase and H. Schäfer, *Angewandte Chemie International Edition*, **2011**, *50*, 5808-5829.
75. P. L. Corstjens, L. van Lieshout, M. Zuiderwijk, D. Kornelis, H. J. Tanke, A. M. Deelder and G. J. van Dam, *Journal of Clinical Microbiology*, **2008**, *46*, 171-176.

76. B. Liu, H. Tan and Y. Chen, *Analytica Chimica Acta*, **2013**, 761, 178-185.
77. J. Harris, L. Gai, G. Kubheka, J. Mack, T. Nyokong and Z. Shen, *Chemistry – A European Journal*, **2017**, 23, 14507-14514.
78. G. Kubheka, O. Achadu, J. Mack and T. Nyokong, *New Journal of Chemistry*, **2017**, 41, 12319-12325.
79. G. Kubheka, J. Mack, N. Kobayashi, M. Kimura and T. Nyokong, *Journal of Porphyrins and Phthalocyanines*, **2017**, 21, 523-531.
80. B. Kulyk, S. Taboukhat, H. Akdas-Kilig, J.-L. Fillaut, Y. Boughaleb and B. Sahraoui, *RSC Advances*, **2016**, 6, 84854-84859.
81. Y. Chen, L. Gao, M. Feng, L. Gu, N. He, J. Wang, Y. Araki, W. J. Blau and O. Ito, *Mini Reviews in Organic Chemistry*, **2009**, 6, 55-65.
82. G. De La Torre, P. Vázquez, F. Agullo-Lopez and T. Torres, *Chemical Reviews*, **2004**, 104, 3723-3750.
83. M. Spaeth and W. Sooy, *The Journal of Chemical Physics*, **1968**, 48, 2315-2323.
84. M. Sheik-Bahae, A. A. Said, T.-H. Wei, D. J. Hagan and E. W. Van Stryland, *IEEE Journal of Quantum Electronics*, **1990**, 26, 760-769.
85. M. Sheik-Bahae, A. A. Said and E. W. Van Stryland, *Optics Letters*, **1989**, 14, 955-957.
86. M. G. Kuzyk and C. W. Dirk, *Characterization Techniques and Tabulations for Organic NLO Materials*, Marcel Dekker, Beltsville, Maryland and Washington, D.C, 1998.
87. R. L. Sutherland, *Handbook of Nonlinear Optics*, CRC press, New York, New York, 2003.
88. H. S. Nalwa and S. Miyata, *Nonlinear Optics of Organic Molecules and Polymers*, CRC press, Boca Raton, Florida, 1996.
89. F. C. Delori, R. H. Webb and D. H. Sliney, *Journal of the Optical Society of America*, **2007**, 24, 1250-1265.
90. R. C. Hollins, *Current Opinion in Solid State and Materials Science*, **1999**, 4, 189-196.
91. B. P. Ngoy, Z. Hlatshwayo, N. Nwaji, G. Fomo, J. Mack and T. Nyokong, accepted for publication in *Journal of Porphyrins and Phthalocyanines* in **2018**. [doi: 10.1142/S1088424617500857]
92. M. Frisch, G. Trucks, H. Schlegel, G. Scuseria, M. Robb, J. Cheeseman, G. Scalmani, V. Barone, B. Mennucci and G. Petersson, *09, Revision d. 01, Gaussian*, Wallingford Connecticut, New York, 2009.

93. M. D. Hanwell, D. E. Curtis, D. C. Lonie, T. Vandermeersch, E. Zurek and G. R. Hutchison, *Journal of Cheminformatics*, **2012**, *4*, 17.
94. A. M. Brouwer, *Pure and Applied Chemistry*, **2011**, *83*, 2213-2228.
95. A. Ogunsipe, J.-Y. Chen and T. Nyokong, *New Journal of Chemistry*, **2004**, *28*, 822-827.
96. D. Magde, R. Wong and P. G. Seybold, *Photochemistry and Photobiology*, **2002**, *75*, 327-334.
97. R. F. Kubin and A. N. Fletcher, *Journal of Luminescence*, **1982**, *27*, 455-462.
98. M. Kubinyi, T. Vidóczy, O. Varga, K. Nagy and I. Bitter, *Applied Spectroscopy*, **2005**, *59*, 134-139.
99. I. Roy, T. Y. Ohulchansky, D. J. Bharali, H. E. Pudavar, R. A. Mistretta, N. Kaur and P. N. Prasad, *Proceedings of the National Academy of Sciences of the United States of America*, **2005**, *102*, 279-284.
100. D. O'Connor, *Time-Correlated Single Photon Counting*, Academic Press, Academic, London 2012.
101. M. P. Wahl, *Time-Correlated Single Photon Counting*, http://www.picoquant.com/images/uploads/page/files/7253/technote_tcspc.pdf, PicoQuant Technical Note, Germany. Accessed 2017/10/09, 2017.
102. R. Chen, R. Wu, G. Zhang, Y. Gao, L. Xiao and S. Jia, *Sensors*, **2014**, *14*, 2449-2467.
103. W. Becker, A. Bergmann, M. Hink, K. König, K. Benndorf and C. Biskup, *Microscopy Research and Technique*, **2004**, *63*, 58-66.
104. X.-F. Zhang, Y. Lin, W. Guo and J. Zhu, *Spectrochimica Acta Part A: Molecular and Biomolecular Spectroscopy*, **2014**, *133*, 752-758.
105. D. Pietrangeli, A. Rosa, S. Ristori, A. Salvati, S. Altieri and G. Ricciardi, *Coordination Chemistry Reviews*, **2013**, *257*, 2213-2231.
106. F. Wilkinson, W. P. Helman and A. B. Ross, *Journal of Physical and Chemical Reference Data*, **1993**, *22*, 113-262.
107. Y. Usui, *Chemistry Letters*, **1973**, *2*, 743-744.
108. R. O. Ogbodu, PhD Thesis, Rhodes University, South Africa, 2015.
109. R. O. Ogbodu, E. Antunes and T. Nyokong, *Polyhedron*, **2013**, *60*, 59-67.
110. P. Carloni, E. Damiani, L. Greci, P. Stipa, F. Tanfani, E. Tartaglioni and M. Wozniak, *Research on Chemical Intermediates*, **1993**, *19*, 395-405.

111. J. T. Lau, P.-C. Lo, W.-P. Fong and D. K. Ng, *Journal of Medicinal Chemistry*, **2012**, *55*, 5446-5454.
112. S. E. Maree and T. Nyokong, *Journal of Porphyrins and Phthalocyanines*, **2001**, *5*, 782-792.
113. N. Kuznetsova, N. Gretsova, E. Kalmykova, E. Makarova, S. Dashkevich, V. Negrimovskii, O. Kaliya and E. Luk'yanets, *Russian Journal of General Chemistry*, **2000**, *70*, 133-140.
114. R. W. Redmond and J. N. Gamlin, *Photochemistry and Photobiology*, **1999**, *70*, 391-475.
115. X.-J. Jiang, P.-C. Lo, S.-L. Yeung, W.-P. Fong and D. K. Ng, *Chemical Communications*, **2010**, *46*, 3188-3190.
116. A. Ogunsipe, D. Maree and T. Nyokong, *Journal of Molecular Structure*, **2003**, *650*, 131-140.
117. W. Spiller, H. Kliesch, D. Wöhrle, S. Hackbarth, B. Röder and G. Schnurpfeil, *Journal of Porphyrins and Phthalocyanines*, **1998**, *2*, 145-158.
118. N. Gandra, A. T. Frank, O. Le Gendre, N. Sawwan, D. Aebisher, J. F. Liebman, K. Houk, A. Greer and R. Gao, *Tetrahedron*, **2006**, *62*, 10771-10776.
119. M. C. DeRosa and R. J. Crutchley, *Coordination Chemistry Reviews*, **2002**, *233*, 351-371.
120. D. Neckers, *Journal of Photochemistry and Photobiology A: Chemistry*, **1989**, *47*, 1-29.
121. E. A. Ermilov, J.-Y. Liu, R. Menting, Y.-S. Huang, B. Röder and D. K. Ng, *Physical Chemistry Chemical Physics*, **2016**, *18*, 10964-10975.
122. I. S. Turan, F. P. Cakmak, D. C. Yildirim, R. Cetin-Atalay and E. U. Akkaya, *Chemistry – A European Journal*, **2014**, *20*, 16088-16092.
123. P. Sen, G. Y. Atmaca, A. Erdoğan, N. Dege, H. Genç, Y. Atalay and S. Z. Yildiz, *Journal of Fluorescence*, **2015**, *25*, 1225-1234.
124. H. Chen, F. Yuan, S. Wang, J. Xu, Y. Zhang and L. Wang, *Biosensors and Bioelectronics*, **2013**, *48*, 19-25.
125. K. Sanusi, J. M. Stone and T. Nyokong, *New Journal of Chemistry*, **2015**, *39*, 1665-1677.
126. S. D. Topel, G. T. Cin and E. U. Akkaya, *Chemical Communications*, **2014**, *50*, 8896-8899.
127. M. Frenette, M. Hatamimoslehabadi, S. Bellinger-Buckley, S. Laoui, J. La, S. Bag, S. Mallidi, T. Hasan, B. Bouma and C. Yelleswarapu, *Journal of the American Chemical Society*, **2014**, *136*, 15853-15856.

128. R. Misra, *The Journal of Physical Chemistry C*, **2017**, *121*, 5731-5739.
129. B. Kim, B. Sui, X. Yue, S. Tang, M. G. Tichy and K. D. Belfield, *European Journal of Organic Chemistry*, **2017**, *2017*, 25-28.
130. W. Hu, X.-F. Zhang, X. Lu, S. Lan, D. Tian, T. Li, L. Wang, S. Zhao, M. Feng and J. Zhang, *Dyes and Pigments*, **2017**.
131. A. Filarowski, M. Kluba, K. Cieřlik-Boczula, A. Koll, A. Kochel, L. Pandey, W. M. De Borggraeve, M. Van der Auweraer, J. Catalán and N. Boens, *Photochemical & Photobiological Sciences*, **2010**, *9*, 996-1008.
132. G. de la Torre, T. Torres and F. Agulló-López, *Advanced Materials*, **1997**, *9*, 265-269.
133. D. Dini, M. Barthel and M. Hanack, *European Journal of Organic Chemistry*, **2001**, *2001*, 3759-3769.
134. K. Sharafudeen, G. Reddy and K. Chandrasekharan, *Journal of Modern Optics*, **2009**, *56*, 1853-1859.
135. C. Mkhize, J. Britton and T. Nyokong, *Polyhedron*, **2014**, *81*, 607-613.
136. M. Calvete, G. Y. Yang and M. Hanack, *Synthetic Metals*, **2004**, *141*, 231-243.
137. K. Sanusi, E. Antunes and T. Nyokong, *Dalton Transactions*, **2014**, *43*, 999-1010.
138. E. Hemmer, A. Benayas, F. Légaré and F. Vetrone, *Nanoscale Horizons*, **2016**, *1*, 168-184.
139. V. K. Sreenivasan, A. V. Zvyagin and E. M. Goldys, *Journal of Physics: Condensed Matter*, **2013**, *25*, 194101.
140. R. Frankel, *Aggregation and Toxicity of Amine-Functionalized Polystyrene Nanoparticles*, Lund University, Lund, Sweden, 2017.
141. Y. Yang, A. Dominguez, D. Zhang, V. Lutsker, T. A. Niehaus, T. Frauenheim and W. Yang, *The Journal of Chemical Physics*, **2017**, *146*, 124104.
142. T. Komatsu, Y. Urano, Y. Fujikawa, T. Kobayashi, H. Kojima, T. Terai, K. Hanaoka and T. Nagano, *Chemical Communications*, **2009**, 7015-7017.
143. T. Yanai, D. P. Tew and N. C. Handy, *Chemical Physics Letters*, **2004**, *393*, 51-57.
144. M. Zakerhamidi, M. Moghadam, A. Ghanadzadeh and S. Hosseini, *Journal of Luminescence*, **2012**, *132*, 931-937.
145. G. H. Summers, J.-F. Lefebvre, F. A. Black, E. S. Davies, E. A. Gibson, T. Pullerits, C. J. Wood and K. Zidek, *Physical Chemistry Chemical Physics*, **2015**, *18*, 1059-1070.

146. P. Yang, J. Zhao, W. Wu, X. Yu and Y. Liu, *The Journal of Organic Chemistry*, **2012**, *77*, 6166-6178.